

POLITECNICO
MILANO 1863

SCUOLA DI INGEGNERIA INDUSTRIALE
E DELL'INFORMAZIONE

Development and implementation of a sensor system for physiological measurements in simulated flight for Rotorcraft-Pilot Coupligs assessment

Tesi di Laurea Magistrale in
Aeronautical Engineering - Ingegneria Aeronautica

Author: **Thomas Soldan**

Student ID: 226361
Advisor: Prof. Andrea Zanoni
Co-advisors: Prof. Pierangelo Masarati
Academic Year: 2024-25

Abstract

Rotorcraft-Pilot Couplings (RPCs) represent a critical safety challenge in modern aviation, manifesting as adverse feedback loops between the pilot's control strategy and the vehicle's high-order dynamics. While traditional analysis often focuses on the mechanical response of the airframe, the pilot's physiological and cognitive states— specifically Muscular Activation Level and Mental Workload (MWL) — play a decisive role in the onset of phenomena such as Pilot-Assisted Oscillations (PAO). Current assessment methods, predominantly reliant on subjective ratings like the Bedford Scale, lack the temporal resolution and objectivity required to fully characterize these complex interactions.

This thesis presents the development, implementation, and validation of a multi-modal sensor ecosystem designed to ultimately enable the objective quantification of pilot workload and biomechanical response within a high-fidelity simulation environment. The experimental setup was integrated into the RPC Test Rig at the FRAME-Lab (Politecnico di Milano), utilizing the MARSH (Modular Architecture for Reconfigurable Simulation of Helicopters) architecture as the backbone for data synchronization and management. The hardware suite comprises five distinct modules: Surface Electromyography (sEMG) to monitor muscle activation and fatigue; Eye Tracking to assess cognitive load via pupillometry and gaze behavior; Electrocardiogram (ECG) for heart rate variability analysis; a computer vision-based Body Pose tracking system for non-intrusive kinematic reconstruction to facilitate the video-based identification of pathological events; and a novel optical force sensor (OPT-IN) to measure grip pressure dynamics based on Frustrated Total Internal Reflection (FTIR).

An experimental campaign involving both professional pilots and non-pilot subjects was conducted using simplified 2-DOF flight models executing ADS-33E Mission Task Elements, specifically vertical repositioning maneuvers. Preliminary results demonstrate the system's capability to provide robust, synchronized telemetry of physiological parameters. Data analysis revealed significant correlations between flight phases and physiological markers, identifying distinct trends in muscle fatigue, grip force modulation, and cardiac response variations between expert and novice operators. This research establishes a validated methodological framework for the objective assessment of pilot physiological states and forces at the human-machine interface, potentially paving the way for the development of adaptive interfaces capable of mitigating RPC risks.

Keywords: Rotorcraft-Pilot Couplings, Mental Workload, Physiological Sensors, Flight

Simulation, Biodynamic Feedthrough.

Abstract in lingua italiana

I fenomeni di accoppiamento pilota-elicottero (Rotorcraft-Pilot Couplings, RPC) rappresentano una sfida critica per la sicurezza nell'aviazione moderna, manifestandosi come anelli di retroazione avversi tra la strategia di controllo del pilota e le dinamiche di ordine superiore del veicolo. Mentre l'analisi tradizionale si concentra spesso sulla risposta meccanica della cellula, gli stati fisiologici e cognitivi del pilota — nello specifico il livello di attivazione muscolare e il carico di lavoro mentale (Mental Workload, MWL) — giocano un ruolo decisivo nell'insorgenza di fenomeni quali le oscillazioni pilota-assistite (Pilot-Assisted Oscillations, PAO). Gli attuali metodi di valutazione, basati prevalentemente su metriche soggettive come la scala Bedford, mancano della risoluzione temporale e dell'oggettività necessarie per caratterizzare appieno queste interazioni complesse.

Questa tesi presenta lo sviluppo, l'implementazione e la validazione di un ecosistema di sensori multi-modale progettato per consentire la quantificazione oggettiva del carico di lavoro e della risposta biomeccanica del pilota all'interno di un ambiente di simulazione ad alta fedeltà. Il setup sperimentale è stato integrato nel RPC Test Rig presso il FRAME-Lab (Politecnico di Milano), utilizzando l'architettura MARSH (Modular Architecture for Reconfigurable Simulation of Helicopters) come infrastruttura per la sincronizzazione e la gestione dei dati. La suite hardware comprende cinque moduli distinti: Elettromiografia di superficie (sEMG) per monitorare l'attivazione e l'affaticamento muscolare; Eye Tracking per valutare il carico cognitivo tramite pupillometria e comportamento dello sguardo; Elettrocardiogramma (ECG) per l'analisi della variabilità della frequenza cardiaca; un sistema di tracciamento della postura (Body Pose) basato su visione artificiale per la ricostruzione cinematica non intrusiva, finalizzato a facilitare l'identificazione video-assistita di eventi patologici; e un innovativo sensore di forza (OPT-IN) per misurare la dinamica della pressione di presa sui comandi di volo basato sulla riflessione totale interna frustrata (FTIR).

È stata condotta una campagna sperimentale coinvolgendo sia piloti professionisti che soggetti non piloti, utilizzando modelli di volo semplificati a 2-DOF nell'esecuzione di Mission Task Elements secondo lo standard ADS-33E, specificamente manovre di riposizionamento verticale. I risultati preliminari dimostrano la capacità del sistema di fornire una telemetria robusta e sincronizzata dei parametri fisiologici. L'analisi dei dati ha rivelato correlazioni significative tra le fasi di volo e i marcatori fisiologici, identificando trend distinti nell'affaticamento muscolare, nella modulazione della forza di presa e nelle variazioni

della risposta cardiaca tra operatori esperti e novizi. Questa ricerca stabilisce un quadro metodologico validato per la valutazione oggettiva degli stati fisiologici del pilota e delle forze all'interfaccia uomo-macchina, ponendo le basi per lo sviluppo di interfacce adattive capaci di mitigare i rischi legati ai fenomeni RPC.

Parole chiave: Rotorcraft-Pilot Couplings, Carico di Lavoro Mentale, Sensori Fisiologici, Simulazione di Volo, Biodynamic Feedthrough.

Contents

Abstract **i**

Abstract in lingua italiana **iii**

Contents **v**

1 Introduction to Rotorcraft - Pilot Coupling **1**

1.1 Background and Motivation 1

1.2 Nature and Characteristics of RPC 2

1.2.1 Categorization of RPC 2

1.2.2 Causative and Contributing Factors 3

1.3 Examples of Rotorcraft-Pilot Coupling (RPC) Events 4

1.3.1 Slung Load Operations and Airframe Dynamics (Low Frequency RPC) 4

1.3.2 FBW and Time Delay Issues (Nonlinear RPC) 5

1.3.3 Collective Bounce (High Frequency Aeroelastic RPC) 6

1.3.4 Shipboard Operations (Operational Environment RPC) 7

1.3.5 Conclusion: The Link Between Workload, BDFT, and RPC 9

2 Mental Workload and Performance Quantification in Advanced Flight Systems **11**

2.1 Conceptualisation and Theoretical Framework of Mental Workload 11

2.1.1 Evolution of the Workload Concept 11

2.2 The Evolving Pilot Role in Automated Cockpits 12

2.2.1 The Automation Paradox and Safety Implications 12

2.2.2 Future Operational Concepts 12

2.3 Multimodal Methodologies for MWL Assessment 13

2.3.1 Psychophysiological Metrics: Mechanisms and Correlates 13

2.3.2 MWL in Complex Multitask Activity: The Role of Expertise 14

2.3.3 MWL in Extreme and Complex Helicopter Operations 15

2.4 Quantitative Performance and Control Activity Metrics 17

2.4.1 Objective Performance Metrics and Subjective Correlates 17

2.4.2 The Attack Chart Methodology: Objective Quantification of Pilot Control Effort . . . 17
2.5 Conclusions . . . 20

3 Workload measurement techniques and study methods 21
3.1 Surface Electromyography (sEMG) . . . 21
3.1.1 Principles of Signal Generation and Detection . . . 21
3.1.2 Workload Quantification via sEMG Features . . . 22
3.1.3 Critical Factors: Innervation Zone and Electrode Placement . . . 23
3.1.4 sEMG in RPC Phenomena . . . 24
3.2 Eye-Tracking in Helicopter Flight for Pilot Workload Assessment . . . 25
3.2.1 Introduction to Eye-Tracking as a Workload Metric . . . 25
3.2.2 Eye-Tracking Measures for Workload Assessment . . . 26
3.2.3 Eye-Tracking in Flight Environments . . . 28
3.2.4 Eye-Tracking and Attentional Tunneling . . . 28
3.3 Heart Rate and Heart Rate Variability for Workload Evaluation . . . 29
3.3.1 Heart Rate (HR) as an Indicator of Pilot Stress . . . 29
3.3.2 Heart Rate Variability (HRV) Metrics . . . 30
3.3.3 Classification of Workload using Machine Learning . . . 31
3.4 Body Pose Estimation and Tracking . . . 32
3.4.1 Foundation of Markerless Pose Estimation . . . 32
3.4.2 Application to Collective Inceptor Tracking in RPC for multibody models validation . . . 34
3.5 The Correlation Between Pilot Workload and Control Inceptor Pressure . . . 36
3.5.1 Grip Pressure Evaluation: From Workload to Optical Sensing . . . 36
3.6 Evaluation of Pilot Workload: The Bedford Workload Scale . . . 37
3.6.1 Conceptual Basis and Structure . . . 37
3.6.2 Operational Use and Methodological Considerations . . . 39

4 Experimental setup: physiological sensors 41
4.1 sEMG measures . . . 41
4.1.1 Description of the sEMG Acquisition System (Raw-Power) . . . 41
4.1.2 EMG Signal Analysis for Workload Assessment . . . 44
4.2 Eye tracking measures . . . 48
4.2.1 Pupil Core Eye Tracking System . . . 48
4.2.2 MARSH Eye Tracking Integration . . . 50
4.2.3 Eye Tracking Data Analysis . . . 53
4.3 ECG Measurement System Architecture . . . 56
4.3.1 Analog Front-End: AD8232 Sensor . . . 57
4.3.2 Data Acquisition, Processing Unit and Communication . . . 59

4.3.3 Data Analysis 60
4.4 Body Pose Tracking 63
4.4.1 Hardware: Intel RealSense Depth Camera D455f 63
4.4.2 Software Implementation and Pose Detection 64
4.5 OPT-IN Instrumentation: Frustrated Total Internal Reflection (FTIR) . . . 67
4.5.1 Mechanical Design and Operating Principle 68

5 Experimental setup: Test Aircraft and Flight Simulation 71
5.1 Test Aircraft Configuration 71
5.2 Vertical Maneuver - RPC Evaluation 72
5.2.1 Objectives 73
5.2.2 Maneuver Description 73
5.2.3 Test Course Specification 74
5.2.4 Performance Standards 75
5.3 Vertical Repositioning Simulations 76
5.3.1 Simulated Environment 76
5.3.2 Pilot Preparation 78

6 Final Assembly and Results 79
6.1 Final Hardware Assembly 79
6.1.1 sEMG Module 80
6.1.2 Eye Tracking Module 81
6.1.3 ECG Module 81
6.1.4 Body Pose Module 83
6.1.5 OPT-IN Module 84
6.2 Final Software Implementation 86
6.2.1 Synchronization and Data Logging 86
6.2.2 Post-Processing and Analysis 86
6.3 Preliminary Sensors Results 86
6.3.1 sEMG Results 87
6.3.2 Eye Tracking Results 92
6.3.3 ECG Results 93
6.3.4 Body Pose Results 97
6.3.5 OPT-IN Results 98

7 Conclusions and future developments 101
7.1 Conclusions on System Integration 101
7.1.1 Hardware Integration and Signal Integrity 101
7.1.2 Software Infrastructure and Data Synchronization 101
7.1.3 Post-Processing Pipeline 102

7.2 Future Developments . . . 102
7.2.1 Software Enhancements . . . 102
7.2.2 Development of an Objective Workload Assessment System . . . 104
7.2.3 Proposed Experimental Protocol for Workload Validation . . . 104

Bibliography **107**

A Appendix A - RPC Test Rig **115**
A.1 Overview and Purpose . . . 115
A.2 Motion Platform System (MPS) . . . 116
A.2.1 Dynamic Capabilities . . . 116
A.2.2 Usage Modes . . . 117
A.3 Structural Components . . . 117
A.3.1 Support Structure . . . 118
A.3.2 Pilot Seat . . . 118
A.4 Cockpit Inceptors and Control Loading . . . 118
A.4.1 Inceptors Assembly . . . 119
A.4.2 Control Loading System (CLS) Upgrade . . . 120
A.5 Instrumentation and Data Acquisition . . . 120
A.5.1 Sensors . . . 120
A.6 Closed-Loop Simulation Architecture . . . 120

B Appendix B - The MARSH Simulation Environment **123**
B.1 Project Rationale and Research Objectives . . . 123
B.1.1 Design Philosophy . . . 123
B.2 System Architecture . . . 124
B.2.1 The Core: MARSH Manager . . . 124
B.2.2 Peripheral Nodes . . . 125
B.3 Software Development Ecosystem . . . 126
B.3.1 Rapid Prototyping: `marsh-py` . . . 126
B.3.2 Cockpit Visualization: LIDIA . . . 126
B.4 Communication Protocol: MAVLink Integration . . . 127
B.4.1 The MARSH Custom Dialect . . . 127
B.5 Data Acquisition and Analysis Workflow . . . 128
B.5.1 Post-Processing in MATLAB . . . 128

List of Figures **129**

List of Tables **133**

List of Symbols **135**

List of Abbrevations **139**

Ringraziamenti **145**

1 | Introduction to Rotorcraft - Pilot Coupling

1.1. Background and Motivation

Rotorcraft, including helicopters and various hybrid configurations such as tiltrotors, are complex aerospace vehicles valued for their unique capabilities, notably Vertical Take-Off and Landing (VTOL) and sustained hovering flight. These operational characteristics often necessitate missions executed under demanding conditions, such as precision landings, hovering (with or without slung loads), tracking tasks, or autorotation [51]. Consequently, the safety and mission effectiveness of a rotorcraft are critically dependent on its *flying qualities* and the stability of the overall pilot-vehicle system, known as the Pilot-Vehicle System (PVS).

A significant challenge in the design and operation of rotorcraft is the potential for Rotorcraft-Pilot Coupling (RPC). RPC is an adverse, unwanted phenomenon originating from anomalous and undesirable couplings between the pilot and the aircraft/rotorcraft [51]. It typically manifests as inadvertent, sustained, and sometimes divergent oscillations. These can range from a degradation of the aircraft's Handling Qualities to instabilities (both oscillatory and non-oscillatory) or an increase in structural strength requirements [1, 50, 51].

Recent research, such as the ARISTOTEL project [4], has highlighted that while RPC events produce similar effects—ranging from pilot discomfort to catastrophic loss of the vehicle—the underlying causes vary significantly. Rigid Body RPCs typically dominate the $0-2$ Hz range, whereas Aeroelastic RPCs occur in the $2-8$ Hz range [21]. RPCs are generally considered more difficult to predict and suppress than Aircraft-Pilot Couplings (APCs), which are mainly associated with the lower frequency spectrum of flight modes [50, 51]. Thus, the term RPC is preferred as it accurately reflects the system-level nature of the coupling phenomenon [1]. Addressing and mitigating RPC is essential for enhancing rotorcraft safety, improving flying qualities, and reducing pilot workload across the operational envelope. Rotorcraft are considered more susceptible to RPC than fixed-wing aircraft are to APCs due to the prominent role of their high-order dynamics in the development of these phenomena [51].

1.2. Nature and Characteristics of RPC

RPC is fundamentally a closed-loop instability wherein the pilot, in an attempt to control the aircraft, inadvertently excites or sustains an oscillatory mode due to an undesirable mismatch between their control strategy and the vehicle's dynamic response [51]. The control input from the pilot to the rotorcraft can be conceptually decomposed into two components: voluntary action (intentional control to follow a desired trajectory) and involuntary action (inadvertent control input resulting from exogenous accelerations of the cockpit) [51, 54]. In the context of aeroelastic RPCs, the pilot acts as an inadvertent link between seat motion and controls, effectively behaving as a mechanical impedance [21].

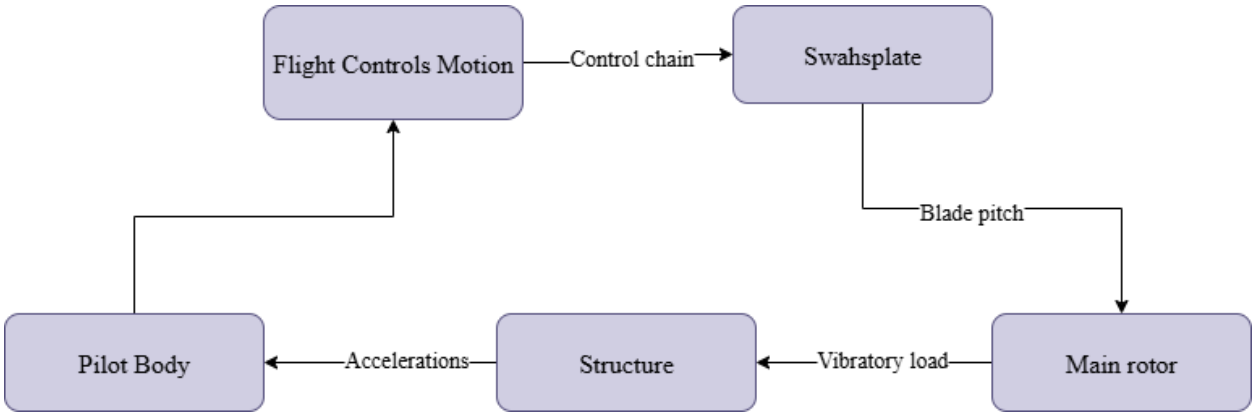


Figure 1.1: Schematization of the RPC closed loop (Source: Adapted from [66]).

1.2.1. Categorization of RPC

Following the established framework for analyzing Pilot-Vehicle Interactions, APC/RPC events are commonly classified based on the pilot's control activity (voluntary or involuntary contribution) [1, 51]:

1. **Voluntary (Active) Contribution:** Associated with the pilot consciously applying control inputs.
    - Pilot-Induced Oscillations (PIO): This occurs when the pilot, often misled by inconsistent or insufficient cues, inadvertently excites sustained or divergent vehicle oscillations by applying control inputs that are in counter-phase or have a phase lag with respect to aircraft motion [1, 51]. PIOs are characterized by low frequency ($0.5 - 1$ Hz) and high amplitude oscillations [51]. Recent flight test campaigns utilizing the Bell 205 have demonstrated that standard ADS-33 tasks can expose PIO tendencies, particularly when modified to increase task aggression or reduce tolerances [26]. PIOs are typically categorized into:
        - Category I PIO: Assumes linear behavior of the pilot and control system, resulting from high gains and increased time delay effects [1, 51].

  - Category II PIO: Involves limit cycle oscillations due to localized nonlinearities, such as rate or position limiting in the control elements [1, 51].
  - Category III PIO: Involves non-stationary and/or complex nonlinearities, often related to Flight Control System (FCS) mode switching [1, 51].
- Non-Oscillatory Event: A condition where the pilot and the FCS effectively work against each other [1, 51].

2. **Involuntary (Passive) Contribution:** Associated with the pilot's biomechanical response.
   - Biomechanical APC (Aeroelastic RPC): Often referred to as Pilot-Assisted Oscillations (PAO) in rotorcraft contexts. These oscillations arise when the pilot's biomechanical response is excited by cockpit motion (exogenous accelerations), leading to inadvertent control inputs that sustain or augment the vehicle's vibration level [1, 51]. They are characterized by high frequency ($1-3$ Hz for APC, or $2.5-8$ Hz for RPC type PAO) and varying amplitude oscillations [1, 51]. In these high-frequency ranges, the pilot becomes an unconscious link in the feedback loop, necessitating aeroelastic models for accurate representation rather than rigid body models [43].
   - A fourth category, Category IV APC, has been proposed for events caused primarily by structural modes and their interaction with the pilot [28], which are occasionally termed Aeroelastic RPCs [51].

1.2.2. Causative and Contributing Factors

The unique dynamics of rotorcraft, coupled with the complexity of modern flight control augmentation, contribute to their susceptibility to RPC. Key contributing factors include:

- **Time Delay and Phase Lag:** Rotorcraft exhibit high-order dynamics and large phase delays, which are often compounded by modern Fly-By-Wire (FBW) systems that introduce additional delays through digital filtering, control computers, and swashplate actuators [1, 51, 54]. The motion of the main rotor coning (at approximately 1/rev) and the regressive cyclic rotor mode can fall within the pilot's biomechanics or voluntary action bandwidth, making the time delay particularly critical [51]. The Loop Transfer Function of the pilot-vehicle system is highly sensitive to the main rotor coning motion, which significantly reduces the stability margins due to its damping factor [44, 54].
- **Control System Nonlinearities:** Actuator or control surface rate limits and high control sensitivity can be causal factors for low-frequency RPCs [51]. Additionally, insufficient collective control friction has been cited as a contributing factor in collective

bounce PAO events [51, 54].

- **Cross-Coupling and Vehicle Dynamics:** Rotorcraft are inherently dynamically unstable in key flight conditions, characterized by numerous control couplings [51]. Control inputs are transmitted through the swashplate, resulting in a flap response with nearly 90° phase delay (1/4 of the rotor revolution period) [51]. The collective bounce phenomenon, for instance, involves the interaction between the main rotor's coning mode and the control loop closure produced by the pilot's involuntary action [54].
- **Pilot Biodynamics:** Involuntary control input is quantified by the Biodynamic Feedthrough (BDFT), which is the transfer function relating the vehicle acceleration (input) to the control deflection (output) [51]. The frequencies associated with pilot biodynamic response ($0.5-10$ Hz) fall into the range of the vehicle response spectrum, enabling the unintended coupling [51]. BDFT is not unique; it varies between pilots and even for the same pilot based on neuromuscular activity, task instruction, and body orientation [43]. To model this linear behavior, rational representations of both BDFT and Neuromuscular Admittance (NMA) are often utilized, typically consisting of second-order filters in the band of interest ($1-10$ Hz) [43].

Understanding and predicting RPC requires a comprehensive analysis of the integrated pilot-vehicle system, recognizing that the susceptibility to coupling is an emergent property of the closed loop rather than a flaw in a single component [51]. RPCs involve the pilot, the vehicle, and a trigger initiation mechanism [51]. To this end, novel objective metrics like the Phase-Aggression Criterion (PAC) have been developed to detect PIO in flight by analyzing the phase distortion between pilot input and vehicle output alongside pilot aggression [26].

1.3. Examples of Rotorcraft-Pilot Coupling (RPC) Events

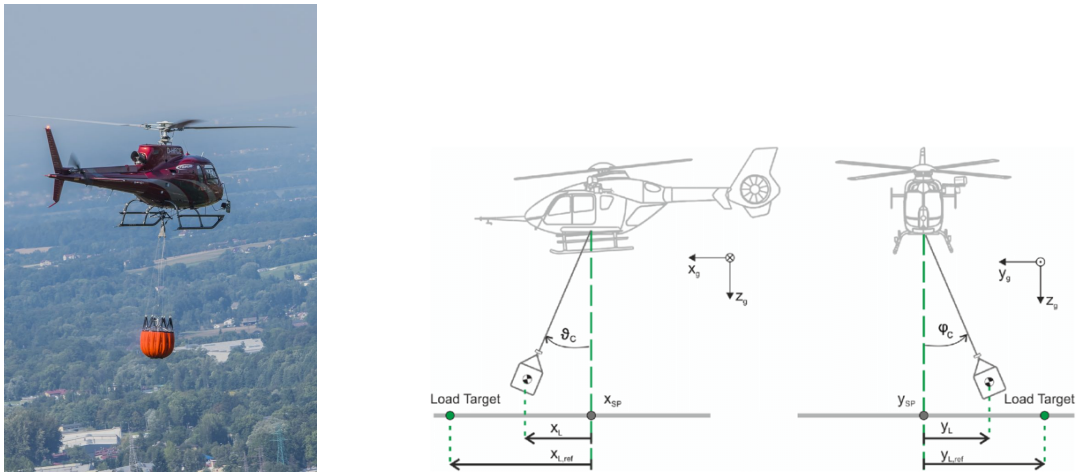
To fully comprehend the Rotorcraft-Pilot Coupling phenomenon, it is instructive to examine real-world scenarios where these adverse interactions have occurred. Accident history reveals that RPC events span a variety of aircraft types (Helicopter (H), Gyrocopter (G/C), Tiltrotor (T)) and distinct causes [51].

1.3.1. Slung Load Operations and Airframe Dynamics (Low Frequency RPC)

Rotorcraft-Pilot Couplings are known to be particularly critical in operations involving external loads, which introduce a low-frequency dynamic element [51].

- **Scenario:** A helicopter operating with a slung load, creating a complex dynamic system [51].

- **Mechanism:** The coupling can manifest as rotor/sling load bouncing [51], vertical bouncing via collective, or vertical bouncing via cyclic [51]. In a tiltrotor, the coupling between the rotor and the slung load is also a recognized RPC type [51].
- **Observed Consequences:** Multiple accidents have been linked to these couplings, such as the CH-47 experiencing rotor/sling load bouncing in 1968, the CH-53E encountering APC with flexible modes in precision hover with heavy sling loads (Category I to Category II PIOs) in 1978, and the CH-53G with flexible modes/sling loads resulting in PAO in 1980 [51]. Tiltrotors like the V-22 have also experienced PAO related to flexible modes and slung loads [51].
- **RPC Category:** Classification varies between low-frequency PIO (voluntary action) and high-frequency PAO (involuntary/aeroelastic coupling) [51].



(a) (b)

Figure 1.2: Figure 1.2a presents the characteristic situation involving a sling load, exemplified by a water bucket positioned beneath the helicopter. A corresponding schematization detailing the load's structure and movement is provided in Figure 1.2b. (Source: adapted from [45])

1.3.2. FBW and Time Delay Issues (Nonlinear RPC)

The introduction of modern systems, such as FBW, can introduce new mechanisms for RPC, often related to time delays and control law complexities [54].

- **Scenario:** Operation of modern, highly-augmented rotorcraft, particularly those equipped with FBW systems.
- **Mechanism:** FBW systems introduce time delays due to stick filtering and control computers, potentially exceeding 100 ms in some experimental vehicles [54]. These delays, coupled with inadequate vehicle dynamics, can cause the pilot to inadvertently

excite oscillations [51]. An example is the UH-60 ADOCS, which experienced PIO in 1988 due to excessive time delays [51].

- **Observed Consequences:** In a high-gain task (e.g., night training, sand, brownout), an initial vertical oscillation triggered by ground contact—such as that experienced by the Danish Air Force Leonardo Helicopters AW101 in 2014—can be exacerbated [51]. Another instance is the Sikorsky S-97 Raider accident in 2017, which suffered extreme roll oscillations as the flight control software transitioned from ground to air modes during takeoff [51].
- **RPC Category:** PIO (voluntary action), often Category I or III when related to mode switching [51].



Figure 1.3: An example of highly augmented rotorcraft dynamics, the UH-60's advanced controls may reach rate limits during rapid, high-load maneuvers, causing a sudden change in effective vehicle dynamics and potential for PIO/RPC. (Source: Lance Cpl. Samantha Rodriguez, Public domain, da Wikimedia Commons)

1.3.3. Collective Bounce (High Frequency Aeroelastic RPC)

Collective Bounce is a specific type of Aeroelastic RPC (or PAO) that occurs along the vertical (heave) axis [54].

- **Scenario:** The pilot holds the collective control inceptor, typically during hover or autorotation.
- **Mechanism:** An oscillatory perturbation of the rotor thrust produces vertical vibrations of the airframe and cockpit [54]. This vertical vibration excites the pilot's

biomechanics through the seat and floor. This involuntary motion of the pilot's left hand and the collective inceptor feeds back into the rotor thrust, closing an adverse control loop and further exciting the thrust perturbation [54]. This constitutes an involuntary control loop closed by the pilot along the vertical axis [54].

- **Tiltrotor Specifics:** While in helicopters the key factor is the reduction of phase margin in the collective pitch-heave loop (often due to main rotor coning), in tiltrotors (such as the XV-15 or AW609), the phenomenon is driven by the interaction between the pilot's biomechanics and the airframe's Symmetric Wing Bending (SWB) mode [43]. In tiltrotors, it is the depletion of the gain margin, rather than the phase margin, that typically leads to instability, manifesting as a resonance between the pilot's biomechanical pole and the poorly damped first SWB mode [43].
- **Observed Consequences:** Accidents have been caused by collective bounce on UH-1B helicopters, leading to severe vertical oscillations (often described as a "hop or a bounce") during autorotation [51, 54]. The issue is magnified when the collective control friction is insufficient [51, 54]. The Bell 525 prototype crash in 2016 was also related to unanticipated severe vibrations at a frequency of 6 Hz, where biomechanical feedback contributed to sustaining and amplifying the vibration [51].
- **RPC Category:** RPC type PAO, specifically an Aeroelastic RPC [51, 54]. The problem is often complicated by the rotor's coning motion, which drastically reduces stability margins [44, 54].

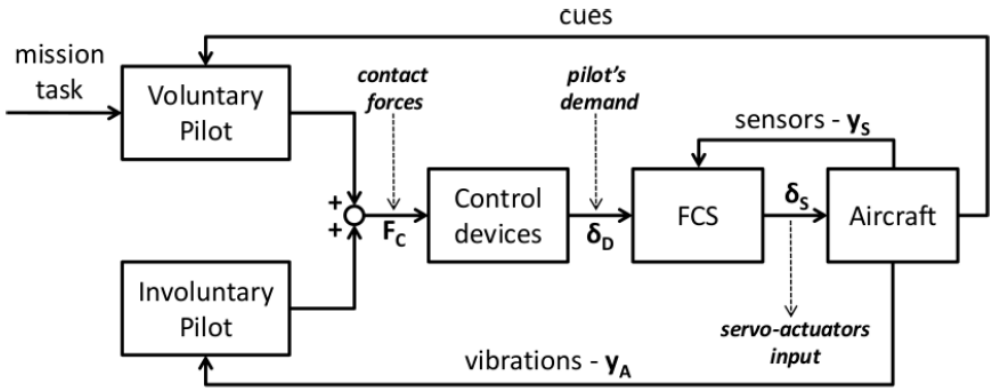


Figure 1.4: Flow block diagram of the PVS (Source: Adapted from [43]).

1.3.4. Shipboard Operations (Operational Environment RPC)

Shipboard recovery presents a uniquely challenging operational environment wherein visual and environmental factors can trigger RPC events.

- **Scenario:** A helicopter attempting recovery to a ship deck, particularly in high sea states or Degraded Visual Environments (DVE).

- **Mechanism:** The combination of irregular ship motion (roll, pitch, heave), airwake turbulence, and obscuration of visual cues creates a high-workload environment [41]. Pilots must aggressively track a moving landing spot, which can lead to high-gain control inputs. The lack of stable visual references forces pilots to rely on the moving deck, potentially inducing vertigo or erroneous control inputs [41].
- **Observed Consequences:** High-intensity ship motion can lead to unacceptable pilot workload (Bedford rating > 4) and unsafe conditions for fleet pilots [41]. Simulations using a BO-105 model indicated that without augmentation, the primary flight control configuration showed a tendency toward PIO during precision hover over the ship deck [41].
- **Mitigation:** Research indicates that advanced control laws (e.g., Translational Rate Command/Position Hold or Acceleration Command/Velocity Hold) combined with visual augmentation (e.g., Head-Mounted Displays with conformal symbology) can significantly reduce workload and mitigate PIO tendencies by providing stable references and simplifying the control task [41].



Figure 1.5: Example of a naval operation in which a helicopter attempts to land on the deck of ship. (Source: U.S. Navy photo by Mass Communication Specialist 2nd Class Rodrigo Caldas, Public domain, da Wikimedia Commons)

1.3.5. Conclusion: The Link Between Workload, BDFT, and RPC

The examples discussed highlight that Rotorcraft-Pilot Coupling is not a singular event but a complex class of instabilities arising from various physical and control-system mechanisms. However, a common denominator in the onset of these phenomena—particularly regarding Aeroelastic RPCs and Pilot-Assisted Oscillations (PAO)—is the breakdown of the effective dynamic interaction between the pilot and the vehicle.

Crucially, this interaction is not static. Recent research has demonstrated that *Biodynamic Feedthrough (BDFT)* is inherently *task-dependent* [27, 46]. As the mission difficulty and the associated *Mental Workload (MWL)* increase, the pilot instinctively alters their neuromuscular strategy to meet precision requirements. This is typically achieved through muscle co-contraction, which modifies the mechanical impedance of the upper limbs [66].

While this stiffening strategy is intended to improve voluntary control accuracy, it simultaneously alters the transmissibility of environmental accelerations through the pilot's body. This variation in neuromuscular admittance can inadvertently amplify the passive feedback loop (BDFT), thereby eroding stability margins and triggering RPC events [66]. Consequently, the assessment of pilot workload is not merely a performance metric but a fundamental variable for predicting and mitigating the risk of biomechanically-induced instabilities.

2 | Mental Workload and Performance Quantification in Advanced Flight Systems

The development of a comprehensive physiological sensor system yields a wealth of data applicable to diverse research domains. A primary area of application lies in the development of methodologies for the objective assessment of MWL — a construct currently evaluated predominantly through subjective means. Consequently, it is first necessary to rigorously define the concept of MWL within the context of flight operations and establish the theoretical framework in which it is situated.

2.1. Conceptualisation and Theoretical Framework of Mental Workload

The rigorous definition and comprehensive understanding of Mental Workload (MWL) are pivotal to the field of human factors engineering, particularly within safety-critical environments such as modern aviation. Despite its centrality, MWL remains a complex and often elusive construct, with no universally accepted definition across scientific literature [37, 39].

2.1.1. Evolution of the Workload Concept

Historically, the term "workload" originated primarily in reference to the demands of physical labour. However, its modern scientific connotation has undergone a significant paradigm shift towards the cognitive domain [39]. This evolution is strongly correlated with the widespread implementation of automation technologies, which have fundamentally altered the role of the human operator from that of a direct *executor* of tasks to a sophisticated *supervisor* of complex, automated systems [39].

MWL is generally conceptualised as a multidimensional construct, encompassing a heterogeneous collection of phenomena related to cognitive demand, affective states, and the inherent psychophysiological response to environmental and systemic stresses [39]. The core theoretical challenge lies in distinguishing whether MWL represents the *demands* imposed by the

task, the operator's *effort* to meet those demands, or the resulting *performance* [39]. Contemporary models predominately operate under the Multiple-Resource Theory framework, postulating that mental resources are not a single reservoir but are multi-dimensional, drawing from distinct pools (e.g., perceptual, cognitive, response) [39].

The practical consequences of excessive cognitive load in flight operations are profound, potentially leading to performance degradation, compromised mission safety, and long-term detriment to aircrew health [39].

2.2. The Evolving Pilot Role in Automated Cockpits

The transition to automated flight decks, while contributing to a historic reduction in overall transport-category aircraft accident rates, has introduced new and complex challenges in Human-System Interaction (HSI) [30].

2.2.1. The Automation Paradox and Safety Implications

The technological evolution leading to the modern two-pilot cockpit has significantly increased system reliability [30]. Paradoxically, despite these technological enhancements, human error remains the predominant contributing factor to flight accidents, accounting for up to 80% of total occurrences within the last two decades [30]. This phenomenon, often termed the automation paradox, underscores that the human element remains the critical safety barrier. Pilots are now tasked with supervising complex systems, requiring them to effectively manage attention, allocate cognitive resources, and maintain high levels of Situation Awareness (SA) to successfully monitor automated systems, diagnose failures, and execute timely, informed decision-making [30].

2.2.2. Future Operational Concepts

Economic and logistical pressures, including a growing global pilot shortage, are driving the industry toward highly complex operational paradigms such as Reduced Crew Operations (RCO) and, ultimately, Single-Pilot Operations (SPO) in commercial transport aviation [30]. These concepts increase reliance on robust automation, but inherently elevate the individual pilot's cognitive load and the complexity of the HSI. Consequently, the development of refined methodologies for real-time, adaptive workload assessment is critical for the safe implementation of these next-generation flight deck designs [30].

2.3. Multimodal Methodologies for MWL Assessment

Effective MWL assessment necessitates a comprehensive approach, typically categorised into three primary domains: subjective, behavioural (performance), and physiological measures [37]. The limitations of subjective post-task evaluations (prone to retrospective bias) and the intermittency of discrete behavioural performance metrics necessitate the use of continuous, objective monitoring techniques. The physiological approach has therefore gained significant traction for its potential to provide objective, continuous data on the operator's real-time cognitive and affective state [37].

2.3.1. Psychophysiological Metrics: Mechanisms and Correlates

A recent scoping review corroborates the high prevalence of psychophysiological data collection in contemporary MWL research, appearing in nearly 70% of assessed studies [30].

Neurophysiological and Oculomotor Measures

- **Neurophysiological Measures (EEG):** Electroencephalography captures brain activity. Spectral power changes in specific frequency bands are key correlates of workload. For instance, an increase in Theta Power (typically $4 - 8$ Hz) in frontal regions is often linked to memory and focused attention demand, while a decrease in Alpha Power (typically $8 - 12$ Hz) in parietal regions is associated with increased cognitive effort and resource engagement [30, 37].
- **Oculomotor Measures:** Metrics such as blink rate, fixation duration, and pupil dilation provide reliable, non-invasive indicators of attention allocation and cognitive processing load. Reduced blink rate and increased pupil diameter are established indicators of heightened MWL [30].

Autonomic and Somatic System Measures

- **Cardiovascular Measures (ECG/HRV):** These metrics reflect the activity of the Autonomic Nervous System (ANS), which modulates cardiac function in response to cognitive and emotional stress. High workload typically results in an increase in Heart Rate (HR) and a significant decrease in Heart Rate Variability (HRV). Specifically, reductions in High Frequency (HF) power and increases in the Low Frequency (LF) to High Frequency (HF) ratio (LF/HF) of the HRV spectrum are strong indicators of sympathetic activation associated with mental effort [30, 37].
- **Electrodermal Activity (EDA/GSR): Skin Conductance (SC)**, derived from EDA, tracks minute changes in sweat gland activity, providing a robust, direct measure of sympathetic nervous system arousal and emotional intensity associated with stress

and cognitive effort [37].

- **Electromyography (EMG):** While often used to assess physical fatigue, EMG, particularly the Root Mean Square (RMS) value, can serve as a somatic proxy for psychological stress and workload. Increased cognitive load often leads to an involuntary increase in muscle tension (e.g., in the forearm, neck, or shoulder muscles), which is captured by the RMS-EMG amplitude, reflecting a state of heightened arousal and effort [19].

Table 2.1: Selected Physiological Parameters and Correlation Trends with Increasing Mental Workload

Physiological System	**Measure/Feature**	**MWL-Specific Metric Detail**	**MWL Trend**
Cardiovascular	Heart Rate (HR)	Beats Per Minute (BPM)	Increase (↑) [37]
	Heart Rate Variability (HRV)	High Frequency (HF) Power	Decrease (↓) [37]
	Heart Rate Variability (HRV)	LF/HF Ratio	Increase (↑) [37]
Autonomic Nervous System	Electrodermal Activity (EDA)	Skin Conductance Level (SCL)	Increase (↑) [19, 37]
Somatic / Musculoskeletal	Electromyography (EMG)	Root Mean Square (RMS) Amplitude	Increase (↑) [19]
Neurophysiological	EEG Activity	Frontal Theta Power	Increase (↑) [37]
	EEG Activity	Parietal Alpha Power	Decrease (↓) [37]
Eye activity	Fixations (HR)	Period of time when gaze remains at a particular location	Increase (↑) [37]
	Saccades	Small, rapid movements between fixations	Decrease (↓) [37]
	Blink rate	Full or partial eye closure frequency	Increase (↑) [37]
	Pupil diameter	Pupil size measure	Increase (↑) [37]

2.3.2. MWL in Complex Multitask Activity: The Role of Expertise

The efficacy of a multimodal approach, incorporating somatic measures, was demonstrated in a study of helicopter pilots engaged in demanding, simulated multitask missions [19]. By monitoring workload, skin conductance (EDA), and RMS-EMG, the research established distinct psychophysiological profiles based on pilot expertise:

- **Expert Pilots:** Demonstrated greater physiological stability, with only slight increases

in measured parameters despite high task difficulty. Their subjective MWL estimates remained low to moderate, and their emotional state was consistently linked to low-intensity positive emotions. This reflects a more efficient cognitive reserve and superior capacity for resource allocation [19].

- **Non-Expert Pilots:** Exhibited a direct and strong correlation between increasing task demand, perceived workload, and rapidly rising physiological values (EDA and EMG). Their emotional profiles were notably more volatile, fluctuating between positive and negative emotions with greater intensity variations, indicative of higher stress levels and less controlled performance [19].

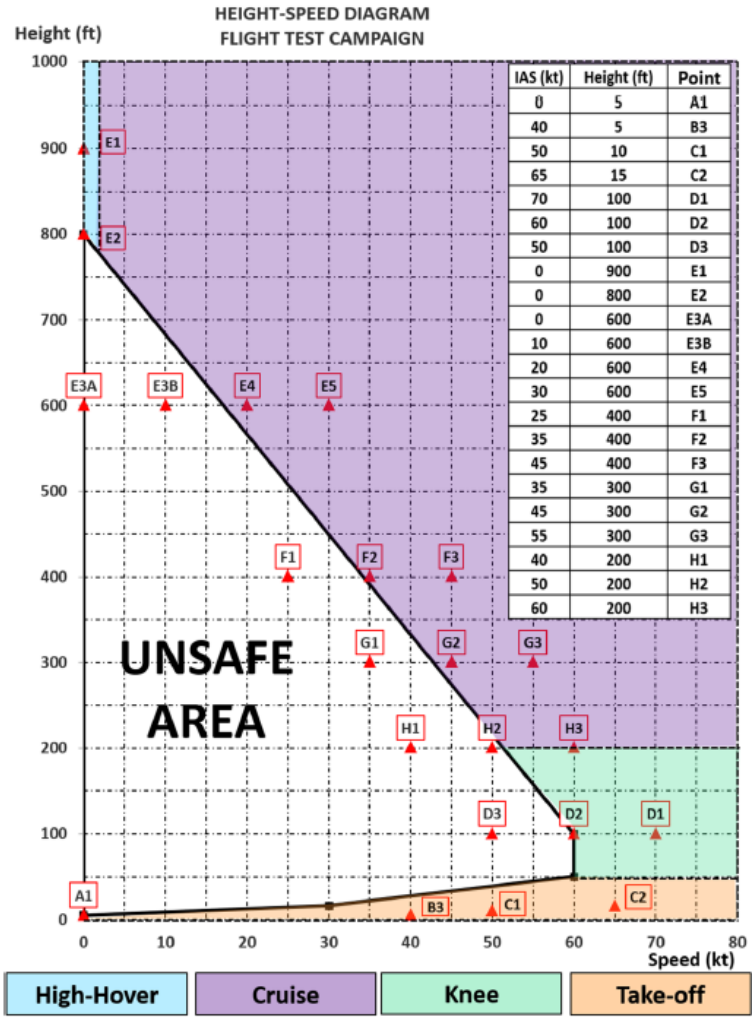
This evidence suggests that expertise acts as a buffer against physiological manifestation of stress, maintaining stability in operational performance through efficient internal resource management [19].

2.3.3. MWL in Extreme and Complex Helicopter Operations

The assessment of MWL is critical during flight conditions that impose maximal cognitive stress, such as emergency procedures and precision shipboard landings.

Workload during Emergencies (Autorotation)

Procedures following a sudden engine failure in a single-engine helicopter, specifically the autorotation manoeuvre, impose an exceptionally high cognitive load on the pilot [56]. The safety margins for executing this manoeuvre are governed by the aircraft's Height-Velocity (H-V) diagram, commonly referred to as the "Dead Man's Curve". Given the subjective methods traditionally used for assessing difficulty near this curve, extensive flight tests have been conducted to establish quantitative physiological parameters that accurately reflect the workload endured by pilots during autorotation [56]. These studies confirm the feasibility of using instrumented pilots and physiological metrics to objectively evaluate cognitive and stress loads in life-critical scenarios.



IAS (kt)	Height (ft)	Point
0	5	A1
40	5	B3
50	10	C1
65	15	C2
70	100	D1
60	100	D2
50	100	D3
0	900	E1
0	800	E2
0	600	E3A
10	600	E3B
20	600	E4
30	600	E5
25	400	F1
35	400	F2
45	400	F3
35	300	G1
45	300	G2
55	300	G3
40	200	H1
50	200	H2
60	200	H3

Figure 2.1: Height-Speed Diagram and the four partitions proposed, i.e., High-hover, Cruise, Knee, and Take-off. The table in the upper right corner shows the height and speed combinations tested during the test campaign as well as their different encodings (Letter - Number) (Source: Adapted from [7]).

Shipboard Landing and the Role of Visual Cues

Helicopter shipboard landing is a cognitively complex task, inherently challenging due to high workload in an unstable, restricted environment [7]. Applied cognitive task analysis through pilot interviews identifies that the final phases of approach and landing are the most critical. Key factors affecting pilot performance and safety include:

1. Environmental factors (e.g., ship motion, airwake, sea state).
2. Aircraft systems and their reliability.
3. Organizational factors (e.g., communication, crew resource management).
4. The crucial role of external visual cues [7].

Reliance on accurate external visual cueing is vital for a successful landing, as pilots transition

from instrument flight to visual guidance in the most critical phases where workload is maximal [7].

2.4. Quantitative Performance and Control Activity Metrics

The ultimate evaluation of HSI effectiveness rests on the maintenance of safety margins and acceptable flight performance. The quantification and prediction of pilot workload are necessary for informing the operational envelope and evaluating handling qualities early in the design cycle, particularly in highly dynamic environments such as the Helicopter/Ship Dynamic Interface (HSDI) [8].

2.4.1. Objective Performance Metrics and Subjective Correlates

Operational capability is intrinsically linked to the pilot's subjective perception of both the workload and the aircraft's Handling Quality Ratings (HQRs) [8]. Standard assessment relies on HQRs, typically provided on a structured scale (e.g., the Cooper-Harper rating scale), which provides a qualitative measure of system usability and pilot acceptance [8]. These subjective ratings are typically correlated with objective performance metrics (e.g., tracking error, velocity deviations) and subjective Workload Ratings (WRs), such as the widely-used NASA Task Load Index (NASA-TLX), to achieve a robust, holistic assessment [30].

2.4.2. The Attack Chart Methodology: Objective Quantification of Pilot Control Effort

The Attack Chart methodology constitutes a powerful behavioural approach that objectively quantifies pilot control effort by transforming raw control input dynamics into a measurable workload profile [8]. This method is essential for evaluating operational limits in high-demand phases, such as the HSDI.

Theoretical and Mathematical Foundation

The core function of the Attack Chart is the objective classification of pilot control movements based on their two primary dynamic characteristics: amplitude (Δ) and the peak gradient (g_{pk}) [8]. The methodology posits that the distribution of control activity within the amplitude-rate space is directly indicative of the pilot's cognitive strategy and workload state.

The key parameter derived from the control input dynamics is the *attack parameter*, which formally defines the relationship between the rapidity and magnitude of a control input

increment. For a smooth ramp profile of a control input, as depicted in Figure 2.2, the attack parameter is defined as the ratio of the peak gradient (rate) to the total amplitude of the deflection:

$$\text{attack} = \frac{g_{pk}}{\Delta} \tag{2.1}$$

where Δ is the control deflection amplitude and g_{pk} represents the peak gradient during the control ramp increment. This ratio quantifies the pilot's control aggressiveness relative to the size of the required correction.

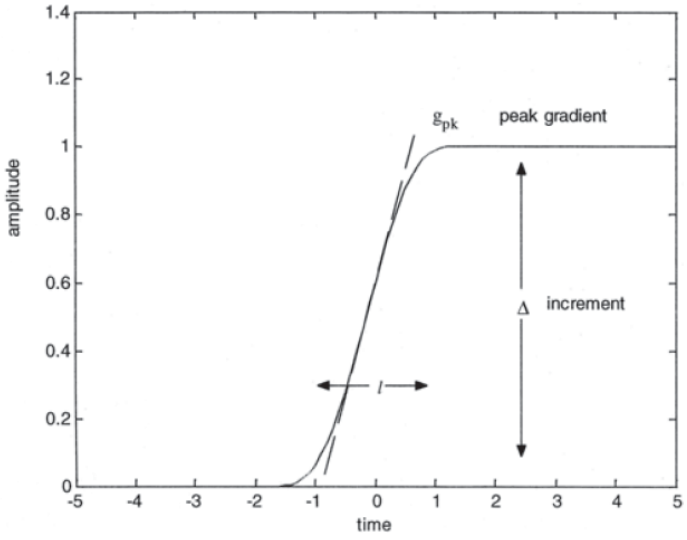


Figure 2.2: Definition of the parameters (Δ and g_{pk}) used to calculate the attack parameter during a smooth ramp control increment. This relationship quantifies the rapidity of the control action relative to its magnitude (Source: Adapted from [8]).

Classification Regions and Control Strategy Mapping

The Attack Chart defines four mutually exclusive regions using predefined empirical thresholds of control amplitude and rate (Δ vs. g_{pk}). Each region corresponds to a distinct pilot strategy and level of cognitive processing:

Region 1: Subguidance (x_1) Characterized by very low amplitude and high frequency. This activity is often associated with involuntary muscle noise or fine trimming, typically falling below the threshold of conscious control engagement.

Region 2: Guidance (x_2) The primary region of purposeful, deliberate control activity, reflecting the effort required to actively guide the vehicle along the assigned trajectory and meet primary mission objectives.

Region 3: Stabilization (x_3) Encompasses control inputs intended to correct for disturbances (external or internal). This signifies the continuous effort required to manage dynamic equilibrium.

Region 4: Super-stabilization (x_4) Defined by inputs of high amplitude and high rate. It is a critical behavioural marker of high workload and impending saturation, indicating the pilot is struggling to maintain control and reacting aggressively to prevent performance divergence [8].

Workload Metric Vector and Predictive Modelling

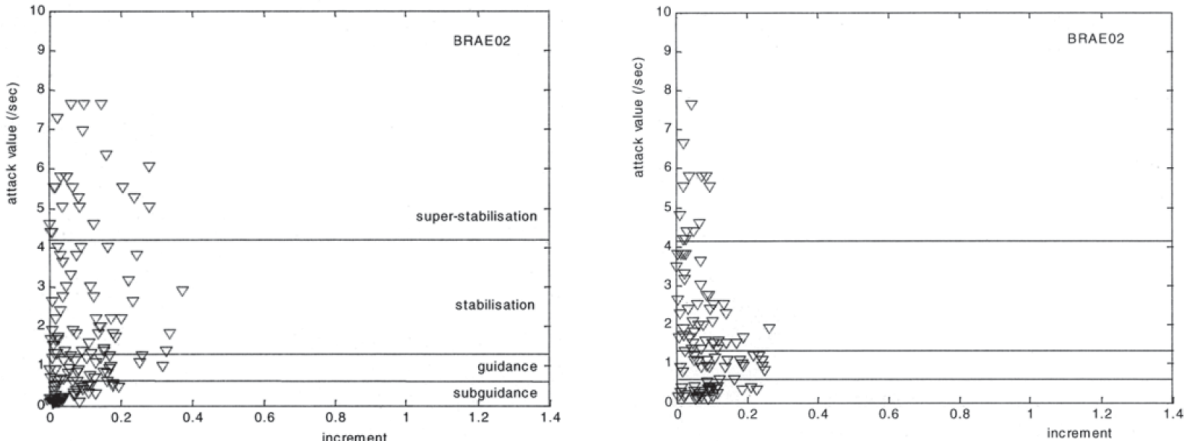
The process quantifies the control effort into a Workload Metric Vector $\mathbf{x}$:

$$\mathbf{x} = \{x_1, x_2, x_3, x_4\} \tag{2.2}$$

where x_i is the normalized count of individual control input events recorded in region i. This objective vector $\mathbf{x}$ is empirically validated against the pilot's subjective WR using non-linear machine learning techniques, specifically Classification and Regression Trees (CART). This allows for the generation of robust decision rules that predict the subjective WR based solely on objective control activity:

$$WR \approx f(\mathbf{x}, C) \tag{2.3}$$

where C may include contextual variables. This predictive capability is essential for defining safe operational limits during the design and simulation phases [8].



(a) Lateral Cyclic Stick Activity (b) Collective Stick Activity

Figure 2.3: Example of Attack Chart distribution for different helicopter controls in a dynamic manoeuvre: Figure 2.3a for the cyclic lateral stick and figure 2.3b for the collective stick [8]. The four distinct control effort zones (Subguidance, Guidance, Stabilization, and Super-stabilization) are clearly (Source: Adapted from [8]).

2.5. Conclusions

The complex relationship between Mental Workload and pilot performance determines the safety margins of modern aviation. The shift toward higher automation and challenging operational concepts (RCO, SPO, HSDI, emergency procedures like autorotation) mandates increasingly precise and objective assessment methods [30, 56]. The current state-of-the-art relies on a sophisticated multimodal assessment framework, integrating validated physiological markers—spanning from neurophysiological (EEG) and autonomic (HRV, EDA) measures to somatic (EMG) indicators—with robust behavioural and control-activity metrics, such as those derived from the mathematically-defined Attack Chart methodology [7, 8, 19, 37]. Continued research is essential to refine these predictive models, ensuring that technological advancements enhance, rather than compromise, the operational effectiveness, resilience, and safety of the human-automation partnership.

3 | Workload measurement techniques and study methods

The assessment of physical and cognitive workload in helicopter pilots, particularly under critical conditions such as RPC or situations leading to Biodynamic Feedthrough (BDFT) and Pilot-Assisted Oscillations (PAOs), necessitates the use of objective and non-invasive techniques [66] in conjunction with subjective metrics like the Bedford scale or NASA-TLX. This chapter presents various methodologies that can be used for physiological data acquisition and could subsequently be used for the evaluation of Mental Workload (MWL), applicable in both simulated and real-world environments, highlighting their respective advantages and limitations.

3.1. Surface Electromyography (sEMG)

Surface Electromyography (sEMG) is a pivotal instrument for investigating bioelectrical signals generated by skeletal muscles and detected at the skin surface [6]. The sEMG signal provides a critical insight into both the motor function (the muscle) and its controller (the nervous system), enabling a deeper understanding of neuromuscular control mechanisms and physiological adaptations in response to high task demands [6]. Research indicates that muscle activity, as quantified by sEMG, increases proportionally with flight task difficulty and overall pilot workload [66]. This increase is attributed to the activation of motor units to modulate mechanical impedance in response to vibrations and demanding tasks, an effect typically manifested as a stiffening of the affected body segments [66].

3.1.1. Principles of Signal Generation and Detection

The sEMG signal originates from the depolarization of muscle fibers, which generates Motor Unit Action Potentials (MUAPs). Each MUAP represents the temporal and spatial summation of individual Action Potentials (APs) propagating bidirectionally along the muscle fibers upon neural stimulation [6]. These propagating APs act as sources of a rapidly changing electric field within the body's biological volume conductor. The electrical potential detected on the skin surface, known as the Interferential EMG Signal, is the complex superposition (algebraic sum) of contributions from multiple, spatially and temporally asyn-

chronous MUAPs, alongside noise and various interferences [6, 14]. This aggregate electrical signal contains the inherent muscle signal, inevitably contaminated by various noise sources or artifacts [14].

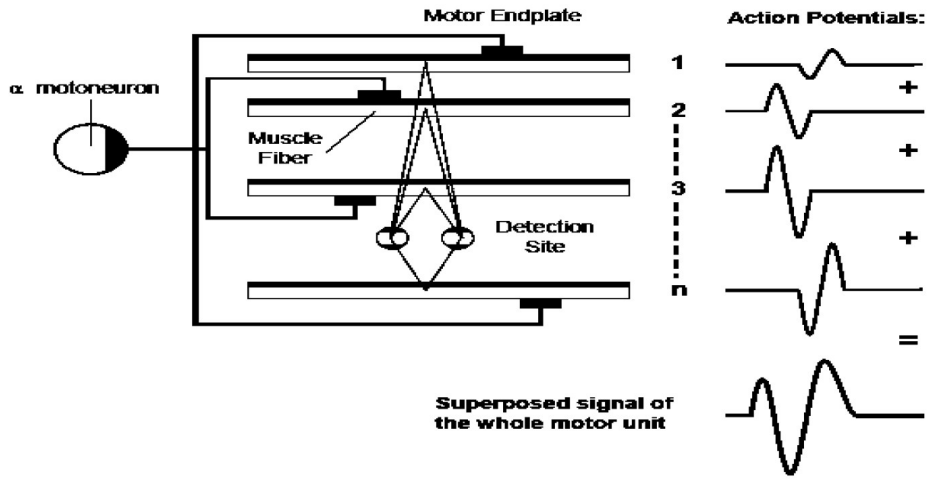


Figure 3.1: Conceptual diagram illustrating the propagation of muscle action potentials and their superposition to form the sEMG interferential signal recorded at the skin surface. (Source: Adapted from [61])

While traditional differential techniques rely on detecting a single time-varying signal using a bipolar electrode pair (providing primarily temporal information), modern methodologies utilize linear or two-dimensional (2D) sensor arrays, known as High-Density sEMG (HD-sEMG). These arrays facilitate the acquisition of space-time images of the instantaneous potential distribution and the generation of sEMG feature maps on the skin. The HD-sEMG approach is particularly valuable for localizing activity, estimating muscle fiber Conduction Velocity (CV), and tracking complex muscle mechanics during dynamic tasks [6].

3.1.2. Workload Quantification via sEMG Features

In the context of ergonomics and movement analysis, the sEMG signal is analyzed to detect manifestations of muscle fatigue and alterations in motor control strategies associated with increased physical and operational pilot workload. Quantification relies primarily on features extracted from two analytical domains:

- **Amplitude Features (Time Domain):** These variables are directly proportional to the neural drive to the muscle, the number of active Motor Units (MUs), and their firing rate (recruitment and rate coding), thus reflecting the physical effort required by the pilot to manipulate flight controls. Key metrics include the Root Mean Square (RMS) and the Average Rectified Value (ARV). An increase in these values is typically correlated with higher physical workload or increased muscle co-activation, indicating

greater stabilization efforts or mechanical impedance modulation during high-precision tasks or RPC events [6, 66].

- **Spectral Features (Frequency Domain):** These features are computed from the power spectrum of the sEMG signal. Variables such as the Mean Spectral Frequency (MNF) and the Median Spectral Frequency (MDF) are critical indicators of the muscle's metabolic state. During prolonged or fatiguing contractions, the propagation velocity of APs along muscle fibers decreases. This physiological change causes a shift of the sEMG power spectrum towards lower frequencies, a phenomenon known as spectral compression. A significant decrease in MDF or MNF is considered the primary myoelectric manifestation of muscle fatigue [6].

3.1.3. Critical Factors: Innervation Zone and Electrode Placement

A critical factor for accurate and reliable sEMG analysis, especially in dynamic environments like a helicopter cockpit, is correct and stable electrode placement. The Innervation Zone (IZ) is the region on the muscle surface where motor neuron terminations connect with muscle fibers (Neuromuscular Junctions, NMJ) and where action potentials originate and diverge in opposite directions [6].

- **Effect of IZ:** Placing the differential electrode pair over or near the IZ is strongly discouraged [6]. This positioning results in signal cancellation (as signals generated by APs traveling toward one tendon are subtracted from similar signals traveling in the opposite direction), leading to attenuated amplitude values (ARV/RMS) and rendering the recorded signal highly sensitive to minor muscle movements or changes in electrode position.
- **Dynamic Artifacts:** In dynamic conditions, such as the continuous control adjustments required in helicopter piloting, the relative sliding between electrodes and underlying muscle tissue can cause the IZ to shift beneath the electrodes [6]. This geometrical change can significantly modify recorded sEMG variables (e.g., amplitude and spectral shifts) in a manner that reflects a movement artifact rather than an actual change in muscle activation or fatigue.

Therefore, utilizing anatomical atlases, such as the *Atlas of Muscle Innervation Zones* [6], to identify muscle fiber orientation and the optimal location for electrode placement (typically midway between the IZ and the distal or proximal tendon) is indispensable for obtaining reliable activation and fatigue data. Adherence to established guidelines, such as those provided by the Surface EMG for Non-Invasive Assessment of Muscles (SENIAM) project, is essential.

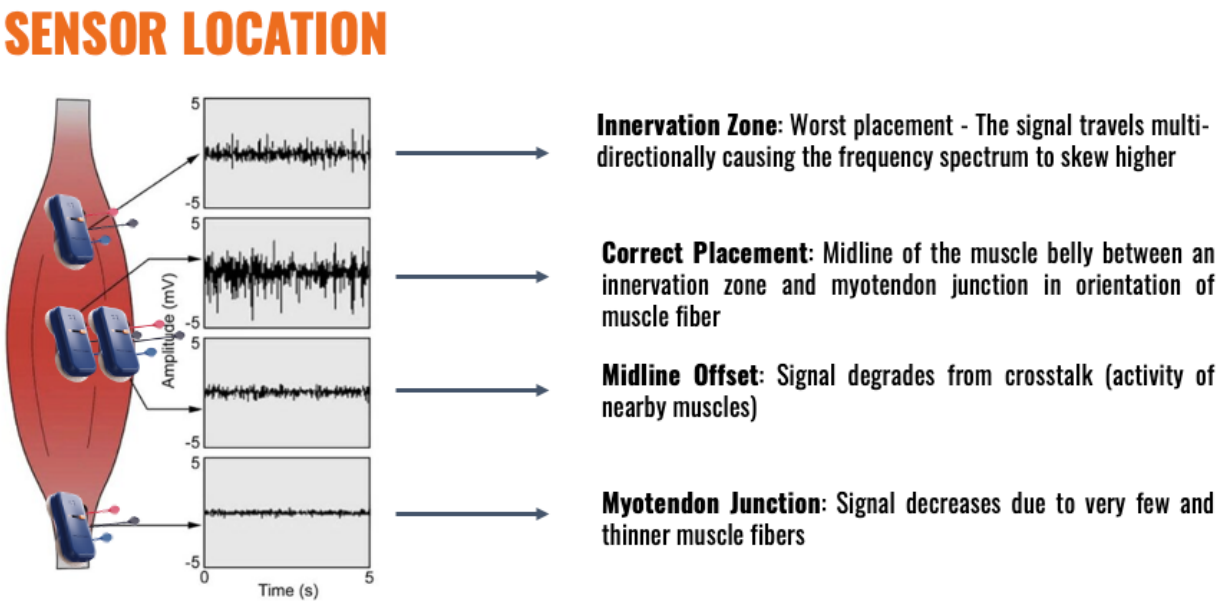


Figure 3.2: Illustration of the Innervation Zone (IZ) and the recommended electrode placement on the muscle belly to avoid measurement artifacts. The optimal position is typically between the IZ and the tendon. (Source: Posizionare elettrodi k-myo)

3.1.4. sEMG in RPC Phenomena

In the context of complex helicopter piloting tasks, sEMG could be employed to quantify the pilot's involuntary physical response to vibrations and high workload conditions, particularly concerning RPC and BDFT.

- The passive contribution to the control input, which can precipitate RPC phenomena, results from the involuntary response of the pilot's body to vibrations transmitted from the rotorcraft, primarily through the seat [66].
- This passive contribution is critically influenced by the active (voluntary) control efforts required by the pilot, especially during tasks demanding high precision or under intensive workload conditions [66].
- The Central Nervous System (CNS) activates muscles not only to provide motion control but also to alter their mechanical impedance by modulating the contraction of agonist and antagonist muscle pairs (co-contraction) [66]. This physiological increase in impedance, or muscle stiffening, is a natural response to enhance dexterity and counteract vibrational disturbances [6, 66].
- Increased muscle activity and co-contraction detected by sEMG indicate that the CNS is increasing the muscle's equivalent mechanical impedance, confirming an elevation in workload and task difficulty [66].
- Specifically, high-precision collective control (e.g., during ship-deck landings) involves

critical tasks where sEMG analysis of the upper limbs (forearm muscles like *flexor carpi ulnaris*, and arm muscles like *biceps brachii*) reveals an increase in activity strongly correlated with subjective workload ratings (e.g., Bedford scale) [66]. A concentration of activity in the forearm muscles has been observed particularly in highly experienced pilots [66].

- The experimental relationship established between admittance-control muscle activity and pilot workload confirms that sEMG can validate the physical demand placed on the pilot. This physiological data is crucial for enhancing the fidelity of numerical biomechanical models aimed at characterizing BDFT and predicting RPC issues, especially considering the influence of piloting style on coupling with aircraft dynamics [66].

3.2. Eye-Tracking in Helicopter Flight for Pilot Workload Assessment

3.2.1. Introduction to Eye-Tracking as a Workload Metric

Eye-tracking constitutes a robust experimental methodology used to record eye motion and gaze allocation over time and task [10]. By measuring where, how, and for what duration a person directs their gaze, it provides insight into the allocation of visual attention, which is intrinsically linked to underlying cognitive processes [10, 15, 23, 33]. This strong connection, often termed the *eye-mind link*, renders eye-tracking a reliable, objective, and non-intrusive tool for assessing the cognitive state and MWL of human operators in safety-critical environments such as aviation [17, 32, 33, 49, 59]. Researchers have also developed specialized protocols, such as the *Eye Tracking in Aviation (ETA)* technique, specifically to investigate the pilot's cognitive processes of attention and decision-making [34].

Relevance in Aviation and Helicopter Operations

In aviation, accurately predicting and evaluating pilot workload is a crucial factor in human-factor airworthiness, particularly given that human error contributes to a significant portion of aviation accidents [15, 17, 32]. The complex and dynamic nature of modern aircraft, including helicopters, requires pilots to monitor and process vast amounts of information, leading to high mental demands [15, 33].

Helicopter operations, specifically, often involve highly dynamic maneuvers (such as fast jet or rotorcraft operations [49]) that place significant and complex mental demands on the pilot, making the assessment of MWL vital [32]. While subjective assessments have traditionally been the primary method for pilot workload certification, physiological methods, such as those provided by eye-tracking, are increasingly recognized and accepted as reference stan-

dards, offering greater objectivity and potential for real-time monitoring [15, 17, 22, 32, 33].

3.2.2. Eye-Tracking Measures for Workload Assessment

The eye's physical movements—specifically fixations, saccades, and blinks—generate physiological data that could be correlated with pilot workload and attention allocation [15, 17, 32, 33, 59]. Different metrics derived from this data offer unique and often non-overlapping information regarding the pilot's cognitive state [17, 22].

- **Fixation and Dwell Measures:** A fixation is a period of relative ocular stillness during which the pilot gathers and processes visual information [32, 59]. An increase in workload often induces changes in fixation parameters, particularly their *duration* and *frequency* [32, 34, 59].
  - **Mean Fixation Time / Dwell Time:** This measure is considered one of the first parameters to change under stress [32]. Generally, a longer mean fixation duration (or dwell time) is interpreted as an increase in *processing effort* or *task difficulty* [17, 32, 33]. For instance, one study observed that mean fixation time exhibited an increasing trend as workload increased across cruise, approach, and landing phases [17].
  - **Fixation Frequency / Number of Fixations:** High MWL can decrease fixation frequency, suggesting focused, deliberate processing, or conversely, may increase it due to greater visual information demand [15, 17, 32–34]. An increase in the *number of fixations* (or fixation density) has been linked to increased attention and processing [17, 33].
- **Saccade Measures:** Saccades are the rapid eye movements between fixations [32, 59]. The movement of the eyes between instruments and displays (scanning behavior) provides insight into information demands and attention management strategies [32, 33].
  - **Saccade Frequency:** This metric, related to how often the eyes move, often exhibits an inverse trend to mean fixation time, frequently declining as workload increases [17, 59]. In one study, saccade frequency was found to be notably lower during the landing phase compared to cruise and approach [17].
  - **Mean Saccade Length (or Amplitude):** This refers to the distance covered by the eye during a saccade. A decrease in mean saccade length has been consistently observed in relation to higher workload (e.g., manual flight) [15, 32]. This decrease suggests a more localized and efficient, goal-oriented visual search and scanning strategy to conserve cognitive resources during demanding tasks [15]. Conversely, larger saccadic movements were observed in conditions with higher automation

levels, indicating a more extensive or relaxed visual search pattern when cognitive load is reduced [16].

  - **Transition Frequency / Rate:** This metric specifically quantifies the shift of gaze between different cockpit displays or Areas of Interest (AOIs) [15]. Changes in this measure can indicate fluctuations in the pilot's Situation Awareness (SA) and the rate of information acquisition and updating [15]. Research suggests that a decrease in transition frequency may occur during high workload, indicating more efficient and task-oriented behavior [15].

- **Pupil and Blink Measures:**
  - **Pupil Diameter / Dilation:** Pupil size is a highly reliable measure, often serving as an index of the amount of *cognitive processing* and *mental effort* [17, 22, 32–34, 49]. Pupil dilation typically increases with higher workload as more mental resources are deployed to handle task demands [17, 49]. A limitation is its strong dependence on ambient light conditions [15].
  - **Blink Rate and Duration:** The endogenous (non-reflexive) eye blink is sensitive to demands for visual attention [22]. Blink rate is generally shown to decrease during periods of high visual workload [22]. In a study involving actual flights, blink rates were significantly lower during Instrument Flight Rules (IFR) conditions, which are associated with high visual demand, compared to Visual Flight Rules (VFR) segments [22].

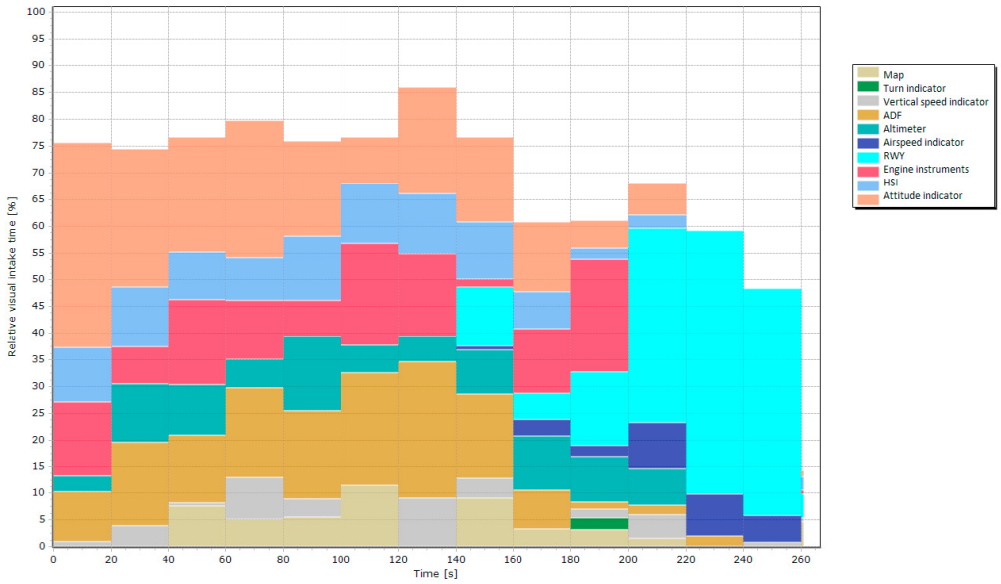


Figure 3.3: Example of eye tracking measurement: percentage of total dwell time on individual Areas of Interest (AOIs) during an NDB approach for an experienced pilot. (Source: Adapted from [22])

3.2.3. Eye-Tracking in Flight Environments

Eye-tracking technology, particularly modern head-mounted systems, is well-suited for deployment in real-world or simulated flight environments. The successful implementation of these systems in aviation research relies on a structured approach that encompasses the physical equipment, the analytical mapping of the cockpit, and the design of the experimental tasks. Specifically, this methodology revolves around three key considerations:

1. **Hardware and Setup:** Mobile, *head-mounted eye-trackers* (often referred to as 'eye-tracking glasses' [49, 59]) enable participants to move their heads freely, which is crucial during dynamic flight tasks [32]. These systems record the pilot's visual scan behavior in relation to the instruments and the outside environment. The technology tracks pupil and corneal reflections to estimate gaze position [32, 49]. The continuous development of techniques like the ETA further facilitates scientific research of cognition and decision-making in flight simulators [34]. However, challenges exist regarding fitting and calibration, especially under headsets [49], and issues with glare or shadows affecting markers [49]. Ideally, the system should be integrated into a flight helmet for greater stability and accuracy, minimizing the need for constant recalibration [49].

2. **Areas of Interest (AOIs):** In the cockpit, specific instruments and windows (e.g., Head-Up Display (HUD), Primary Flight Display (PFD), Multi-Function Displays (MFD), and the Out-The-Window view) are defined as AOIs to monitor the allocation of visual attention [32, 33, 49]. The HUD, in particular, often commands significant attention due to its consolidation of critical flight information [33, 49]. Analyzing AOI dwell time and transition frequency between these areas can clearly differentiate how attention shifts between focusing on flight parameters and monitoring the external environment.

3. **Workload Scenarios:** To effectively assess metrics, scenarios must be designed to elicit varying and measurable levels of MWL [15].

    - **High Workload:** Often induced by critical flight phases (takeoffs/landings [22]), IFR operations [22], high-speed conditions [22], unexpected failures [32], or secondary tasks (e.g., n-back, arithmetic tasks) that overload cognitive resources [15, 49].
    - **Low Workload:** Typically associated with less demanding phases like cruise flight or ground-based baselines [22].

3.2.4. Eye-Tracking and Attentional Tunneling

Attentional Tunneling is a cognitive state characterized by an *excessive, involuntary focus* on one source of information or goal to the disregard of other critical factors [15]. This state is

strongly linked to human error accidents, such as Controlled Flight Into Terrain (CFIT) [15]. Eye-tracking is a crucial tool for studying this phenomenon by identifying visual patterns indicative of narrowing attention [15].

- **Detection through Gaze Metrics:** Tunneling is hypothesized to manifest as changes in visual scanning behavior. Metrics such as a decrease in transition frequency (fewer switches between AOIs) and a decrease in gaze entropy (more predictable, less random gaze patterns) could signal that the pilot's attention has excessively narrowed to a specific display or task [15].
- **Classification:** Machine learning algorithms (such as Support Vector Machines (SVM) or Logistic Regression [15]) can be trained using eye-tracking metrics to potentially classify the occurrence of tunneling states in real-time [15]. This capability is essential for developing "pilot-aware cockpits" that can provide adaptive support to mitigate safety risks [15].

3.3. Heart Rate and Heart Rate Variability for Workload Evaluation

Among the various physiological signals available, cardiac activity, specifically Heart Rate (HR) and Heart Rate Variability (HRV), is considered the most significant and practical indicator of cognitive load in aviation contexts [48].

3.3.1. Heart Rate (HR) as an Indicator of Pilot Stress

Heart rate is modulated by the Autonomic Nervous System (ANS). In the context of flight operations, an increase in task demand or psychological stress typically triggers the sympathetic nervous system, resulting in an accelerated heart rate. Research conducted on a SW-4 helicopter simulator demonstrated that pilot HR increases monotonically with the difficulty of flight maneuvers (e.g., slalom tasks performed under varying weather conditions) [29]. This study further established a link between increased mental stress (indicated by elevated HR) and changes in the pilot's control strategy, specifically an increase in the natural frequency (ω_n) and damping ratio (ζ) of the pilot's neuromuscular system model [29].

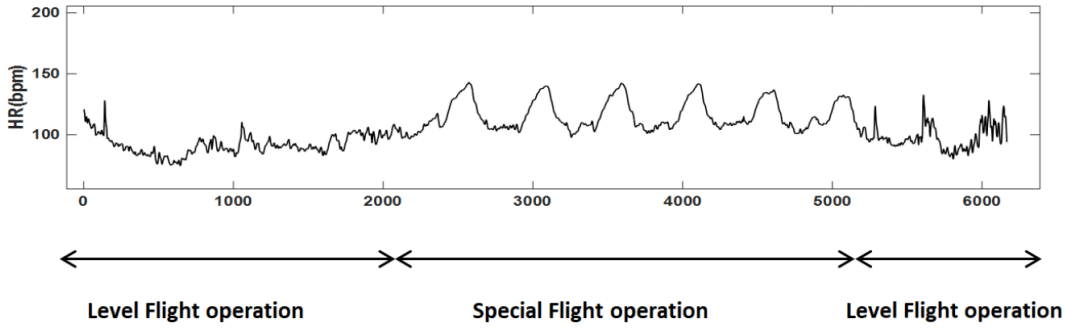


Figure 3.4: Typical Heart Rate profile during complex special flight operations, showing distinct phases of physiological stress [57]. The figure illustrates three distinct flight phases. (Source: Adapted from [57])

In real flight conditions involving complex special operations, pilot HR has been observed to exhibit significant fluctuations, reaching instantaneous peaks of over 150 bpm during high-G maneuvers [57]. However, for transient flight maneuvers where standard HRV analysis may be unstable, alternative metrics such as the "area of the heart rate curve" have been proposed to quantify stress intensity, which tends to decrease exponentially as pilots adapt to the task through repeated training [57].

3.3.2. Heart Rate Variability (HRV) Metrics

While HR provides a gross measure of arousal, HRV—the variation in time intervals between consecutive heartbeats (RR intervals)—offers a more nuanced insight into the interplay between the sympathetic and parasympathetic branches of the ANS. Generally, a suppression of HRV is associated with increased mental effort and cognitive demand [37].

HRV features used in pilot workload assessment are typically categorized into time-domain and frequency-domain metrics:

- **Time-Domain Features:** Common metrics include the Standard Deviation of NN intervals (SDNN) and the Root Mean Square of Successive Differences (RMSSD). In real helicopter cross-country flights, statistical analysis has shown that these features exhibit significant differences across flight phases, with RMSSD generally decreasing during high-workload phases such as approach and landing [70]. Similarly, in flight tests using a Bell 205 helicopter, mean RR intervals and RMSSD were found to decrease as target tracking difficulty increased [63].
- **Frequency-Domain Features:** These include Low Frequency (LF) power ($0.04 - 0.15$ Hz), High Frequency (HF) power ($0.15 - 0.4$ Hz), and the LF/HF ratio. HF power is often associated with parasympathetic (vagal) activity and tends to decrease under high mental workload, while the LF/HF ratio is used to estimate the sympathovagal balance [48].

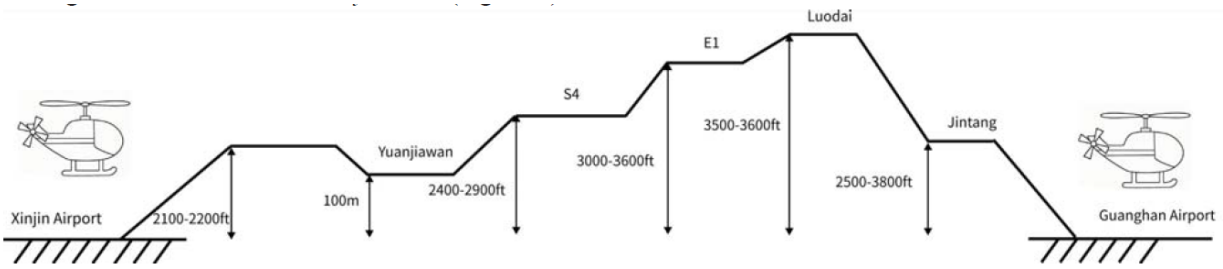


Figure 3.5: Flight route and altitude profile used for real-world mental workload assessment, correlating flight phases with physiological responses (Source: Adapted from [70]).

It is noted that during simulated IFR tasks, HRV has been reported to be more sensitive to mental workload variations than raw HR, which may be confounded by physical effort [37].

3.3.3. Classification of Workload using Machine Learning

Recent studies have moved beyond simple statistical correlation to using machine learning algorithms for the automatic classification of pilot workload based on ECG features. In a study involving real cross-country flights on an R44 helicopter, Photoplethysmography (PPG) derived HRV features were used to classify workload across takeoff, cruise, and landing phases. The study found that the Random Forest (RF) algorithm achieved the highest Area Under the Curve (AUC) of 0.934, while K-Nearest Neighbors (KNN) achieved the highest accuracy of 85.9% [70].

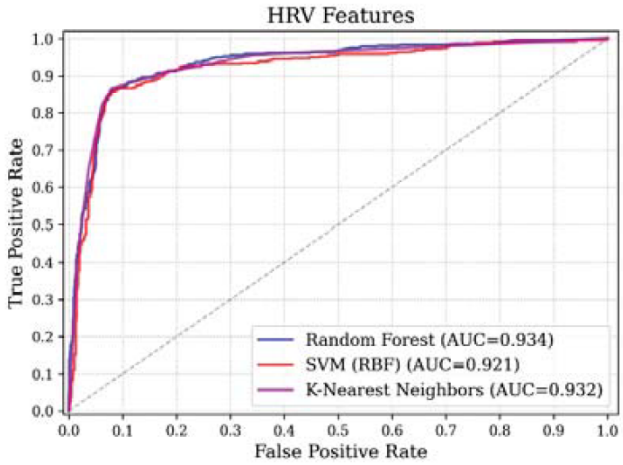


Figure 3.6: Comparison of machine learning algorithms (RF, KNN, SVM) for pilot workload classification using HRV features in real flight conditions (Source: Adapted from [70]).

Furthermore, when comparing physiological modalities, ECG-derived metrics have shown superior performance in regression models compared to EEG for detecting in-flight changes in helicopter pilot workload. A study using SVM regressors on Bell 205 flight data reported a lower cross-validation Mean Squared Error for ECG ($MSE = 0.17$) compared to EEG

($MSE = 0.29$), suggesting that cardiac measures may provide a more robust and practical metric for the electro-mechanically noisy helicopter environment [63].

However, the context of the flight is crucial. While acute workload increases HR and decreases HRV, long-duration flights inducing fatigue may show different patterns, such as a decrease in average HR and an increase in HRV time-domain indices like RMSSD, as observed in long-duration simulation studies [48]. Therefore, a comprehensive assessment system must distinguish between acute mental workload and cumulative fatigue.

3.4. Body Pose Estimation and Tracking

Accurate estimation and tracking of the three-dimensional (3D) human body pose from video streams is a fundamental task in computer vision, finding applications in diverse fields such as gaming, intelligent video surveillance, and health care systems [58]. In the context of aerospace human factors, particularly RPC phenomena, a markerless, view-invariant system for pose tracking offers a non-intrusive method to analyze pilot behavior and movements by focusing on specific body segments, such as the arm manipulating the collective inceptor.

3.4.1. Foundation of Markerless Pose Estimation

Human pose estimation is fundamentally challenging due to issues such as object occlusion, self-occlusion, variations in human motion, and the high Degrees of Freedom (DOFs) of the human body configuration [42, 52]. Early methods often relied on conventional intensity cameras, which proved limited under dynamic environmental conditions, such as severe illumination changes and shadows [31, 52]. The recent advent of low-cost depth cameras (e.g., Microsoft Kinect, Asus Xtion) has provided a significant advancement, as depth information is generally more robust to these environmental variations [31, 52]. These cameras provide 3D measurements from a single viewpoint, effectively mitigating ambiguities caused by the projection of human motion onto a 2D camera plane and alleviating some self-occlusion problems [52].

Methodologies for human pose recognition can be broadly classified into two main categories:

- **Learning-based Methods:** These approaches rely on large databases of training data to train classifiers for body part recognition [31, 52]. While highly accurate, their computational complexity may restrict their applications and impede real-time performance [52].
- **Model-based Methods:** These involve fitting a predefined human body model to the input data to estimate the pose [52]. A common approach is to employ an articulated cylinder model composed of segments (head, torso, arms, legs) connected by joints [52, 52]. To manage the total of up to 25 DOFs for poses [52], a hierarchical model

fitting method is often adopted, wherein a central part (like the torso) is detected first, followed by the estimation of the limbs relative to it [42, 52].

Visual-based Systems (Monocular Camera)

Visual-based systems often process the input video sequence through a pipeline involving 2D segmentation, 2D tracking, and finally 3D tracking and pose reconstruction (as illustrated in Figure 3.7) [52].

1. **2D Segmentation:** This step involves separating the human figure from the background, often using background subtraction techniques like a Gaussian Mixture Model (GMM) [52]. This yields frames for silhouette, edge, and motion [52].
2. **2D Tracking:** This stage is crucial for locating 2D feature blobs (e.g., head, hands, and feet) by combining appearance, color, and temporal information [52].
    - **Appearance Cues:** Often obtained through skeletonization, a procedure that extracts a skeleton graph from the silhouette of the human body [52].
    - **Color Information:** Acquired using tracking methods like Mean Shift Tracking to compute the next possible 2D blob locations [52].
    - **Temporal Prediction:** Used to handle severely occluded cases by predicting the next 2D location based on the Exponentially Weighted Moving Average (EWMA) of the blobs' locations from previous frames [52].
3. **3D Tracking and Reconstruction:** The tracked 2D feature locations are used to estimate an initial 3D pose [52]. The final 3D pose reconstruction is achieved by iteratively minimizing a cost function $F(S_{image}, S_{model})$ that measures the match between the projected 3D model and 2D image features (silhouette, edge, motion, and feature points) using a nonlinear optimization technique like the downhill simplex algorithm [52]. The result of the 3D pose is then fed back to assist 2D tracking for the next frame's prediction and skeletonization seeds [52].

Depth-based Systems

Systems utilizing depth cameras frequently embed the human model within a probabilistic tracking framework, such as the Particle Filter [52]. This sequential Monte Carlo method is well-suited for non-linear and non-Gaussian dynamic systems like human motion [52]. The process involves:

1. **Initialization:** Calibrating the human model and setting an initial pose, often a T-pose, to generate the initial set of samples (particles) [52].
2. **State Prediction:** Propagating the samples from the previous frame to the current

one by adding Gaussian noise and applying kinematic constraints to restrict the search space [52].

3. **Weight Calculation (Measurement Model):** The core step where each sample's weight is determined by calculating the average Euclidean distance between the observed depth data points and the surface of the cylinder model defined by the sample's state vector [52]. A refinement is often introduced to filter out noise by considering the number of depth points associated with the sample [52].

4. **Resampling and State Estimation:** Eliminating samples with small weights (degeneracy problem) and concentrating on those with large weights [52]. The final estimated state is the weighted sum of the remaining samples [52].

This hierarchical approach combined with the particle filter avoids iterative solutions like the Iterative Closest Point (ICP) algorithm, contributing to real-time performance without requiring a Graphics Processing Unit (GPU) [52].

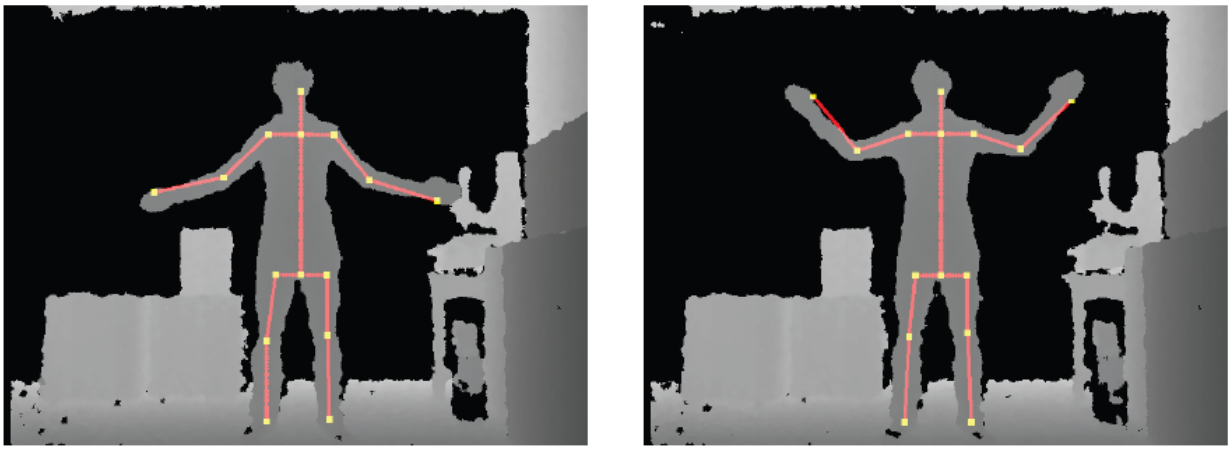


Figure 3.7: Overview of the proposed view-invariant 3D human body pose reconstruction system from a monocular video camera. (Source: Adapted from [52])

3.4.2. Application to Collective Inceptor Tracking in RPC for multibody models validation

The challenge of analyzing pilot movements in a rotorcraft during an RPC event requires precise, non-invasive measurement of the pilot's control activity. The movement of the collective inceptor is primarily driven by the left arm, making the tracking of the left arm's pose a key indicator of pilot input and potential workload.

Tracking the Left Arm Pose

For the purpose of tracking the left arm, which is expected to have a relatively high degree of motion, the body pose estimation system must be robust to:

- **Self-Occlusion:** The pilot's left arm may be occluded by the torso or other objects in the confined cockpit environment. Depth-based systems inherently handle this better than visual-only systems [52]. However, a failure condition is noted in depth-based tracking when one body part is too close to another, such as when the lower arm touches the torso, leading to inaccurate or fused detection [31, 52].
- **Confined Environment/Background:** The collective inceptor and the cockpit itself act as a complex, fixed background. The use of a depth camera is beneficial here as it naturally distinguishes the pilot (foreground) from the simulator/cockpit (background) based on depth value differences [31].

A hybrid approach, leveraging the strengths of both monocular video and depth data, would be ideal for a robust system. The articulated human model segments the body into components, including the upper and lower arms [52].

The state vector for the left arm would specifically track its 4 DOFs: the rotation parameters of the upper and lower arm [52].

Motion Analysis in RPC

The motion of the collective inceptor is directly reflected by the angles and position of the left arm joints (shoulder, elbow, wrist). Specifically:

- **Joint Trajectory Accuracy:** The output of the 3D pose estimation is the estimated position of key joints, such as the left elbow and left wrist, which directly inform the motion of the collective stick. The accuracy of the estimated joints is typically measured by the average Euclidean distance error (in pixels or meters) between the estimated position and the ground truth [31, 42, 52]. For depth-based methods, the average tracking error for each key joint is reported to be around 0.06 meters with a standard deviation of 0.04 meters [52].
- **Temporal Dynamics:** The analysis would not only focus on the instantaneous pose but also the temporal distribution of the left arm's motion parameters. Tracking methods utilize a motion model (e.g., Particle Filter) to maintain temporal continuity in the pose estimation [42, 52]. Increased frequency or magnitude of corrective inputs from the left arm (and thus the collective) during RPC can be quantified from the tracked joint velocities and accelerations, indicating higher pilot workload and compensatory effort. The use of a Kalman filter can be employed to predict and update the distance between joints, which helps to minimize errors in joint estimation [31].

The precise tracking of upper limb kinematics, synchronized with video-derived keypoint data, establishes a robust framework for cross-correlating pilot physiological and behavioral metrics. Furthermore, this multimodal approach facilitates the identification of data anoma-

lies and artifacts that may arise from idiosyncratic piloting maneuvers.

Additionally, the positional data acquired from the tracking system serves as a critical empirical baseline for the verification and validation of biomechanical multibody models designed to simulate human in-flight dynamics.

3.5. The Correlation Between Pilot Workload and Control Inceptor Pressure

Workload can be directly correlated with the risk of Loss of Situation Awareness (LoSA) and the onset of RPCs [68]. Recent efforts focus on developing objective, non-intrusive tools that provide real-time data.

3.5.1. Grip Pressure Evaluation: From Workload to Optical Sensing

Solid evidence indicates that a pilot's cognitive and physical effort, or stress, is directly correlated with the force exerted on control inceptors [12]. As the difficulty of a Mission Task Element (MTE) increases, involuntary muscle tension rises, leading to a consistently higher average grip pressure. This physiological response provides a valuable, objective metric for pilot-vehicle system analysis, independent of subjective self-assessment.

Experimental simulation tests confirm this relationship, identifying the Root Mean Square (RMS) and variance (σ^2) of the total grip pressure signal as reliable indicators of pilot effort. Specifically:

- **Task Dependency and Disturbance:** Testing with increased motion disturbance frequencies (e.g., 3.5 Hz versus 4.5 Hz) or tighter tracking thresholds resulted in significant increases in both the RMS and variance of the grip force signal [68]. This total pressure variance notably spikes when transitioning from a steady cruise to a highly demanding task, such as precision hovering [20].
- **Metric Correlation:** These objective force metrics demonstrate a strong correlation with validated control-input workload indices, including the Aggression Parameter and Moving Median Absolute Deviation [12].

To accurately and objectively capture this crucial pressure data, the OPT-IN sensor technology was developed. This non-contact pressure sensor transduces mechanical contact into a measurable electrical signal by exploiting the optical phenomenon of Total Internal Reflection (TIR).

TIR occurs when an electromagnetic wave traveling through a denser medium (characterized

by a higher refractive index, n_1) encounters an interface with a less dense medium (lower refractive index, n_2) at an angle exceeding the critical angle. Under these conditions, the wave is completely reflected back into the denser medium. Concurrently, an evanescent wave is generated, which decays exponentially into the less dense medium [68]. The OPT-IN sensor operates on the principle of Frustrated Total Internal Reflection (FTIR): when a third, denser medium (such as an elastic probe) is introduced into the evanescent field, the TIR is frustrated. This allows light energy to be transmitted out of the initial medium and subsequently measured by a photoresistor.

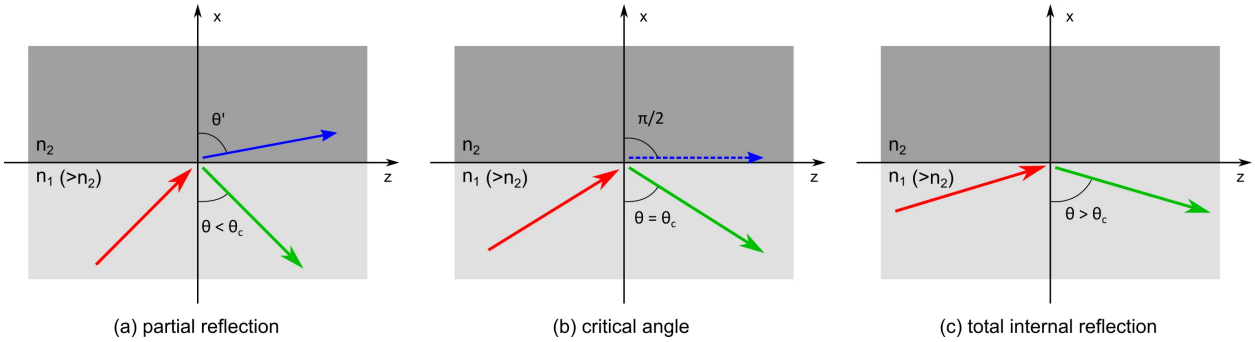


Figure 3.8: Diagram illustrating the Total Internal Reflection (TIR) and the evanescent wave. When the incident angle is greater than the critical angle, light is completely reflected. (Source: Conceptual diagram based on optical physics described in [68]).

3.6. Evaluation of Pilot Workload: The Bedford Workload Scale

The assessment of pilot workload is crucial for aviation safety, particularly when evaluating new operating techniques, aircraft designs, and flight deck automation [55]. Despite the array of objective and physiological techniques available, subjective rating scales remain an integral component of workload evaluation due to their reliability in capturing the pilot's internal experience. Foremost among these tools, particularly in the flight test environment, is the Bedford Workload Scale.

3.6.1. Conceptual Basis and Structure

Workload Definition and the Spare Capacity Concept

The Bedford Scale is a ten-point ordinal rating system developed at the Royal Aircraft Establishment (RAE) Bedford by Roscoe and Ellis in the late 1970s [55]. Its primary objective was to provide a more reliable and structured method for in-flight subjective workload assessment than unstructured pilot opinion.

This scale is founded on the definition that:

> *"Pilot workload is the integrated mental and physical effort required to satisfy the perceived demands of a specified flight task."* [55]

The practical implementation of this definition relies on the concept of *spare capacity* [55]. Instead of quantifying the pilot's total effort, the scale prompts the pilot to judge how much reserve capacity remains to take on "additional relevant but secondary tasks," such as monitoring other crew members, making radio calls, or managing systems [11, 55]. This intuitive focus on what the pilot *could* still do is what makes the metric highly consistent for experienced aviators. This approach is leveraged by modern analytical tools, such as the Spare Capacity Operator Estimator (SCOPE), which uses this concept to predict Handling Qualities Ratings (HQRs) by establishing quantitative workload metrics related to the best-case task-execution workload [5].

Hierarchical Decision Tree and Rating Categories

Structurally, the Bedford Scale intentionally parallels the successful hierarchical decision tree of the Cooper-Harper HQR scale. The ordinal scale ranges from 1 (lowest workload) to 10 (highest workload). The pilot navigates three main binary (Yes/No) decision points to arrive at four principal workload bands, which define the limits of performance and tolerability:

1. **Was it possible to complete the task?** (Leads to the Impossible category, Rating 10).
2. **Was workload tolerable for the task?** (Leads to the Possible category, Ratings 7–9).
3. **Was workload satisfactory without reduction?** (Leads to the Tolerable/Satisfactory categories, Ratings 1–6).

The categories of workload, anchored by specific spare capacity descriptors, are defined as follows:

1. **Satisfactory (Ratings 1–3):** Workload is considered low or insignificant. Rating 3 is defined as having "Enough spare capacity for all desirable additional tasks."
2. **Tolerable (Ratings 4–6):** The pilot has insufficient, reduced, or "little spare capacity." While adequate attention to additional tasks is possible, the level of effort required to maintain performance is increasing. Rating 6, representing the limit of tolerable workload, indicates that the pilot only has "little spare capacity: level of effort allows little attention to additional tasks."
3. **Possible (Ratings 7–9):** Workload is very high, and the maintenance of effort is becoming difficult. Rating 9 is reserved for "Extremely high workload. No spare capacity. Serious doubts as to ability to maintain level of effort."

4. **Impossible (Rating 10):** The task is abandoned, and the pilot is "unable to apply sufficient effort," representing an outright loss of control or task failure.

The explicit nature of these discrete, anchored descriptors is crucial for standardizing subjective judgment and minimizing the "scale-loading" issues observed in simple linear scales [11].

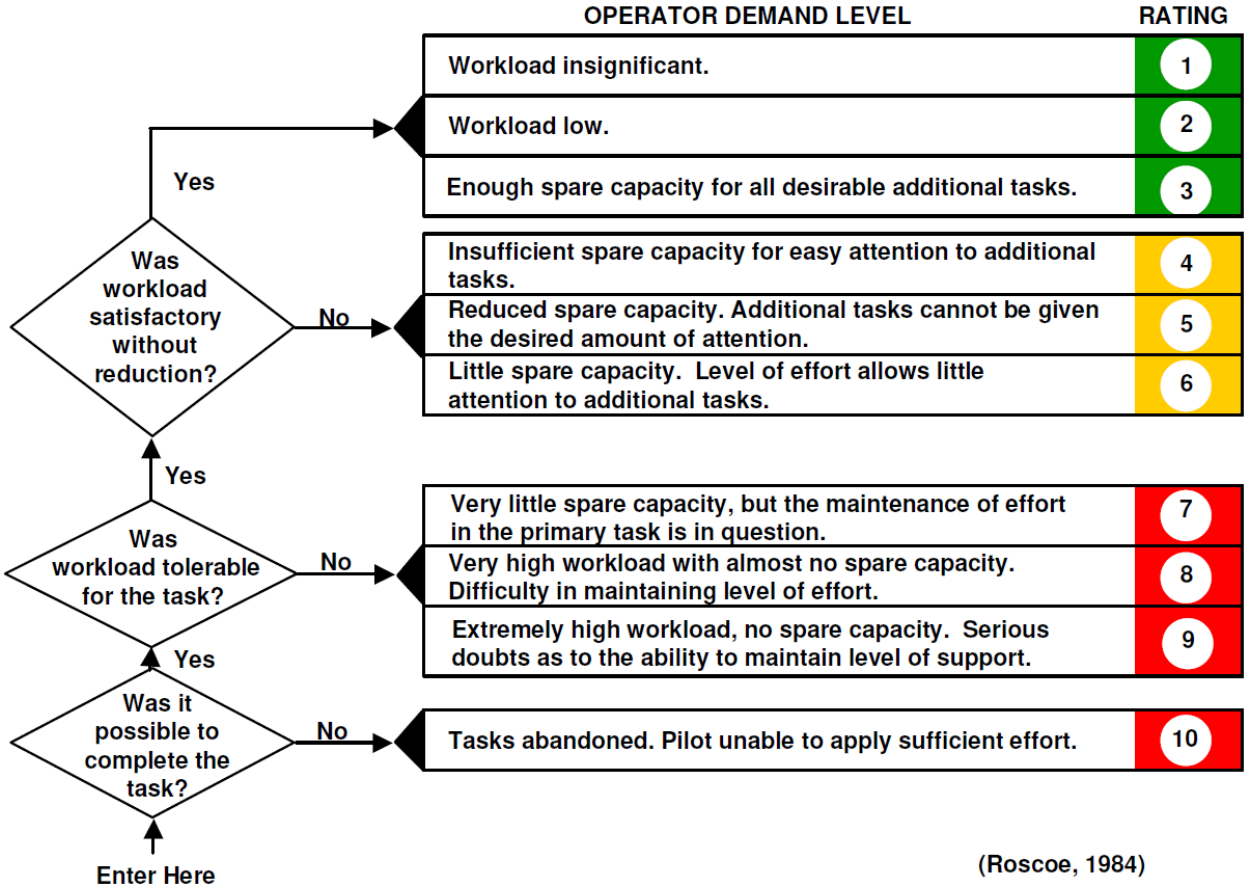


Figure 3.9: Structure of the Bedford Workload Scale (BWS). The scale uses a sequential decision tree to convert a pilot's qualitative judgment of control and spare capacity into a standardized numerical rating. (Source: Adapted from [11, 55])

3.6.2. Operational Use and Methodological Considerations

Empirical Validation and Operational Success

The Bedford Scale has proven its utility across diverse, real-world flight test environments. Its operational success includes:

- **Physiological Correlation:** The scale demonstrated a reasonably good correlation with objective stress indicators, most notably the pilot's heart rate response, achieving approximately 80% agreement for the same flight task among tested pilots [55].
- **Aircraft Evaluation:** It was successfully used during crew complement certification

(e.g., the BAC 146) and comparative studies of advanced aircraft, such as the Boeing 767 versus the Boeing 737. These studies used the scale to clearly distinguish between workload levels associated with different flight modes (e.g., hand-flying versus autopilot with Flight Management System integration) [55].

Methodological Limitations and Temporal Augmentation

Despite its practical strength, a rigorous interpretation of Bedford Scale results requires acknowledging its limitations:

- **Ordinality and Statistical Rigor:** As an ordinal scale, it does not possess interval properties. This means standard statistical processes, while often used, may provide results that are difficult to interpret rigorously, as the perceived difference between Rating 6 and 7 is not necessarily the same as the difference between 2 and 3.
- **Lack of Diagnostic Power:** The scale provides a high-level, aggregate assessment of workload. It lacks the dimensionality to diagnose the specific source of the workload (e.g., primarily visual, auditory, or cognitive), a capability offered by multi-dimensional tools like the NASA-TLX [11].
- **Ambiguity of Spare Capacity:** The core construct of "spare capacity" remains prone to individual interpretation. Pilots may define it differently (e.g., available time versus mental bandwidth), which can introduce individual variability in absolute ratings [11].
- **Critical Temporal Demand Omission:** A significant finding in recent research pertains to the scale's omission of time pressure as an explicit dimension. Wang et al. (2024), utilizing the Bedford Scale augmented by a supplemental time pressure survey for traffic pattern tasks, definitively concluded that while the classic scale correlates positively with predicted models, the "consideration of time pressure can effectively improve the consistencies" between theoretical predictions and subjective evaluations [65]. This highlights that in modern, time-compressed aviation tasks, the necessity of augmenting the classical Bedford scale with a dedicated temporal dimension is evident.
- **Expertise Skew:** Highly proficient pilots tend to anchor their ratings toward the lower end of the scale, as their increased skill reduces the felt effort for a given task. This reinforces that the scale's primary and most reliable function is for comparing [5] between design alternatives or different mission segments, rather than making absolute judgments about workload [11, 55].

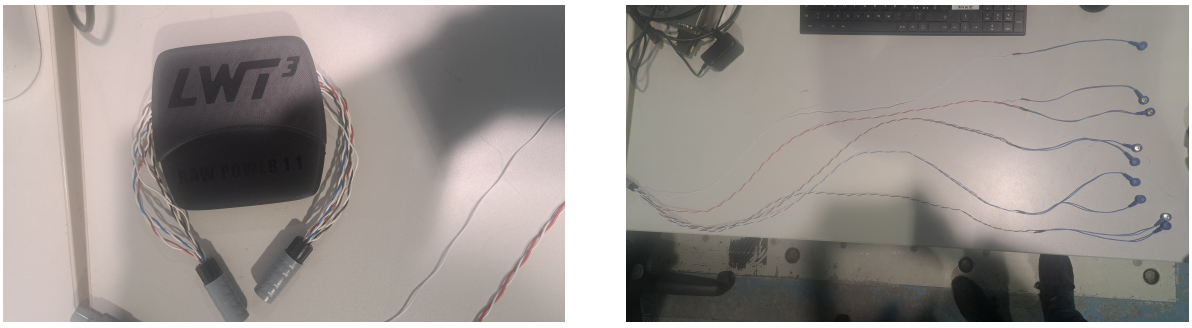
4 | Experimental setup: physiological sensors

In order to conduct the experimental campaign, starting from the theoretical foundations outlined in the previous chapters, the instrumentation used aligns with that of the simulations. In particular, the experimental activities will make extensive use of the RPC test rig (Appendix A) and the MARSH architecture [40] (Appendix B) to handle sensor management and the associated telemetry.

4.1. sEMG measures

4.1.1. Description of the sEMG Acquisition System (Raw-Power)

The Surface Electromyography (sEMG) signals were acquired using the Raw-Power system (supplied by LWT-3) [38]. This dedicated platform was selected for its high fidelity and accuracy in capturing dynamic muscle activity, a crucial factor for assessing pilot performance.



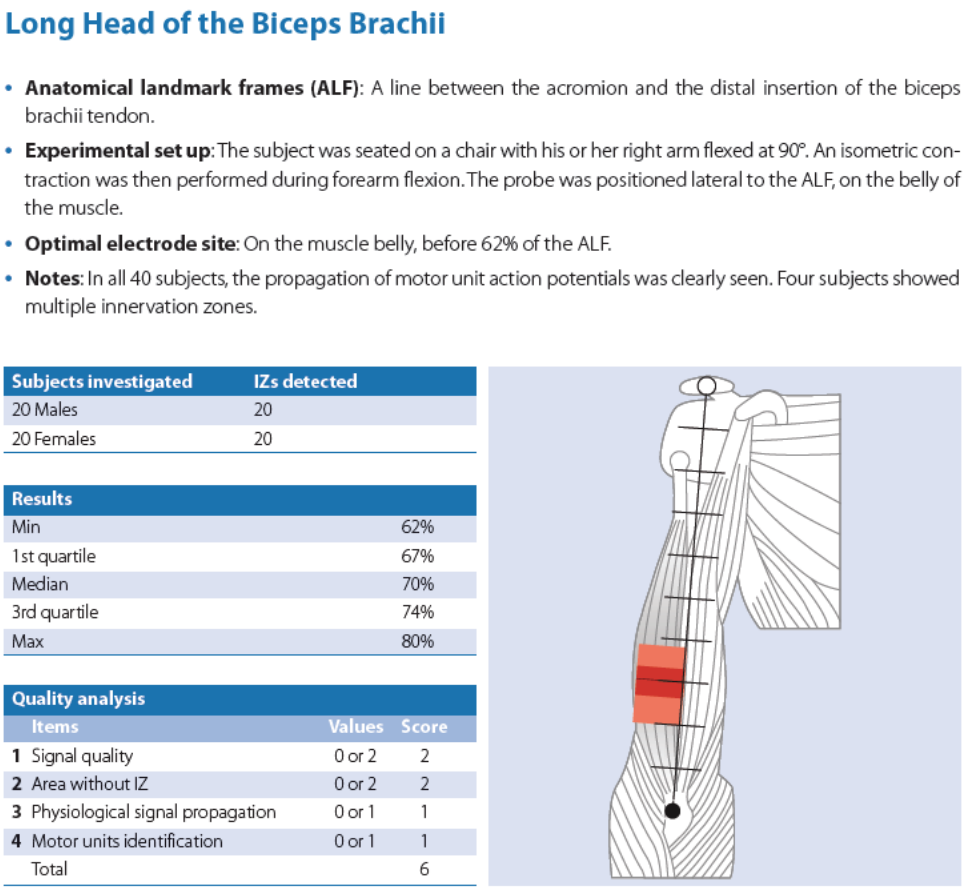
(a) (b)

Figure 4.1: Figure 4.1a shows the Raw-Power system's acquisition card, which connects to the PC via a USB interface. Figure 4.1b illustrates the cabling used to connect the card to the electrodes, highlighting the twisted pair for the differential signal and the single cable for the reference electrode.

Hardware Configuration and Electrode Placement

The system architecture utilizes acquisition boards, each capable of monitoring up to eight distinct muscles simultaneously [38].

- **Electrode Setup:** For each muscle, the sEMG signal was recorded using a differential configuration, employing a pair of active Ag/AgCl electrodes placed on the muscle belly. Crucial for reliable measurement, the electrodes were aligned with the muscle fibers and positioned distally from both the Innervation Zone (IZ) and the tendon, in accordance with SENIAM guidelines and the *Atlas of Muscle Innervation Zones* [6].
- **Reference Electrode:** A mandatory common reference electrode (ground) was applied to an electrically neutral site, specifically over an area with minimal electrical activity, such as a bone crest or a tendon (e.g., the anterior superior iliac spine). The positioning of the reference electrode is a mandatory configuration field in the Raw-Power application interface [38].



Long Head of the Biceps Brachii

- **Anatomical landmark frames (ALF)**: A line between the acromion and the distal insertion of the biceps brachii tendon.
- **Experimental set up**: The subject was seated on a chair with his or her right arm flexed at 90°. An isometric contraction was then performed during forearm flexion. The probe was positioned lateral to the ALF, on the belly of the muscle.
- **Optimal electrode site**: On the muscle belly, before 62% of the ALF.
- **Notes**: In all 40 subjects, the propagation of motor unit action potentials was clearly seen. Four subjects showed multiple innervation zones.

Subjects investigated	IZs detected
20 Males	20
20 Females	20

Results	
Min	62%
1st quartile	67%
Median	70%
3rd quartile	74%
Max	80%

Quality analysis			
	Items	Values	Score
1	Signal quality	0 or 2	2
2	Area without IZ	0 or 2	2
3	Physiological signal propagation	0 or 1	1
4	Motor units identification	0 or 1	1
	Total		6

Figure 4.2: Example of electrode placement provided by the *Atlas of Muscle Innervation Zones* [6]. The red zone indicates the area directly above the IZ where placing the differential electrodes is strongly advised against to minimize measurement artifacts. (Source: Adapted from [6])

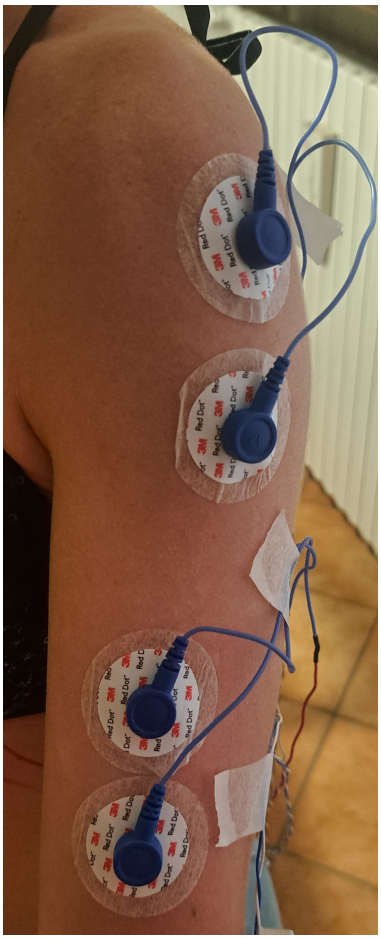


Figure 4.3: Example of electrode placement in a real application over the left arm.

Digital Acquisition Parameters and Data Output

The analog signals were digitized and stored using the following parameters:

- **Sampling Frequency (f_s):** The Raw-Power system allows for the selection of sampling frequencies ranging from $f_s = 2.7$ kHz (Mode 0, 1) down to $f_s = 500$ Hz (Mode 6, 7) [38]. The choice of frequency is critical to ensure adherence to the Nyquist criterion for the sEMG signal spectrum (which typically lies below 500 Hz), thus preventing aliasing artifacts.
- **Output Format:** Acquired data are stored in CSV format. The file contains the Timestamp (in microseconds), internal checks (Stream ID, Sequence), and 8 columns representing the Analog-to-Digital Converter (ADC) value (RAW signal) for the selected muscles [38].
- **Data Analysis:** The application provides integrated functionalities for offline data analysis, including signal filtering (e.g., 5^{th}-order Butterworth, low-cut: 20.0 Hz), smoothing (e.g., Savitzky-Golay), and the computation of sEMG features such as RMS, MNF, and MDF [38].

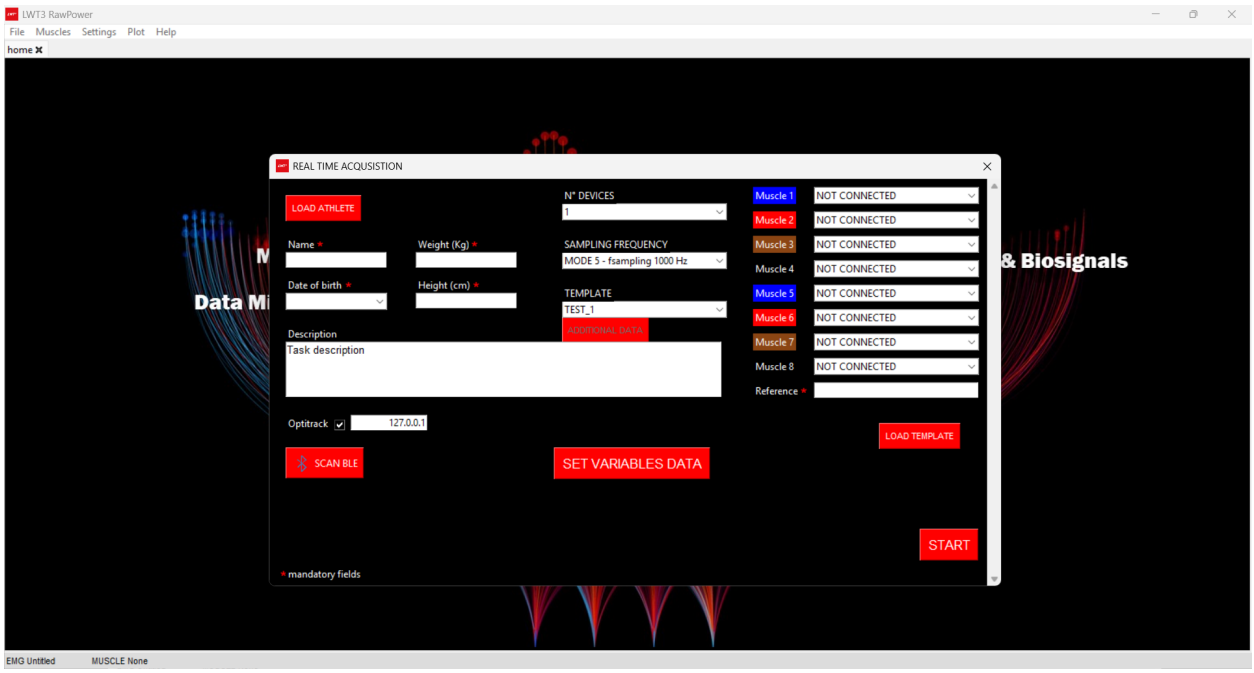


Figure 4.4: The Raw-Power system interface used for pre-test configuration, enabling subject parameter input, muscle selection, and sampling frequency setting. Configurations can be saved as templates (e.g., SHIRT, RUN) to ensure test reproducibility [38].

4.1.2. EMG Signal Analysis for Workload Assessment

To perform the sEMG data analysis, the *LWT3 Raw Power* software, provided alongside the acquisition boards [38], was utilized as a foundation for a dedicated MATLAB script developed specifically for this scope.

The primary objective is to process the raw sEMG signal into a filtered and comparable form to conduct analyses correlating the Root Mean Square (RMS) amplitude feature with MWL [39, 66]. The RMS is a key parameter for evaluating muscle electrical activity and is closely related to the control of mechanical impedance by the Central Nervous System (CNS) [39, 66].

The sequence of the main operations performed is as follows:

1. **Raw Signal Visualization** [38].
2. **Signal Filtering**: Application of a fifth order Butterworth band-pass filter to exclude unwanted frequency contributions [14, 38].
3. **RMS Calculation**: Computation of the RMS value, an amplitude feature used to quantify muscle activity [39].

Raw Data vs. Filtered Data

For the analysis, a generic muscle is considered by comparing the raw signal acquired by the acquisition board with the output of a preliminary filtering process [38].

This process involves applying a 5^{th}*-order Butterworth band-pass filter* [38]. The filter generally includes a low-cut frequency (high-pass filter, f_{HP}) typically set around 20 Hz and a high-cut frequency (low-pass filter, f_{LP}) usually around 500 Hz [14, 38].

- The high-pass filter ($f_{HP} = 20$ Hz) is applied to mitigate contributions from movement artifacts and baseline noise [14]. These artifacts possess frequency spectra that contaminate the low-frequency portion of the sEMG signal [14]. A compromise is necessary when setting this frequency to reduce noise while preserving the desired information from the sEMG signal, as increasing the frequency beyond an optimal range (e.g., 20 Hz) can distort the signal [14].
- The low-pass filter ($f_{LP} = 500$ Hz) is typically set where noise components surpass the amplitude of the sEMG signal, often recommended in the 400 Hz to 450 Hz range [14].

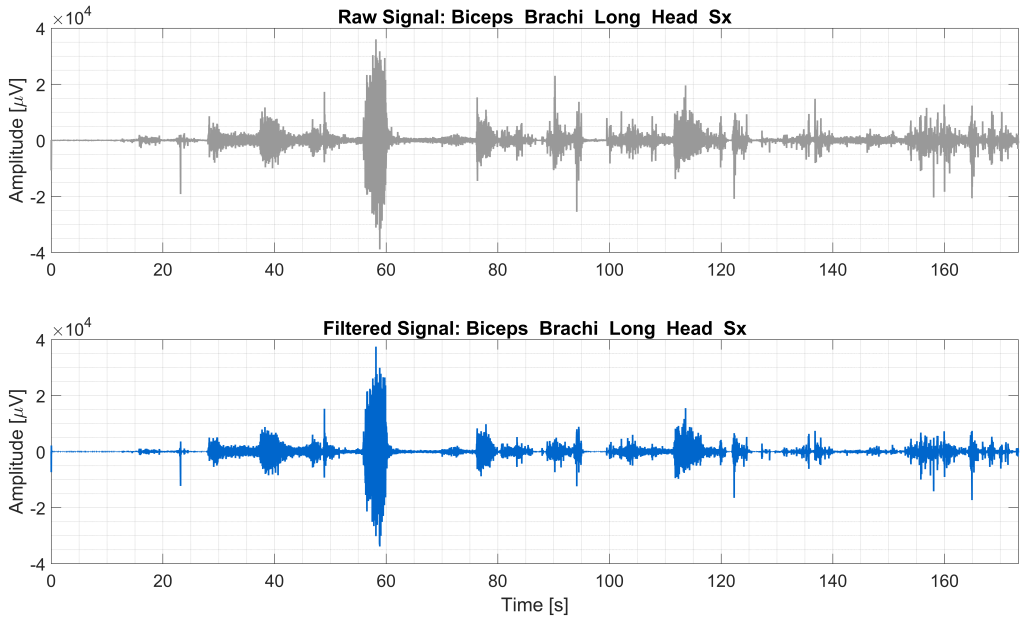


Figure 4.5: An example of the comparison between a raw sEMG signal (gray) and a filtered sEMG signal (blue). The filtering process reduces noise and retains the relevant frequency content. The 5^{th}-order Butterworth filter is a common choice for this operation [38].

RMS and MNF

Following filtering, it is possible to calculate the RMS value [38], which represents the amplitude feature used to assess muscle electrical activity, thereby providing an estimate of physical workload or effort [39, 66]. An increase in RMS often corresponds to an increase in

workload due to heightened muscle activation [39].

The Root Mean Square is defined mathematically as:

$$\mathrm{RMS} = \sqrt{\frac{1}{N}\sum_{i=1}^{N} x_i^2} \tag{4.1}$$

where N is the number of samples in the epoch and x_i is the instantaneous value of the signal [39].

The Mean Frequency (MNF) is a spectral feature providing information related to muscle fiber conduction velocity, used as a key index for myoelectric manifestations of muscle fatigue [14, 66].

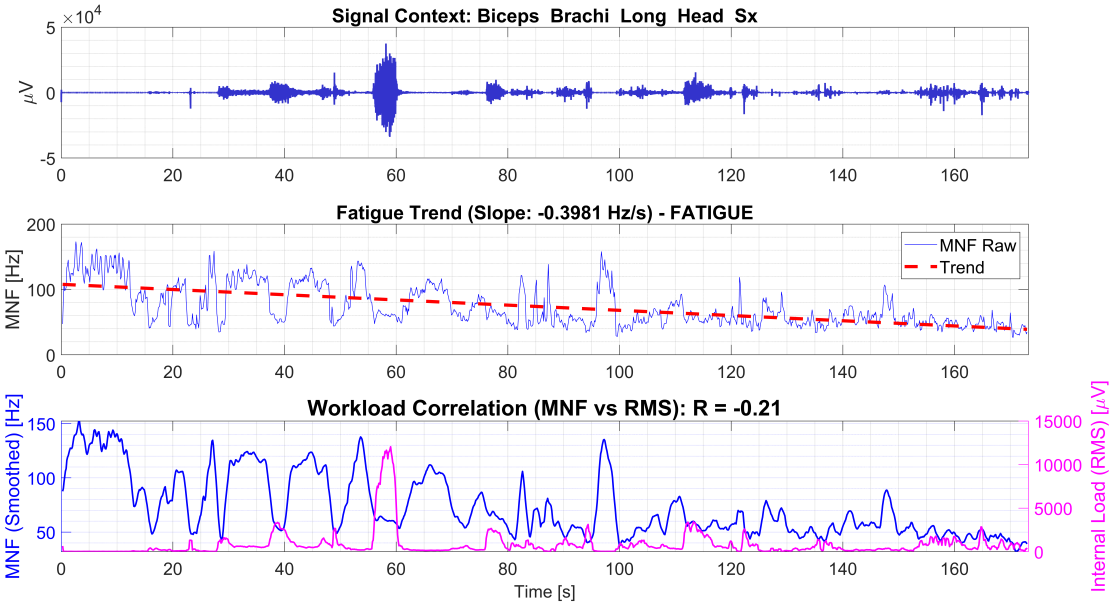


Figure 4.6: The image illustrates the comparison between the filtered signal, the calculated fatigue trend, and the workload correlation via the comparison between MNF and RMS. The trend in RMS amplitude is often used for qualitative assessment of workload, where an increase (peak) corresponds to higher workload or muscle activation in the current epoch [39].

Other sEMG Features

Utilizing the custom MATLAB script, it is possible to calculate additional features based on sEMG measurements. Below are graphs of these features, superimposed or compared with the filtered sEMG signal.

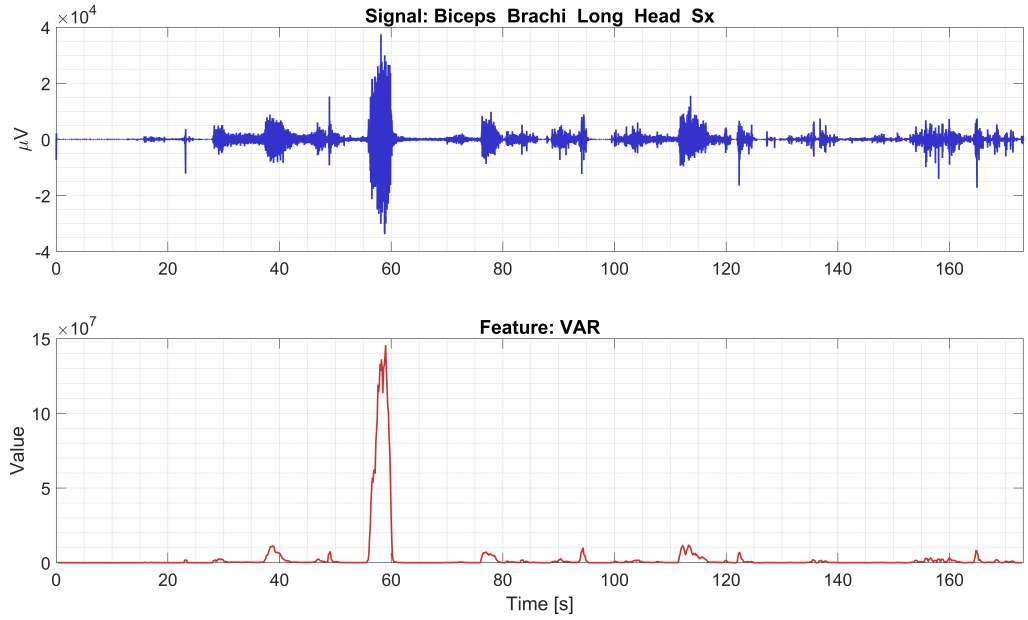


Figure 4.7: The image illustrates the comparison between the filtered signal and the calculated Variance (VAR) of the signal.

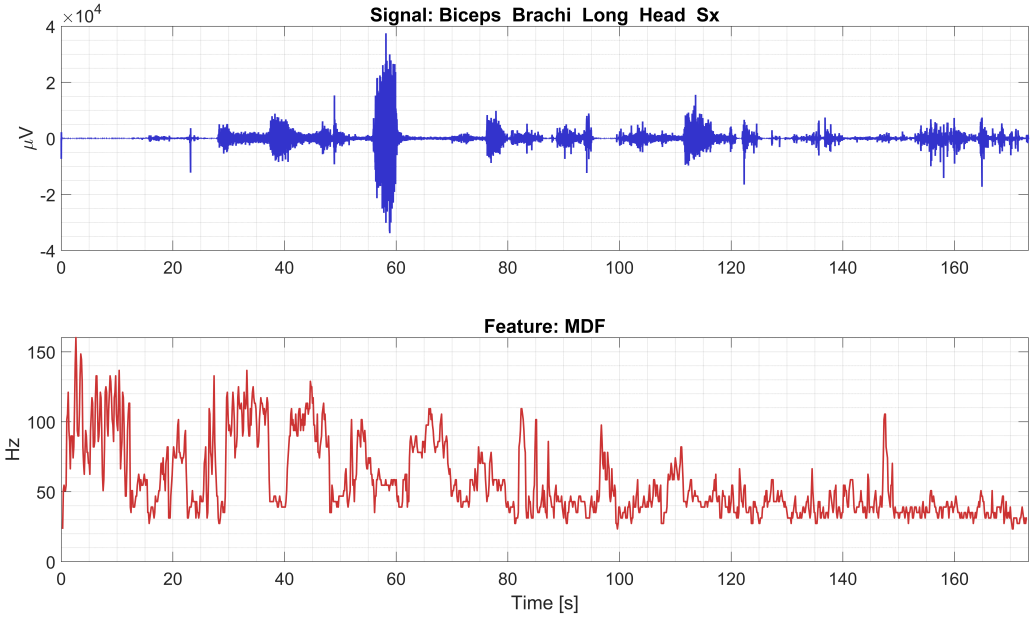


Figure 4.8: The image illustrates the comparison between the filtered signal and the calculated Median Spectral Frequency (MDF) of the signal.

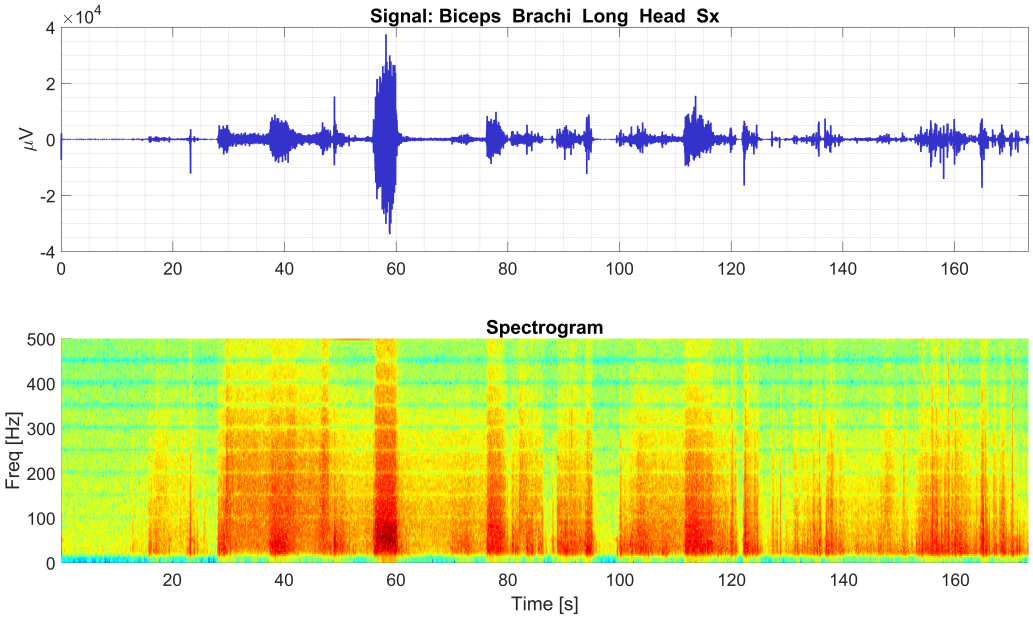


Figure 4.9: The software allows for the calculation of the signal spectrogram to evaluate the amplitude of the different signal components.

4.2. Eye tracking measures

4.2.1. Pupil Core Eye Tracking System

The eye tracking data for this study was collected using the *Pupil Core* system, a lightweight, head-mounted eye tracker developed by Pupil Labs GmbH [53]. The Pupil Core system is designed for mobile and desktop applications, providing non-intrusive gaze tracking suitable for various experimental paradigms.

Hardware Components

The primary hardware comprises a pair of wearable goggles housing two main sets of cameras:

1. **World Camera**: A high-resolution camera positioned centrally to capture the user's Field of View (FOV), providing the video context for the experiment.
2. **Eye Cameras**: Two miniature Infrared (IR) cameras, one per eye, focused directly on the pupil. These cameras record the pupil's position and diameter at a high frame rate, even in low-light conditions, allowing for robust pupil detection and gaze estimation.

The system connects to a host computer (e.g., laptop or mobile device) via USB-C for power and data transfer.

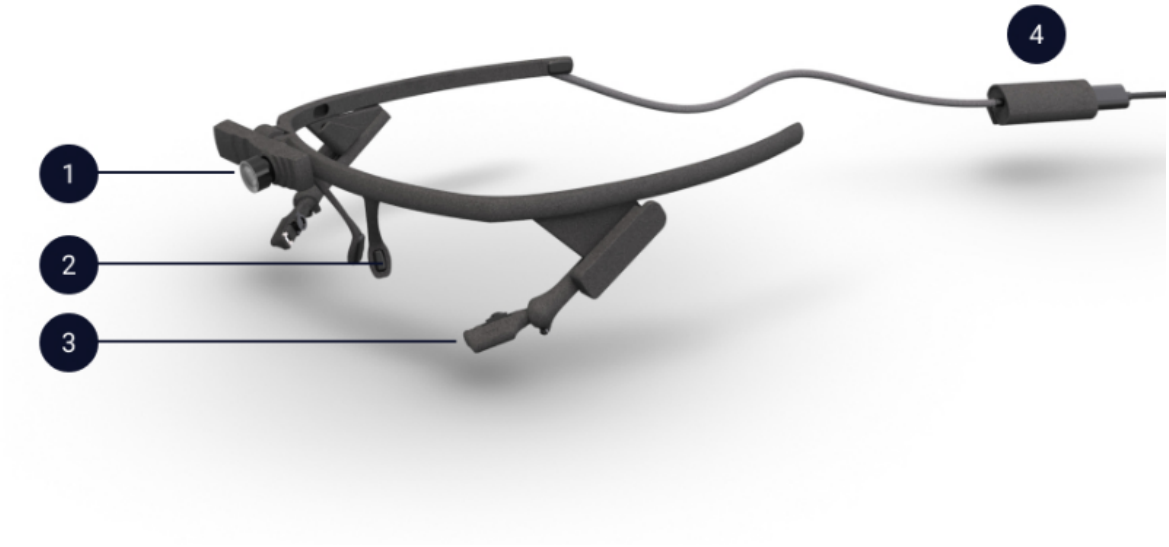


Figure 4.10: The Pupil Core eye tracking glasses. (1) World camera, (2) Nose support, (3) Eye camera(s), (4) USB-C connector clip. (Source: Adapted from [53])

Software Suite

Data acquisition and processing are managed by the official open-source software suite [53], which comprises three main applications:

1. **Pupil Capture**: This application is used for real-time recording and calibration. It streams synchronized video feeds from the world and eye cameras, applies the gaze detection algorithm, performs crucial calibration to map eye data onto the world video, and stores the raw data.

2. **Pupil Player**: This is the primary offline analysis tool. It allows users to review recordings, re-run or fine-tune tracking algorithms, visualize the gaze overlay on the world video, and export processed data (e.g., gaze coordinates, pupil size, events like blinks and saccades) into common formats like CSV or HDF5 for further statistical analysis.

3. **Pupil Service**: This background application manages the hardware connection and exposes a network Application Programming Interface (API). This enables remote control and data streaming for custom software integrations, facilitating synchronization with external data streams or experimental control software.

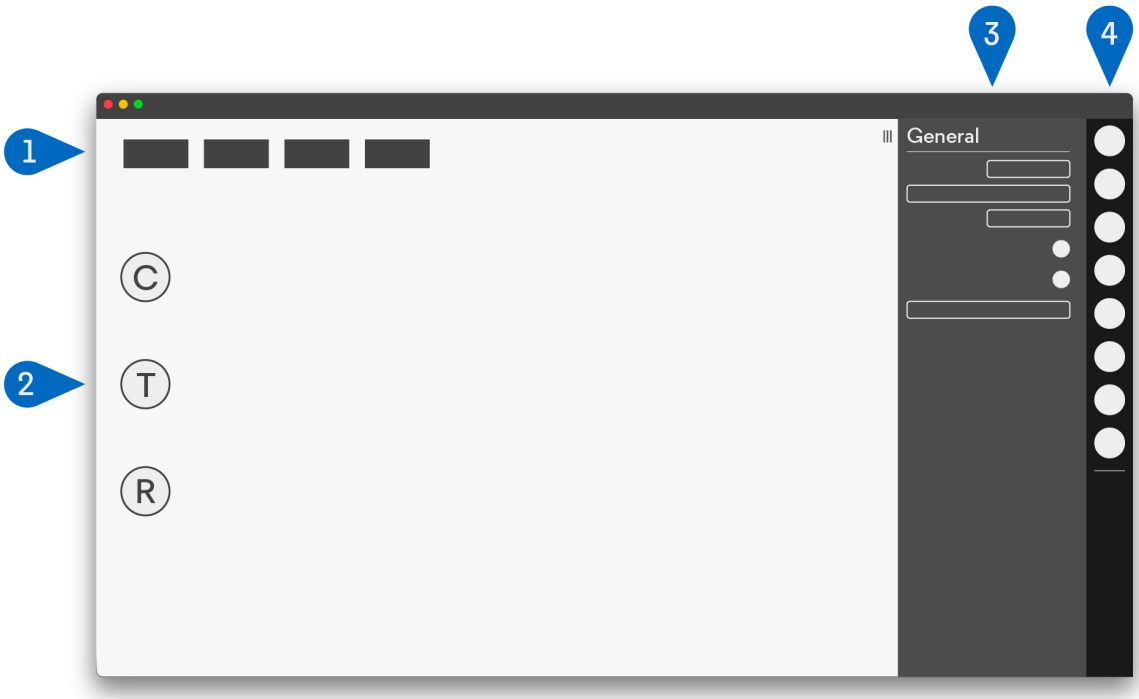


Figure 4.11: The user interface of the Pupil Capture software during a live recording session. (Source: Adapted from [53])
1. Graphs: Displays performance graphs. By default, CPU, FPS, and pupil algorithm detection confidence are shown. Graph settings can be controlled via the System Graphs plugin.
2. Hot keys: Contains clickable buttons for plugins.
3. Menu: Contains settings and contextual information for each plugin.
4. Sidebar: Contains clickable buttons for each plugin. System plugins are loaded at the top, and user-added plugins are added below a horizontal separator.

4.2.2. MARSH Eye Tracking Integration

To achieve seamless integration between the Pupil Labs Core eye tracking glasses and the instrumentation already present at the FRAME Lab, specific implementations of the MARSH protocol were developed (MARSH Documentation). These extensions coordinate all sensors utilized during the experimental tests. Specifically, messages such as `EYE_TRACKING_DATA` and `EYE_TRACKING_EVENT` were added to facilitate the logging of pilot gaze vectors and recognized gaze events (blink, fixation, saccade) [35].

Eye-Tracking Data Acquisition (`EYE_TRACKING_DATA`)

The MARSH system incorporates a mechanism for real-time pilot gaze monitoring by utilizing a dedicated `MARSH_TYPE_EYE_TRACKER` Node. This node interfaces with external eye-tracking hardware and corresponding proprietary software, such as that provided by Pupil

Labs GmbH, utilizing tailored scripts for data forwarding [35].

This data acquisition is standardized through the MARSH MAVLink dialect, specifically via two custom messages, `EYE_TRACKING_DATA` and `EYE_TRACKING_EVENT` [40]. The primary data carrier for continuous gaze information is the `EYE_TRACKING_DATA` message, designed to capture both the estimated 3D position of the eye relative to the sensor and the derived gaze vector.

Key fields within this message include:

- **Gaze Origin:** The X, Y, Z coordinates of the `gaze_origin` point, representing the calculated center of the eye in meters, which allows for precise spatial referencing of the pilot's head within the cockpit's defined coordinate system.
- **Gaze Direction Vector:** The normalized X, Y, Z vector of the `gaze_direction`, which is essential for determining the pilot's instantaneous line of sight towards instruments or the external visual scene.
- **Focal Points and Biometrics:** Additional fields provide context-specific information critical for human factors analysis, including the estimated `pupil_diameter` in millimeters and the normalized coordinates (0 to 1) of the gaze focal point on the video feed (`video_gaze`) and on specific reference surfaces (`surface_gaze`).

Table 4.1: MAVLink Message: EYE_TRACKING_DATA

Field Name	Properties		Description
	Type	Units	
TIMESTAMPS AND IDENTIFIERS			
time_usec	uint64_t	us	Timestamp (UNIX Epoch time or time since system boot).
sensor_id	uint8_t	-	Unique ID for the eye tracking sensor/device.
3D GAZE DATA (WORLD SPACE)			
gaze_origin_x	float	m	X-coordinate of the eye origin in 3D space.
gaze_origin_y	float	m	Y-coordinate of the eye origin in 3D space.
gaze_origin_z	float	m	Z-coordinate of the eye origin in 3D space.

Continued on next page

Table 4.1 – *Continued from previous page*

Field Name	Properties		Description
	Type	Units	
gaze_direction_x	float	-	X-component of the gaze direction unit vector.
gaze_direction_y	float	-	Y-component of the gaze direction unit vector.
gaze_direction_z	float	-	Z-component of the gaze direction unit vector.
2D GAZE DATA (SCREEN/SURFACE SPACE)			
video_gaze_x	float	-	X-position in video frame (normalized 0.0 to 1.0).
video_gaze_y	float	-	Y-position in video frame (normalized 0.0 to 1.0).
surface_id	uint8_t	-	ID of the specific surface being looked at.
surface_gaze_x	float	-	X-position on the surface (normalized 0.0 to 1.0).
surface_gaze_y	float	-	Y-position on the surface (normalized 0.0 to 1.0).
EYE METRICS			
pupil_diameter	float	mm	Diameter of the pupil.

Complementing the continuous data stream is the `EYE_TRACKING_EVENT` message. This message is designed to report discrete temporal events recognized through analysis of the gaze data, categorized by the `EYE_TRACKING_EVENT_TYPE` enumeration:

- `EYE_TRACKING_EVENT_TYPE_BLINK` (Partial or full eye closure): type = 0.
- `EYE_TRACKING_EVENT_TYPE_FIXATION` (A period of stable gaze on a location, quantified by a dispersion magnitude): type = 1.
- `EYE_TRACKING_EVENT_TYPE_SACCADE` (A rapid, small eye movement, quantified by the total angular movement magnitude): type = 2.

Table 4.2: MAVLink Message: EYE_TRACKING_EVENT

Field Name	Properties		Description
	Type	Units	
TEMPORAL AND IDENTIFICATION			
time_usec	uint64_t	us	Start timestamp (UNIX Epoch or time since boot). Matches EYE_TRACKING_DATA.
sensor_id	uint8_t	-	Unique sensor ID for the device/person tracked (0 if unknown).
duration	uint64_t	us	Total duration of the event (set to 0 if not applicable).
EVENT CHARACTERISTICS			
type	uint8_t	-	Type of event (e.g., Blink, Fixation, Saccade) defined in EYE_TRACKING_EVENT_TYPE.
confidence	float	-	Estimator confidence value between 0.0 and 1.0.
magnitude	float	deg	Magnitude dependent on type (e.g., fixation dispersion or saccade movement angle).

The inclusion of these specialized MAVLink messages ensures that high-fidelity human factors data is logged consistently alongside flight dynamics and control system states, facilitating unified data post-processing via the MATLAB analysis workflow.

4.2.3. Eye Tracking Data Analysis

Post-processing of the eye-tracking data was performed using a custom MATLAB® script designed to import, filter, and visualize the telemetry logged via the MARSH protocol. The analysis utilizes the `mavlinktlog` function to parse the binary log files (`.tlog`) using the custom dialect definitions described in subsection 4.2.2. The workflow is divided into three primary components: pupil diameter processing, blink analysis, and fixation analysis.

Pupil Diameter Analysis

The raw pupil diameter data is extracted from the `EYE_TRACKING_DATA` message. Since raw eye-tracking data inevitably contains noise and signal loss due to blinks or momentary occlusion, a pre-processing step is applied. Timestamps are normalized to the start of the recording ($t = 0$), and invalid data points (where pupil diameter ≤ 0) are filtered out.

To maintain signal continuity for statistical analysis, missing values are reconstructed using Piecewise Cubic Hermite Interpolating Polynomial (PCHIP) interpolation. This method preserves the shape of the data and prevents overshooting artifacts common with standard cubic splines. The result is a continuous timeline of pupillary changes, as shown in Figure 4.12, allowing for the calculation of the mean pupil diameter—a key metric often correlated with cognitive workload.

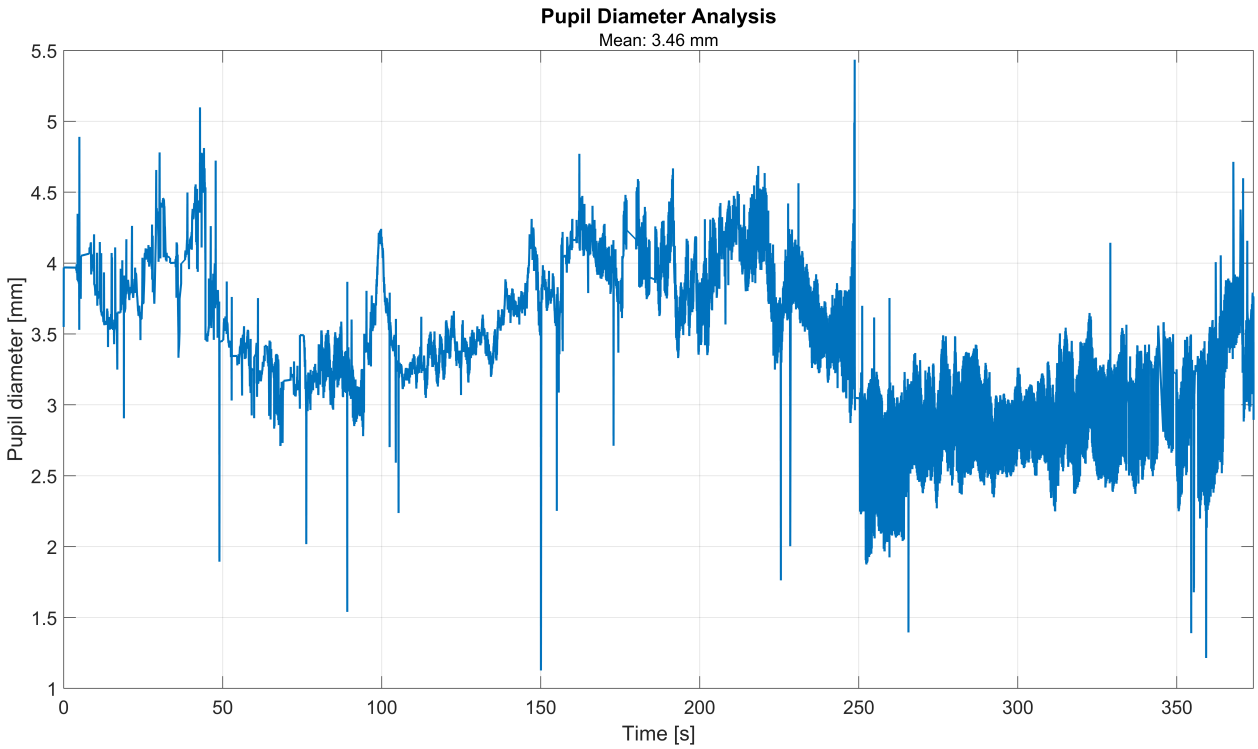


Figure 4.12: Pupil diameter analysis over time. The plot shows the interpolated pupil diameter signal (blue) after removing artifacts, allowing for the assessment of physiological arousal trends.

Blink Analysis

Blink behavior is analyzed using the discrete events logged in the `EYE_TRACKING_EVENT` message (Type 0). The script extracts the timestamp and duration of every blink event.

Beyond individual blink duration, the analysis calculates the *Blink Rate* (Blinks Per Minute - BPM) to identify trends in pilot fatigue or visual attention. The blink rate is computed using a sliding window algorithm with a window size of 60 seconds. This approach provides

a dynamic measure of blink frequency over the course of the flight session rather than a single static average. Figure 4.13 illustrates both the discrete blink events (top) and the continuous blink rate trend (bottom).

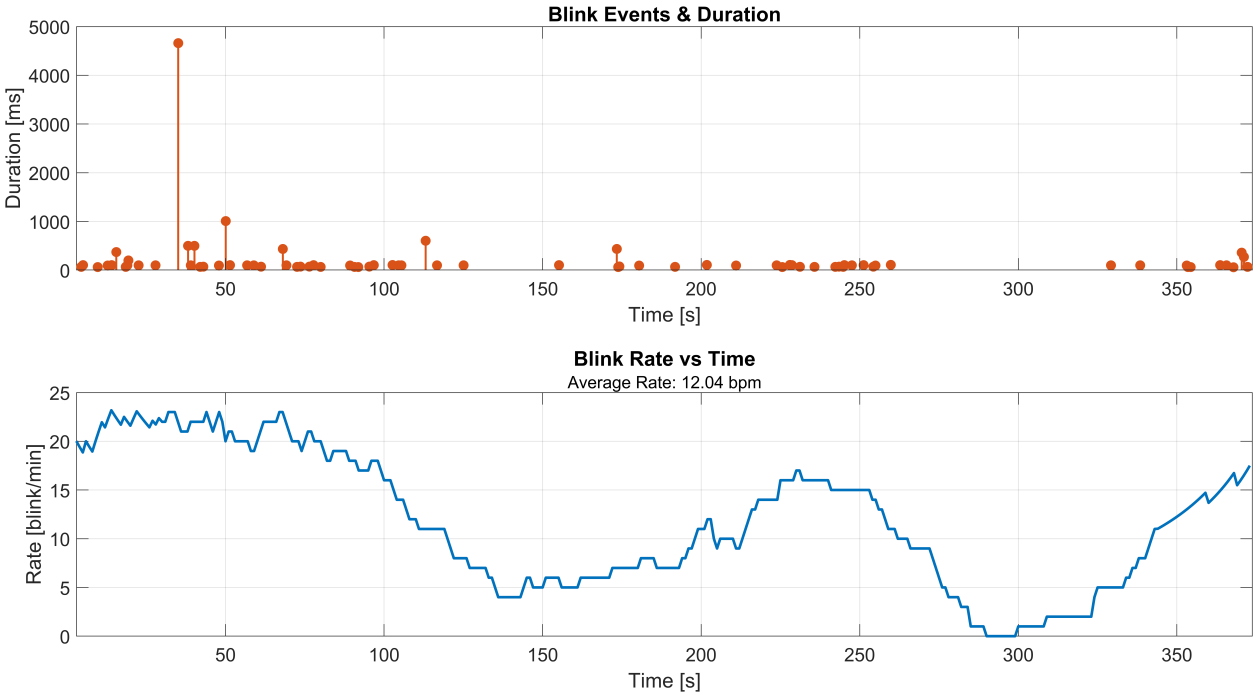


Figure 4.13: Blink analysis. Top: Discrete blink events and their durations (stem plot). Bottom: The calculated Blink Rate (Blinks Per Minute) over time using a 60-second sliding window, highlighting variations in blink frequency.

Fixation Analysis

Visual fixations, defined as periods where the gaze is relatively stable on a specific target, are extracted from the `EYE_TRACKING_EVENT` message (Type 1). The analysis focuses on the temporal distribution and duration of these fixations.

As visualized in Figure 4.14, the duration of each fixation is plotted against time. This data is critical for understanding the pilot's scan pattern and information processing speed; longer fixations may indicate difficulty in interpreting instruments, while rapid, short fixations may suggest an active visual search or monitoring task.

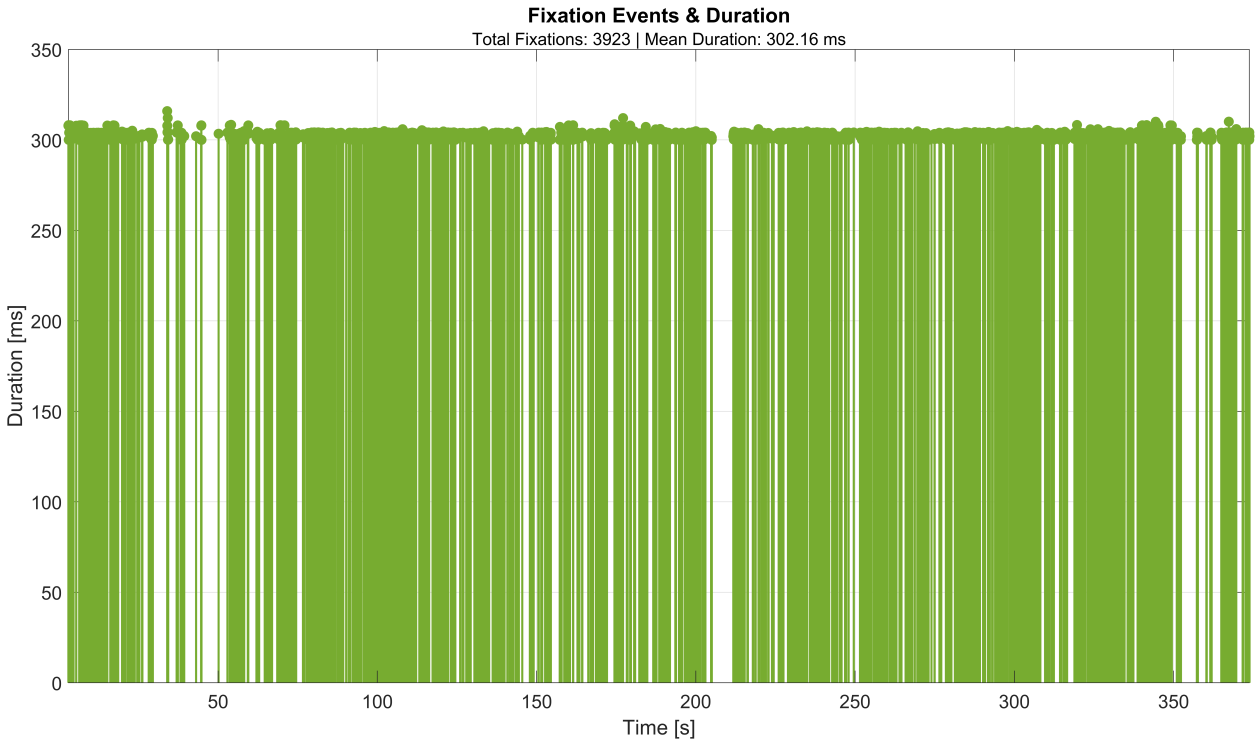


Figure 4.14: Fixation analysis showing the occurrence and duration of fixation events throughout the experimental session. The density and height of the stems indicate the pilot's visual attention stability.

4.3. ECG Measurement System Architecture

The Electrocardiogram (ECG) measurement system utilized is a wired, single-lead biopotential acquisition device designed for triggered monitoring and signal classification. The system architecture is modular, consisting of three primary stages: the Analog Front-End (AFE) for signal extraction and conditioning, a Microcontroller Unit (MCU) based on the STM32 Nucleo platform for analog-to-digital conversion and processing, and a wired communication/storage interface. Acquisition synchronization is handled via a hardwired trigger signal from an external LabJack T7 data acquisition device [3, 9, 62].

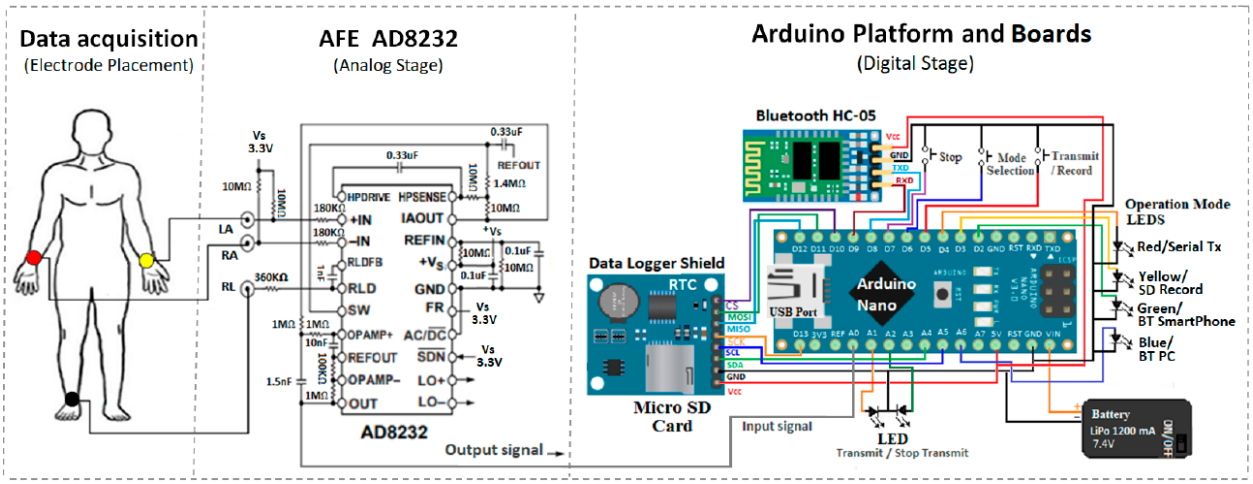


Figure 4.15: Sections of the ECG prototype showing the signal path from electrode placement to the analog front-end and digital processing stages. The system uses a wired configuration with an external trigger (Source: Adapted from [9]).

4.3.1. Analog Front-End: AD8232 Sensor

The core component of the measurement system is the AD8232 Single-Lead Heart Rate Monitor Front End [2]. This integrated circuit is designed to extract small biopotential signals in the presence of noisy conditions, such as those created by motion or remote electrode placement.

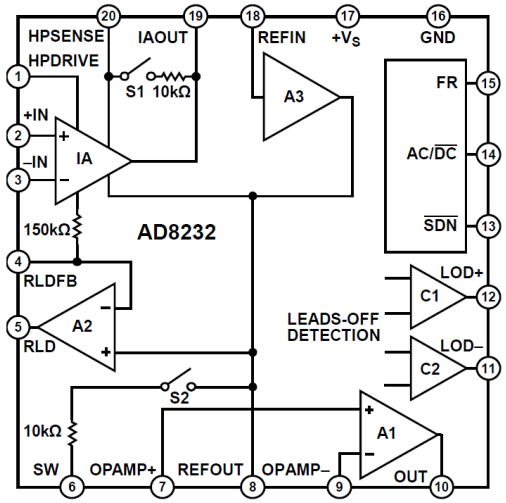


Figure 4.16: Functional block diagram of the AD8232 sensor, highlighting the integrated instrumentation amplifier and filter architecture [2]. (Source: Adapted from [2])

Signal Conditioning

The AD8232 architecture employs a specialized Instrumentation Amplifier (IA) with a typical Common-Mode Rejection Ratio (CMRR) of 80 dB (DC to 60 Hz), which is crucial for

rejecting line noise [2]. The amplifier utilizes a two-pole high-pass filter to eliminate motion artifacts and the electrode half-cell potential. This filter is tightly coupled with the instrumentation architecture, allowing for a high signal gain of 100 V/V in a single stage while blocking DC offsets [2].

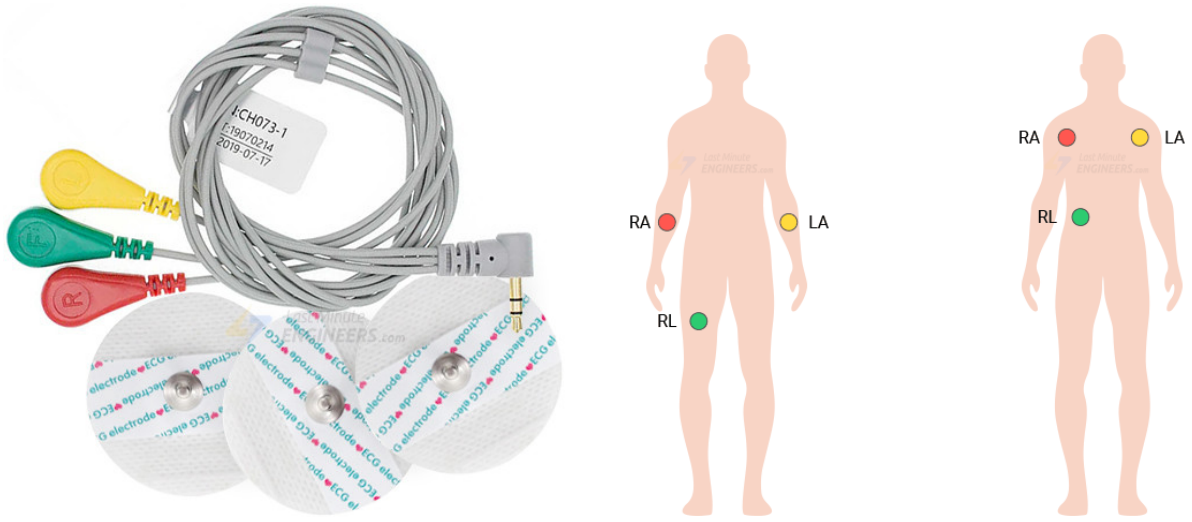
In the specific implementations discussed, the system is configured to achieve a total gain of approximately 1100x with a bandwidth ranging from 0.5 Hz to 40 Hz [9]. This bandwidth is optimized to capture the PQRST morphology while filtering out high-frequency noise and muscle artifacts. The system also utilizes an uncommitted operational amplifier within the AD8232 to create a three-pole low-pass filter for additional noise removal [2].

Right Leg Drive (RLD)

To further improve common-mode rejection, the system implements a Right Leg Drive (RLD) circuit. The AD8232 includes an integrated RLD amplifier that inverts the common-mode signal present at the instrumentation amplifier inputs and drives it back into the patient [2]. This configuration maintains the voltage between the patient and the AFE at a near-constant level, significantly reducing interference from power lines [3].

Electrodes and Interface

The system employs a 3-lead electrode configuration. Disposable dry or gel electrodes are connected to the AD8232 via a 3.5 mm jack or direct pin headers [3]. The standard placement described involves electrodes on the Right Arm (RA), Left Arm (LA), and Right Leg (RL) to form Lead I, with the RL acting as the driven reference electrode [9]. The AD8232 also features leads-off detection circuitry to monitor electrode contact quality [2].



(a) (b)

Figure 4.17: Figure 4.17a shows the cables and the electrodes used by the AD8232 EMG Module. Figure 4.17b shows the two different electrode arrangements over the body.

4.3.2. Data Acquisition, Processing Unit and Communication

The conditioned analog signal from the AD8232 is fed into an STM32 Nucleo-64 board for digitization and processing.

Microcontroller Implementation

The processing platform is based on the STM32 Nucleo-64 board (MB1136), which features a high-performance 32-bit Arm Cortex-M microcontroller (e.g., STM32F103RB, STM32L476RG) [62]. This platform is selected over Arduino-based alternatives for its superior processing capabilities and flexible I/O options necessary for wired, triggered acquisition.

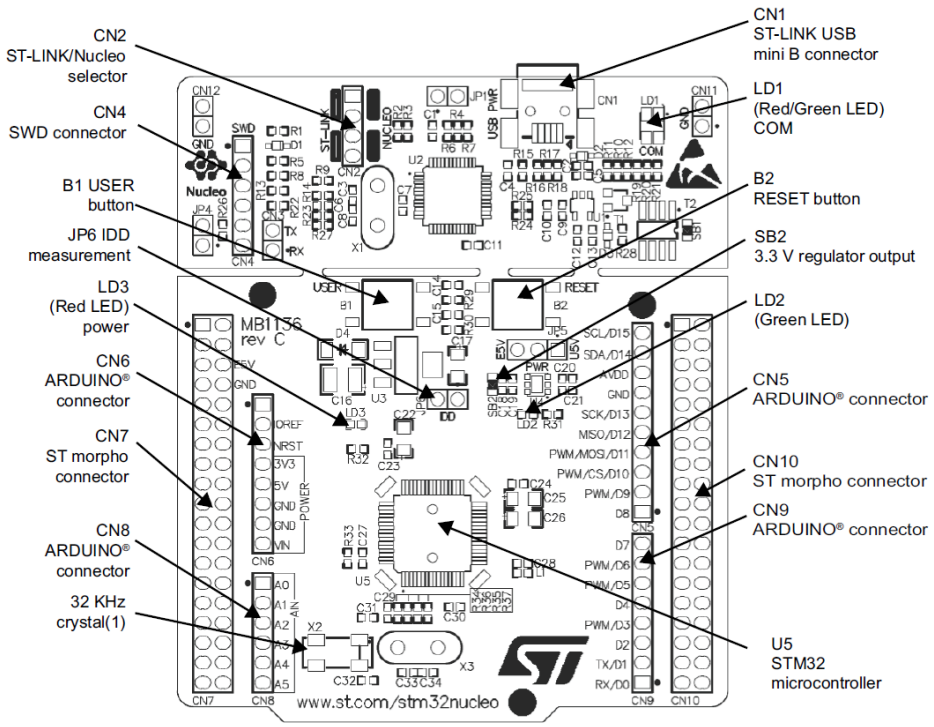


Figure 4.18: Top layout of the STM32 Nucleo-64 board, showing the Arduino-compatible headers and ST morpho connectors used for interfacing with the AD8232 sensor and the LabJack trigger line [62]. (Source: Adapted from [62])

- **ADC Configuration:** The STM32 MCU utilizes its onboard 12-bit Analog-to-Digital Converter (ADC) to sample the output signal from the AD8232. This provides higher resolution (4096 levels) compared to standard 10-bit ADCs, allowing for more precise capture of the ECG waveform [62].
- **Triggered Acquisition:** The system is configured to start data acquisition upon receiving a wired digital trigger signal from an external LabJack T7 device. The trigger line is connected to a digital input pin on the STM32 Nucleo (accessible via the ST Morpho headers), which is configured to generate an interrupt on the rising or

falling edge to initiate the sampling sequence.

- **Connectivity Headers:** The Nucleo board includes both ARDUINO® Uno V3 connectivity and ST morpho extension pin headers [62]. This allows the AD8232 module to be easily connected via standard jumper wires or a dedicated shield, while simultaneously accommodating the trigger connection from the LabJack T7.

Communication and Storage

For data handling, the system relies exclusively on wired interfaces and local storage, avoiding wireless transmission to ensure signal integrity and synchronization reliability.

- **Data Logging:** The system is expanded with a micro SD card module connected via the SPI interface on the Arduino or Morpho headers of the STM32 Nucleo. This enables long-term offline recording of ECG data directly on the device [9].
- **Wired Interface:** All control signals, including the acquisition trigger from the LabJack T7, are hardwired. Data transfer for analysis is performed post-acquisition via the SD card or through the USB interface of the Nucleo board (utilizing the ST-LINK/V2-1 virtual COM port) [62].

Power Supply

The STM32 Nucleo board offers flexible power supply options suitable for this wired setup [62]:

- **USB VBUS:** Power is typically supplied directly via the USB connector (5 V) connected to the host PC or dedicated power bank.
- **External Sources (VIN/E5V):** Alternatively, for isolated operation, the board can be powered by external sources (7 V – 12 V VIN or regulated 5 V E5V), with onboard regulators providing the stable 3.3 V required by the MCU and the AD8232 sensor.

4.3.3. Data Analysis

Data processing and analysis were performed using a custom MATLAB algorithm developed specifically for this application. As previously discussed, signal conditioning and primary filtering are handled directly by the hardware integration of the AD8232 module; consequently, the software analysis focuses exclusively on the post-acquisition processing of the raw data.

The system operates at a sampling frequency of $f_s = 250$ Hz. The analysis workflow is structured into four distinct stages, described as follows:

1. **Signal Visualization and Windowing:** The initial phase involves the inspection of the complete raw signal in the time domain. A specific time window is defined by the

user (specifying initial and final timestamps, t_{start} and t_{end}) to isolate the segment of interest. To ensure accurate amplitude analysis, a DC offset removal is applied to the windowed signal by subtracting its mean value.

2. **Peak Detection:** The algorithm identifies the R-peaks within the QRS complex, which are essential for cardiac timing analysis. Peak detection is performed using adaptive thresholds: a minimum peak height (set at 60% of the maximum signal amplitude within the window) and a minimum peak distance (set to 0.2 s) are enforced to differentiate true R-peaks from T-waves or motion artifacts.

3. **BPM and Heart Rate Estimation:** Based on the detected peaks, the system calculates the RR intervals (the time difference between consecutive R-peaks). These intervals are used to compute the instantaneous HR and Beats Per Minute (BPM), as well as the average BPM over the entire selected time window.

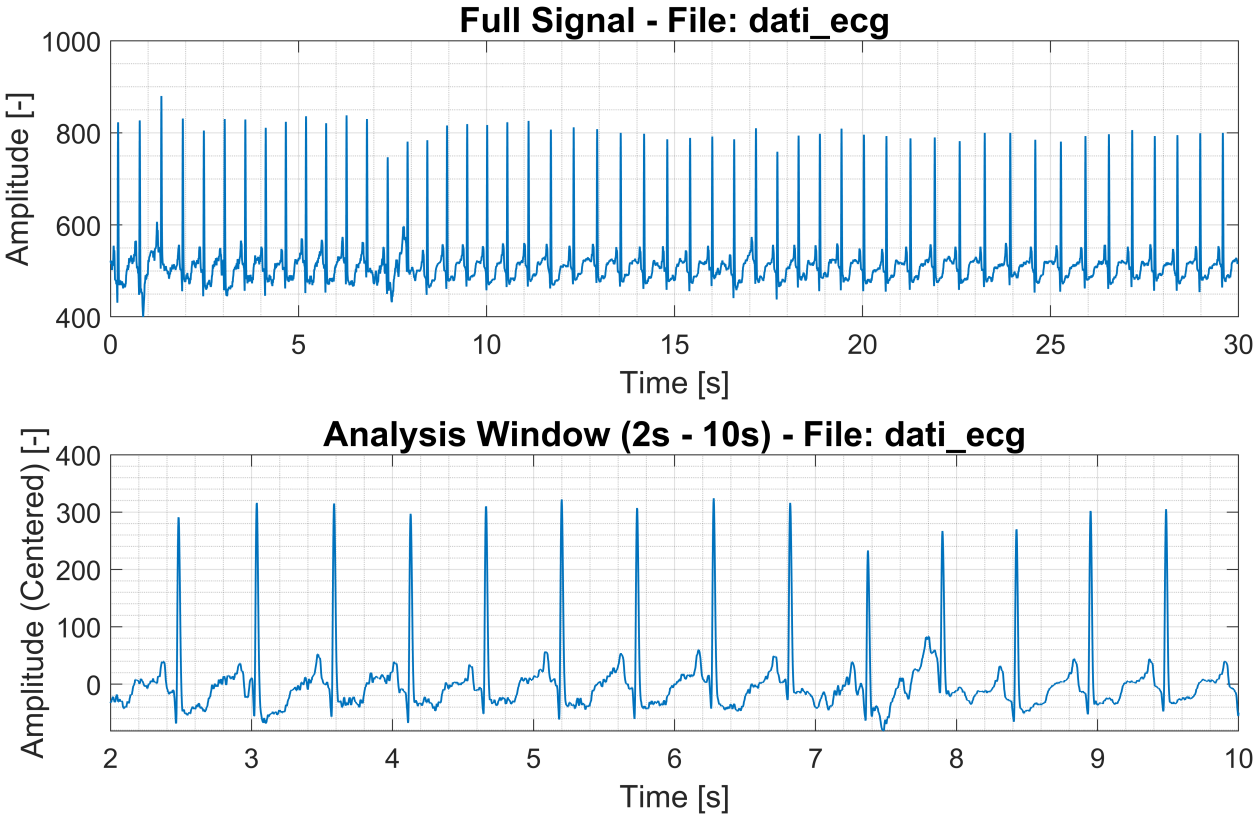


Figure 4.19: Raw signal is represented on the top of the image. On the bottom is presented the same signal centered on the time window selected.

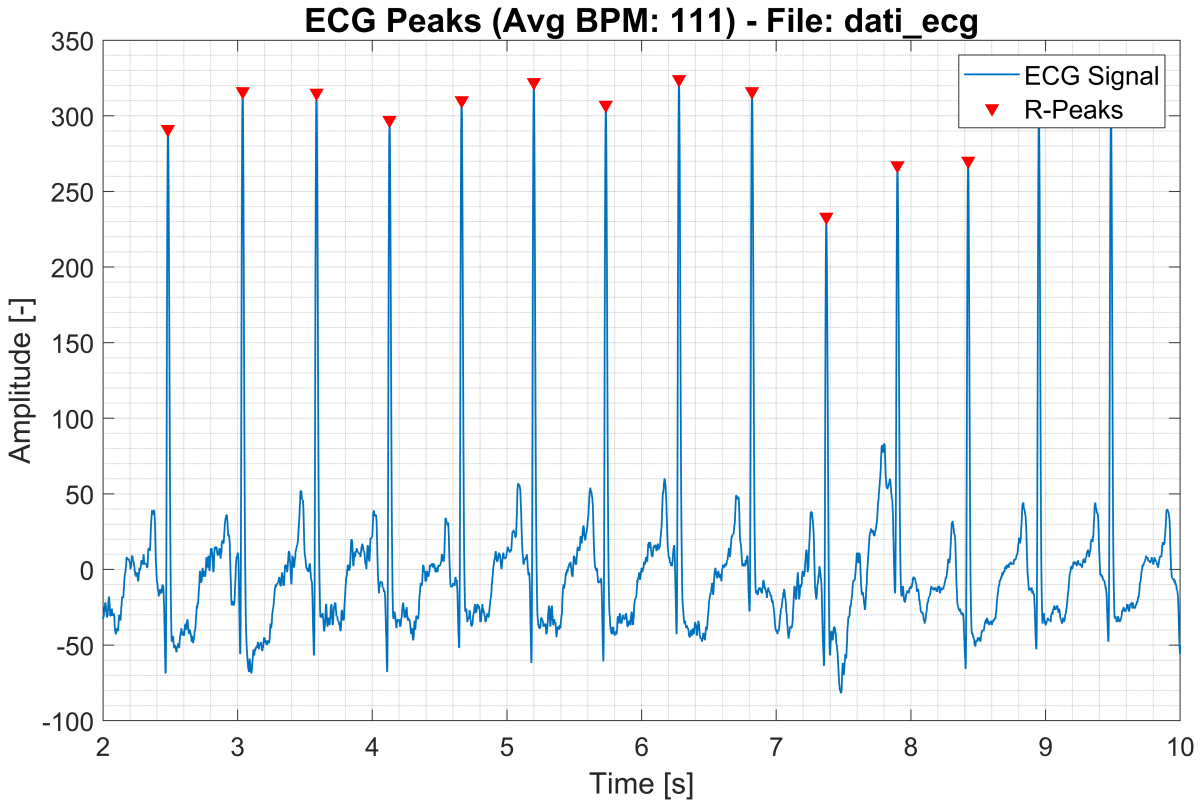


Figure 4.20: Visualization of R-peaks on the selected time window.

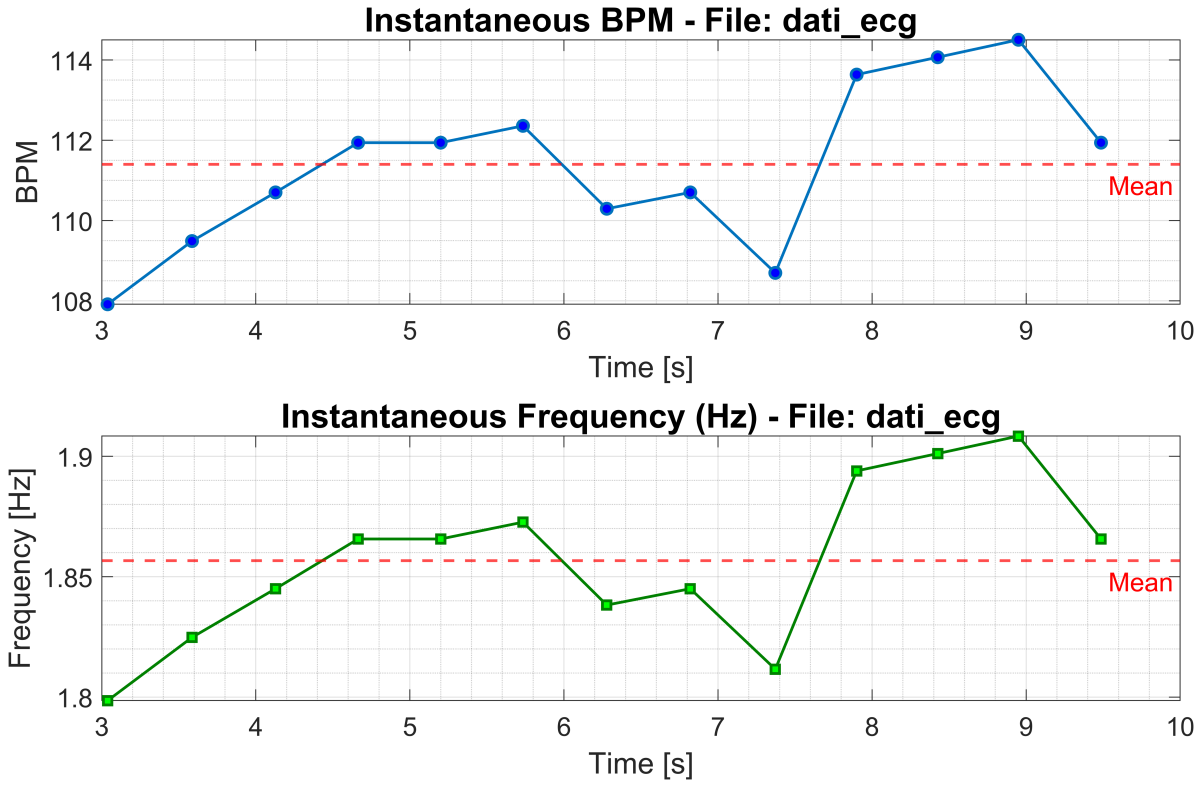


Figure 4.21: The last image shows the estimation of instantaneous and mean BPM (top) and HR (bottom) on the selected time window.

4.4. Body Pose Tracking

4.4.1. Hardware: Intel RealSense Depth Camera D455f

The hardware foundation for robust body pose tracking is built upon advanced depth-sensing technology, exemplified by the *Intel RealSense Depth Camera D455f* (SKU: `0x0B5C`). This device is specifically designed for high-precision spatial awareness, which is critical for reliably estimating human pose in three dimensions [25].



Figure 4.22: The Intel RealSense D455f camera used for the experiments and tests on the RPC test rig.

Depth and Vision Processing Core

The D455f is a stereo vision depth camera system incorporating the dedicated RealSense Vision Processor D4 [25]. This processor is responsible for computing depth information by correlating corresponding points captured by the left and right imagers [25]. The system utilizes a wide stereo imager configuration with a 95 mm baseline [25], providing enhanced depth accuracy and a typical range of 0.4 m to over 6 m [25]. The key imaging specifications are:

- **Depth Resolution:** Up to 1280 × 720 stereo depth at 30 FPS.
- **Imager Type:** Dual Global Shutter sensors (Table 3-14), crucial for minimizing motion blur in dynamic pose tracking scenarios.
- **Depth Field of View (FOV):** Diagonal FOV over 90°, ensuring a wide detection area (Table 3-49).

Inertial Measurement Unit (IMU) for 6 DOF Data

A critical feature for pose estimation is the inclusion of an integrated *Inertial Measurement Unit (IMU)*, which provides 6 Degrees of Freedom (6 DOF) data [25]. The IMU supplies highly accurate acceleration and gyroscope readings, which are essential for combining visual depth data with motion tracking. This sensor fusion is vital for smooth and stable pose tracking, particularly when the subject's movement is fast or when visual features are temporarily obscured.

- **Acceleration Range:** ±4 g.
- **Gyroscope Range:** ±1000 deg/s.
- **Sample Rate:** Accelerometer at 100 or 200 Hz; Gyroscope at 200 or 400 Hz (Table 4-24).

Infrared Enhancement for Ambient Light Immunity

The D455f variant includes an IR-pass filter [25] applied to the cover glass. This filter transmits near-infrared light (where the camera's IR projector operates) and absorbs visible light [25]. The advantages of the IR-pass filter for high-quality pose tracking are twofold [25]:

1. **Mitigation of Specular Reflections:** Reduces image saturation caused by visible ambient light reflections.
2. **False Depth Mitigation:** The camera focuses only on the scene's texture produced by its active IR projector, mitigating false depth readings often caused by repetitive visible light patterns (e.g., in structured indoor environments).

The active illumination is provided by a Wide Infrared Projector with an optical power of 360 mW average, meeting Class 1 laser safety standards [25]. The combination of the IR filter and the active projector ensures robust performance even in bright indoor or outdoor environments, significantly improving the stability of the depth stream for continuous pose tracking.

4.4.2. Software Implementation and Pose Detection

The raw data streams generated by the D455f hardware are managed and processed by a multi-layered software stack, enabling the extraction of high-level features such as body pose.

The Core SDK and Data Acquisition

The fundamental interaction with the D455f camera is handled by the cross-platform *RealSense Software Development Kit 2.0* (`librealsense`) [24]. This SDK facilitates three crit-

ical roles in the pose tracking workflow:

1. **Stream Management:** It allows the host application to establish and manage synchronized, high-bandwidth streams (Color/RGB and Depth) over USB 3.1 Gen 1. The script leverages this to request specific formats and frame rates that optimize for the required processing pipeline.
2. **Calibration Parameter Access:** The SDK provides programmatic access to the intrinsic and extrinsic calibration matrices stored in the camera's non-volatile memory (EEPROM [25]). These precise, factory-calibrated parameters are non-negotiable for accurate 3D projection.
3. **Frame Alignment Utilities:** The SDK's depth module employs a computational tool (`rs.align`) to transform the coordinate space of the depth frame onto the visual (color) frame. This mathematical operation corrects for the physical offset (baseline) and angular rotation between the two sensors, ensuring that the detected 2D keypoint location directly maps to the correct depth pixel.

Application Script: `pose.py` Detailed Workflow

The Python application layer, exemplified by the `realsense-pose-detector` project [36], and typically integrated with external computer vision libraries (e.g., MediaPipe), formalizes the 3D pose estimation process into a tight loop of capture, alignment, and mapping.

Pipeline Configuration and Alignment Setup

The script begins by initializing the communication pipeline and setting up the precise configuration to utilize the hardware effectively. The simultaneous streaming of 1280×720 RGB and Z16 depth streams at 30 FPS is selected to balance spatial detail with frame rate, minimizing processing latency.

```
pipe = rs.pipeline()
config = rs.config()
config.enable_stream(rs.stream.depth, 1280, 720, rs.format.z16, 30)
config.enable_stream(rs.stream.color, 1280, 720, rs.format.bgr8, 30)
profile = pipe.start(config)

# Initialize alignment to map depth data onto the color coordinate system
align = rs.align(rs.stream.color)
```

Frame Acquisition, Alignment, and Scale Conversion

In each iteration, the script ensures a synchronized frame set is captured, performs the alignment, and retrieves the camera-specific depth scale for metrology.

1. **Synchronization:** `pipe.wait_for_frames()` captures a multi-frame buffer, ensuring the Depth and Color frames are hardware-matched temporally, leveraging the D455f's global shutter for motion consistency.
2. **Alignment:** `align.process(frames)` mathematically transforms the depth map to match the perspective of the color sensor.
3. **Depth Scale and Conversion:** The depth scale (e.g., 0.001 m per unit) is fetched from the depth sensor's profile. This value is essential for translating the raw 16-bit depth values (Z16) into real-world metric distances.

3D Coordinate Projection and Output

The final stage combines the pose detection results from the RGB image with the metric depth data to yield 3D spatial coordinates.

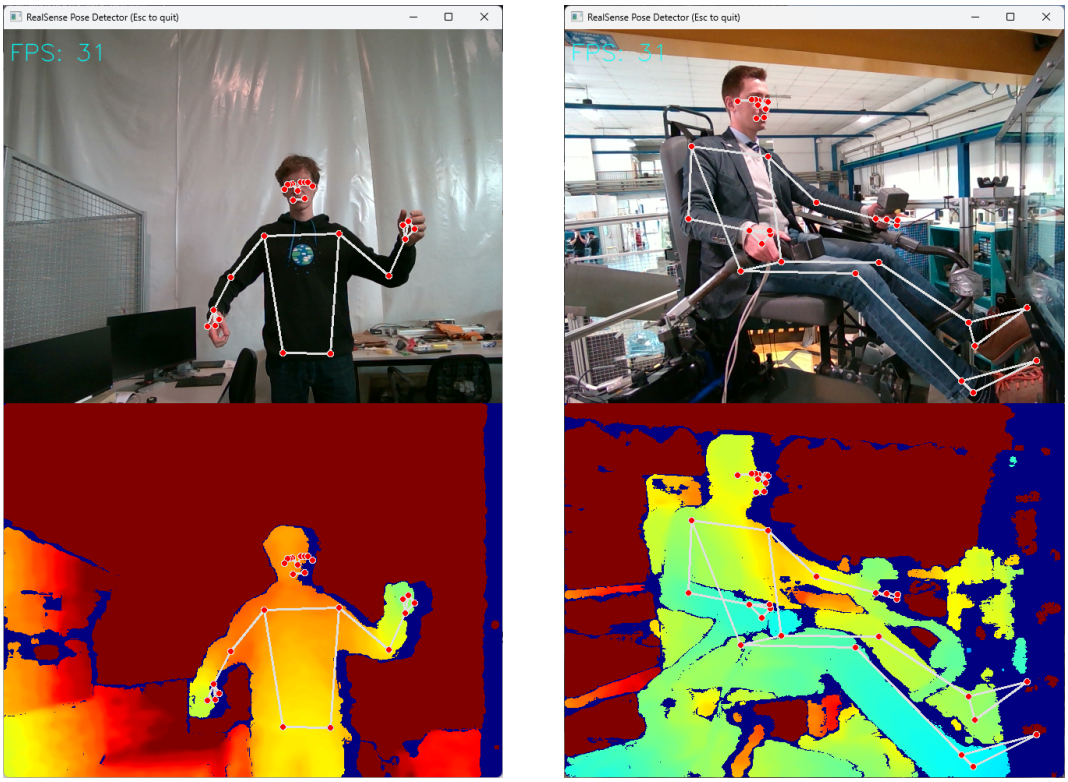
1. **2D Pose Estimation:** An external model identifies the 2D pixel coordinates (u, v) for each joint on the aligned color frame.
2. **Depth Lookup:** The raw depth value Z_{raw} is sampled directly from the aligned depth frame at the keypoint's pixel location (u, v).
3. **3D Projection:** The `librealsense` API's utility functions (e.g., `rs.rs2_deproject_pixel_to_point`) are used, taking the pixel location, depth value, and the camera's intrinsic parameters as input. This operation converts the 2D pixel and Z-depth into a precise 3D point (X, Y, Z) in the camera's reference frame, thus completing the body pose tracking process.

Visual Confirmation of System Integration

The utility of this system architecture is empirically demonstrated by the application output, as shown in Figure 4.23a and Figure 4.23b. The application successfully overlays the detected skeletal structure onto both the RGB and Depth streams [36]. In the RGB window (top), the pose model identifies the 2D keypoints. Crucially, the bottom window demonstrates the pose overlay on the pseudo-colorized depth map, illustrating two key aspects of successful hardware-software integration:

1. **Accurate Alignment:** The skeletal overlay aligns perfectly with the depth contours of the human subject, validating the function of the `rs.align` utility.
2. **Metrical Data Visualization:** The color variance in the depth map (e.g., red for

far, yellow/blue for near) demonstrates that the system is acquiring real metric data, which is then used in conjunction with the detected joints to calculate accurate 3D spatial positions. This validates the entire pose-to-point cloud workflow.



(a) (b)

Figure 4.23: Figure 4.23a: General human pose tracking and 3D keypoint projection demonstrating alignment between the RGB frame (top) and the Depth frame (bottom).
Figure 4.23b: Complex seated pose tracking within a helicopter cockpit mockup, demonstrating reliable depth acquisition in an industrial indoor environment with detailed skeleton mapping.

4.5. OPT-IN Instrumentation: Frustrated Total Internal Reflection (FTIR)

The *OPTical-INceptor (OPT-IN)* system is a novel sensing architecture developed to provide a seamless, non-intrusive method for measuring pilot grip pressure while simultaneously distinguishing between intentional control actions and involuntary biodynamic feedthrough [20, 68]. This system integrates a high-stiffness mechanical structure with an optical sensing layer based on the Frustrated Total Internal Reflection (FTIR) principle, ensuring that the measurement process does not compromise the mechanical impedance or the "crispness" of the flight controls [13, 68].

4.5.1. Mechanical Design and Operating Principle

The core innovation of the OPT-IN mechanism lies in its dual-path load transmission strategy, consisting of a rigid waveguide and a compliant probe [13].

1. **Rigid Waveguide:** The primary structural element is a central cylindrical waveguide manufactured from transparent Polycarbonate (PC). This component acts as the main load path, transmitting pilot forces from the grip directly to the support frame of the active inceptor. Under standard operation, this waveguide behaves as a rigid structure, ensuring full load transmission to the motor without introducing compliance that could alter the control feel [13].
2. **Compliant Interface (Probe):** The sensing interface consists of hemispherical probes made from medical-grade silicone (Shore A 40). These probes are housed within the grip's outer shell and act as a compliant interface.
3. **FTIR Transduction:** The waveguide is illuminated by an internal LED source. When the pilot applies pressure to the grip, the silicone probe compresses slightly against the waveguide surface. This contact frustrates the Total Internal Reflection (TIR) of the light within the cylinder, causing light to scatter at the contact point [13].
4. **Detection:** A photoresistor positioned behind the probe detects the variation in light intensity, which is directly proportional to the local contact pressure [13].

Crucially, the deformation induced by this process is negligible. The probe compression remains below 0.2 mm, corresponding to less than 0.1% of the cyclic stroke. This ensures the system preserves the stiffness and fidelity of the mechanical control path while acting as a parallel sensing layer [13].

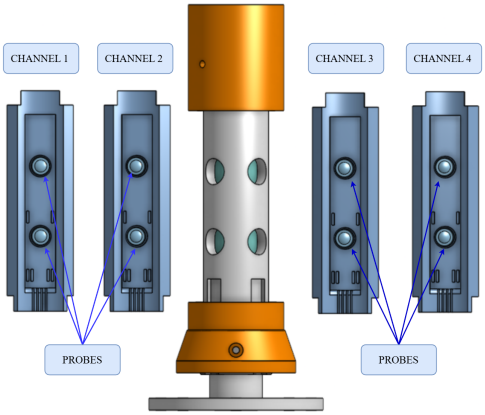
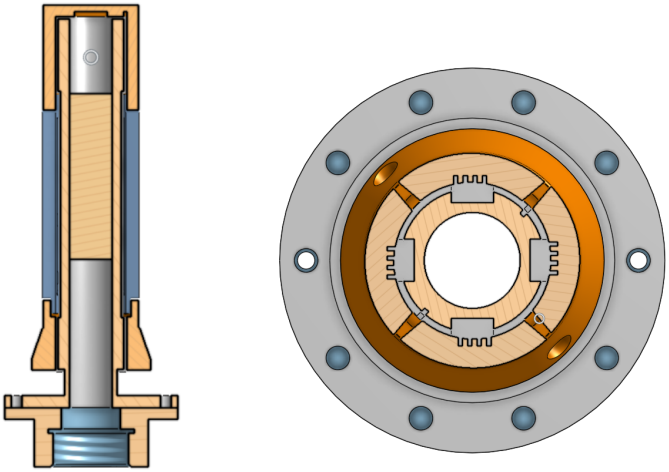


Figure 4.24: Schematic of the sensing channels. Four independent channels utilize probes to detect pressure variations across the waveguide surface, allowing for the spatial distribution of grip force to be monitored.(Source: (Source: Adapted from [13])



(a) (b)

Figure 4.25: Mechanical integration of the OPT-IN prototype sensor. Figure 4.25a: Front section view showing the central polycarbonate waveguide (grey) and the outer shell. Figure 4.25b: Top section view illustrating the four sensing units arranged radially around the waveguide to detect directional input. (Source: Adapted from [13])

Data Acquisition

The analog voltage signals (typically $0 - 5$ V) are acquired via a *LabJack T7* module (replacing earlier microcontroller implementations) and streamed in real-time to the MARSH simulation framework. The data is sampled at 20 Hz and processed using a low-pass Butterworth filter with a 10 Hz cutoff frequency to remove high-frequency mechanical noise [13].

The Opt-In Logic

A threshold-based logic is employed to determine if a pilot's input is a deliberate control action or an involuntary vibration (such as that caused by rotorcraft-pilot coupling). The activation state is defined as:

$$OptIn = \begin{cases} 1 & \text{if } F_{probe} > F_{th} \\ 0 & \text{otherwise} \end{cases} \tag{4.2}$$

Where F_{th} is a threshold typically set to 2 N. This threshold represents the minimum force distinguishable from background grip pressure and biodynamic tremor.

5 | Experimental setup: Test Aircraft and Flight Simulation

5.1. Test Aircraft Configuration

The aircraft dynamics subject to this evaluation are computed through sophisticated mathematical models integrated into the flight dynamics modules of the RPC simulator. These numerical models rely on the comprehensive aeromechanical data and theoretical methodologies originally published by Padfield [47]. Furthermore, these baseline models have been substantially expanded and refined by the FRAME Lab to include higher-fidelity representations of rotor aerodynamics and structural dynamics, which are crucial for capturing complex phenomena such as Rotorcraft-Pilot Couplings [44]. This modeling approach enables the real-time simulation of a comprehensive range of rotorcraft platforms, allowing the system to be configurable to meet specific Mission Task Elements (MTEs) and handling qualities requirements. The system's scope encompasses:

- **Classification Range**: The simulation capabilities extend across a wide spectrum of the rotorcraft fleet, ranging from light-weight, high-maneuverability platforms to heavy-class multi-engine helicopters, encompassing varying mass properties and moments of inertia.
- **Dynamic Scaling**: The architecture allows for scalable simulation fidelity, making it suitable for diverse operational scenarios, from agile utility missions requiring high responsiveness to stable heavy-transport operations.
- **Configuration**: The modular design supports a reconfigurable architecture capable of representing various rotor systems (e.g., articulated, hingeless) and distinct fuselage aerodynamic characteristics.



(a) (b)

(c) (d)

Figure 5.1: An overview of selected helicopter types simulable via the RPC simulator at FRAME Lab. (Source: Fig 5.1b Tajul H, CC BY 4.0 <https://creativecommons.org/licenses/by/4.0>, via Wikimedia Commons; Fig 5.1c Mass Communication Specialist 2nd Class Joe Bishop, Public domain, via Wikimedia Commons; Fig 5.1d Konflikty.pl, Public domain, via Wikimedia Commons)

5.2. Vertical Maneuver - RPC Evaluation

This section outlines the protocols for the Vertical Maneuver (often referred to as Vertical Repositioning). This maneuver, especially when utilizing a simplified flight model with just 2 DOFs, facilitates the study of RPC phenomena linked to rotor coning and heave axis controllability. The test criteria are rigorously derived from the *Aeronautical Design Standard Performance Specification for Handling Qualities of Military Rotorcraft* (ADS-33E-PRF) [64], specifically Section 3.11.6, with adaptations developed at the FRAME Lab of Politecnico di Milano.

Recent academic research, such as the work by Marchesoli [39], has further highlighted the importance of immersive simulation and biomechanical analysis in understanding pilot performance during such maneuvers.

5.2.1. Objectives

For a Scout/Attack rotorcraft, the objective of this maneuver is to simulate a rapid unmask/remask profile with an aiming task at the unmask position. For Utility or Cargo rotorcraft, it assesses heave axis controllability during precision station keeping. The specific checks defined by ADS-33E include:

- Assessment of adequate heave damping, i.e., the ability to precisely initiate and arrest a vertical rate.
- Assessment of adequate vertical control power.
- Assessment of undesirable coupling between the collective and the pitch, roll, and yaw axes.
- Assessment of the characteristics of the heave axis controller, especially if a non-conventional controller is used (e.g., a four-axis sidestick).
- In the presence of an external load, assessment of undesirable interaction between the heave controller and other axes, as well as complications induced by load dynamics.

5.2.2. Maneuver Description

According to the standard, the maneuver is initiated from a stabilized hover at a specific reference altitude. The pilot must execute the following sequence:

From a stabilized hover at an altitude of 15 ft, initiate a vertical ascent of 25 ft, stabilize the helicopter, then descend back to the initial hover position. In the Good Visual Environment (GVE), the maneuver shall be accomplished in calm winds and in moderate winds from the most critical direction.

Flight Maneuver Specification

1. **Initial Condition**: The rotorcraft is positioned in a stabilized hover at the initial reference altitude ($h_1 = 15$ ft AGL).
2. **Vertical Ascent (Unmask)**: The aircraft shall traverse vertically from h_1 to the target altitude ($h_2 = 40$ ft AGL), corresponding to a standard ascent of 25 ft.
3. **Station Keeping (Unmask)**: Upon reaching altitude h_2, the aircraft shall maintain a stable hover for a minimum duration of 2 seconds. Vertical deviation must be constrained within the tolerances defined in the performance standards.
4. **Vertical Descent (Remask)**: The aircraft shall descend from h_2 returning to the initial altitude h_1 (15 ft AGL).

5. **Terminal Station Keeping**: Upon returning to altitude h_1, the aircraft shall execute a stable hover to complete the maneuver.

6. **Landing**: To complete the flight test and try to trigger RPC phenomena, the pilot will be asked to proceed with a landing to evaluate the coupling that is generated between the helicopter model and the ground.

5.2.3. Test Course Specification

The test course shall consist of ground markings that clearly define desired and adequate performance zones. It is suggested that this maneuver utilize the standard hover course (refer to Figure 5.2) with a second reference symbol or hover board positioned to align at the upper reference altitude (40 ft).

In addition to demonstrating potential RPC triggers, the pilot must perform a landing to evaluate possible dynamic coupling between the helicopter and the landing surface dynamics.

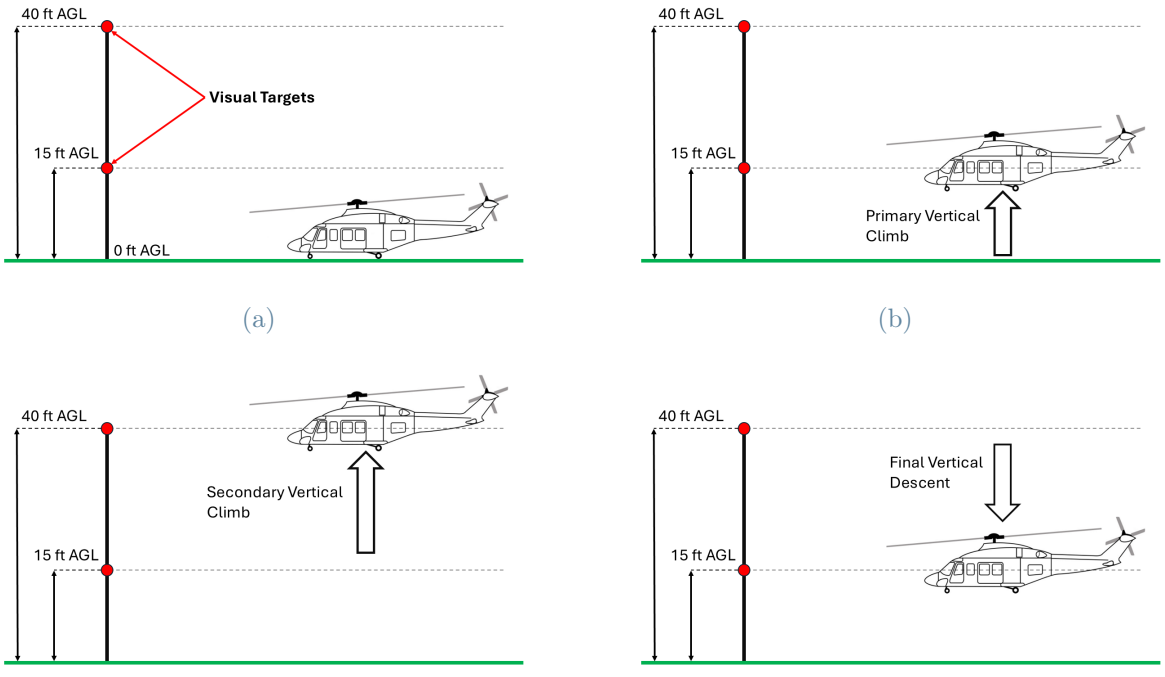


Figure 5.2: Suggested course layout for Vertical Reposition maneuver [64]. The image sequence is as follows:
Figure 5.2a: Take off
Figure 5.2b: First climb and first stabilization at 15 ft AGL
Figure 5.2c: Second climb and second stabilization at 40 ft AGL
Figure 5.2d: Final descent and stabilization at 15 ft AGL

5.2.4. Performance Standards

The pilot must maintain specific flight parameters to achieve *Desired* or *Adequate* performance ratings. Failure to meet Adequate standards constitutes a failure of the test point. Table 5.1 details the standards for the Scout/Attack configuration in both Good Visual Environment (GVE) and Degraded Visual Environment (DVE) as per ADS-33E Section 3.11.6.

Table 5.1: Performance - Vertical Maneuver

Metric	**Scout/Attack**		**Cargo/Utility**		**Ext. Slung Load**	
	GVE	**DVE**	**GVE**	**DVE**	**GVE**	**DVE**
DESIRED PERFORMANCE						
Maintain longitudinal and lateral position within $\pm X$ ft	6	10	3	3	3	3
Maintain start/finish altitude within $\pm X$ ft	3	3	3	3	4	4
Maintain heading within $\pm X$ deg	3	3	5	5	5	5
Complete the maneuver within (sec)	10	13	13	15	13	15
ADEQUATE PERFORMANCE						
Maintain longitudinal and lateral position within $\pm X$ ft	10	20	6	6	6	6
Maintain start/finish altitude within $\pm X$ ft	6	6	6	6	6	6
Maintain heading within $\pm X$ deg	6	6	10	10	10	10
Complete the maneuver within (sec)	15	18	18	18	20	20

5.3. Vertical Repositioning Simulations

The experimental trials were conducted at the FRAME Lab of Politecnico di Milano. These tests encompassed a series of scenarios replicating the standards outlined in ADS-33E, utilizing a 2-DOF flight model (altitude variation and rotor coning), while introducing varying turbulence conditions and modifications to helicopter simulation parameters, such as the rotor gain.

5.3.1. Simulated Environment

The visual system implementation was developed using the Godot engine, selected for its efficient system architecture and capability to interface with the *LIDIA* Python library for rendering cockpit instruments. A two-level tower was constructed to serve as a reference, encompassing obstacles suggested by ADS-33E but modifying the vertical repositioning task to provide specific hovering references at 15 and 40 feet above ground. Each level features a specific marker requiring the pilot to stabilize the aircraft within the limits prescribed by ADS-33E [64]. The environment supports dynamic parameter adjustment—such as fog density and starting offsets—via MAVLink messages. The experiments can be conducted using either the simulator's physical displays or a Virtual Reality (VR) headset; the application prioritizes VR initialization for a more immersive experience, automatically defaulting to a standard pilot viewpoint if VR hardware is unavailable.

As previously mentioned, the simulated flight test relies on the techniques defined in ADS-33E. Specifically, the pilot is tasked with stabilizing the helicopter such that a red marker remains clearly visible within a bright green band from the pilot's Point of View (POV). The primary objective is to maintain the helicopter's position despite oscillations caused by perturbations. The maneuver consists of a vertical repositioning between two different height levels, which must be completed within a designated timeframe, followed by vehicle stabilization.

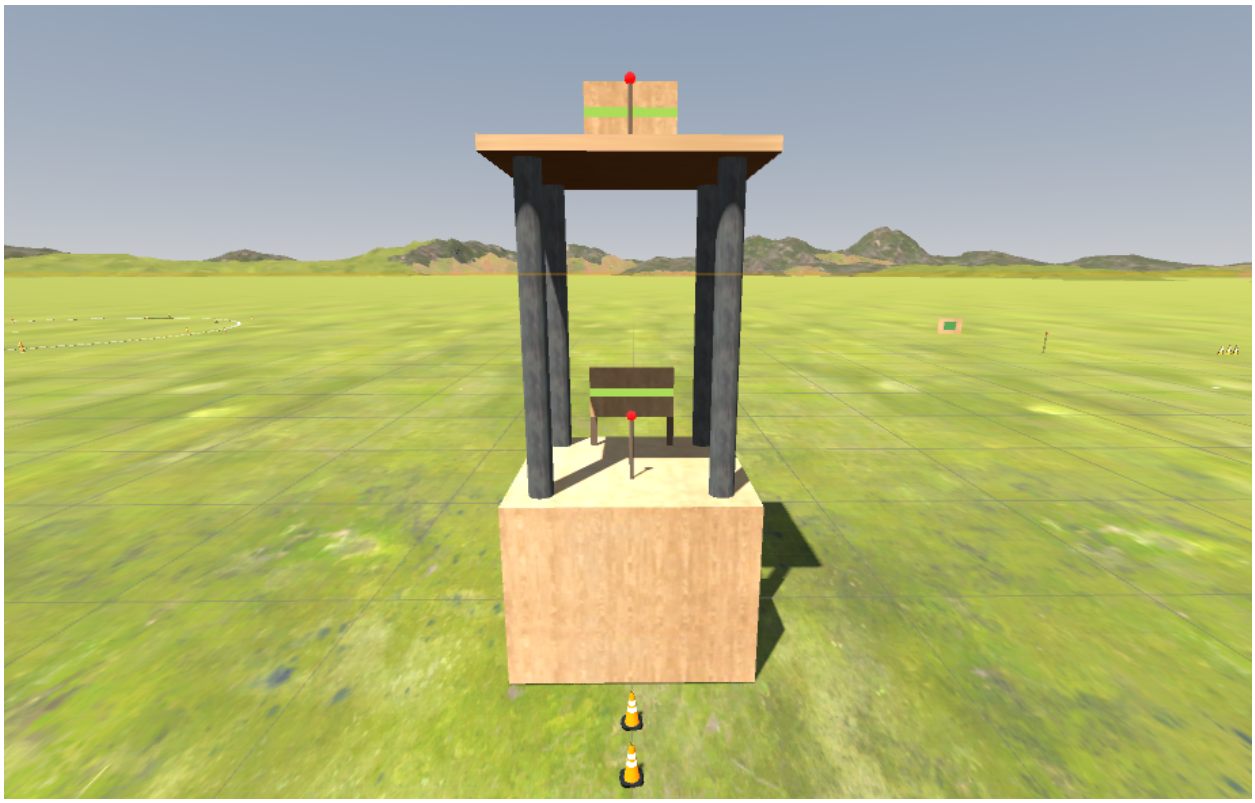


Figure 5.3: Representation of the tower used to simulate vertical repositioning maneuvers. The two levels are clearly visible, highlighting the red markers that indicate the correct hovering position. (Source: Adapted from [40])

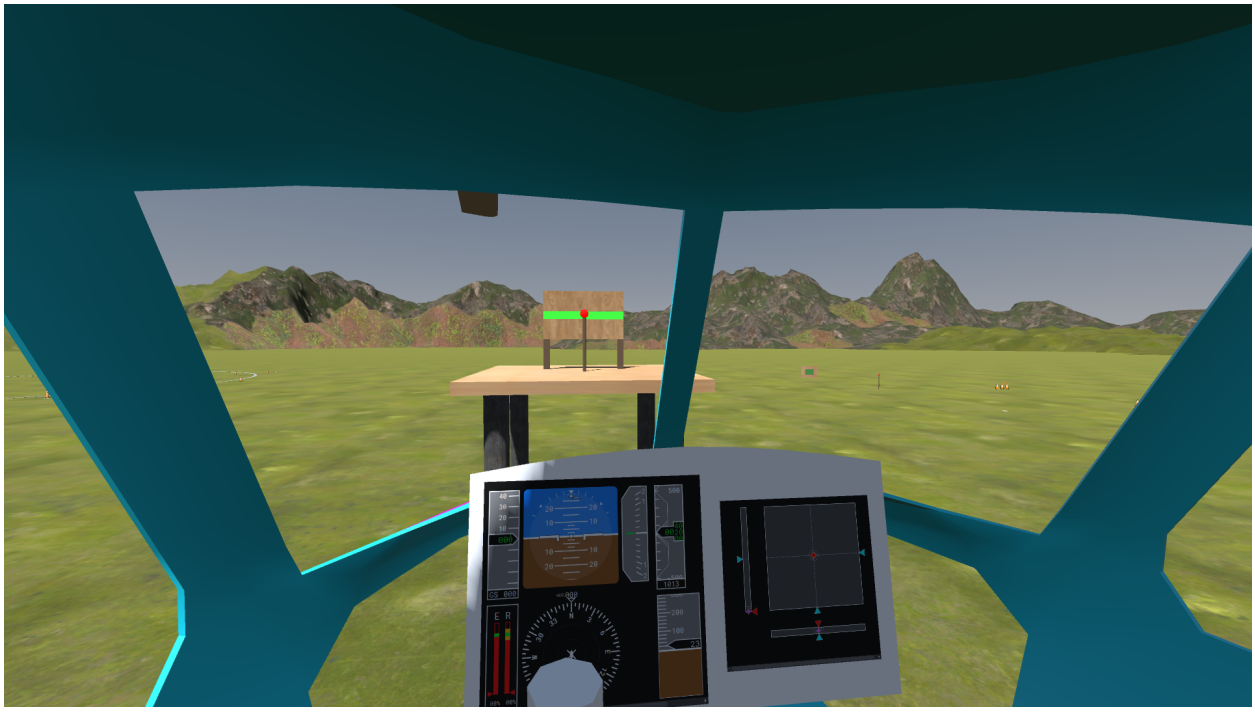


Figure 5.4: The pilot's Point of View (POV) during the simulated trials. (Source: Adapted from [40])

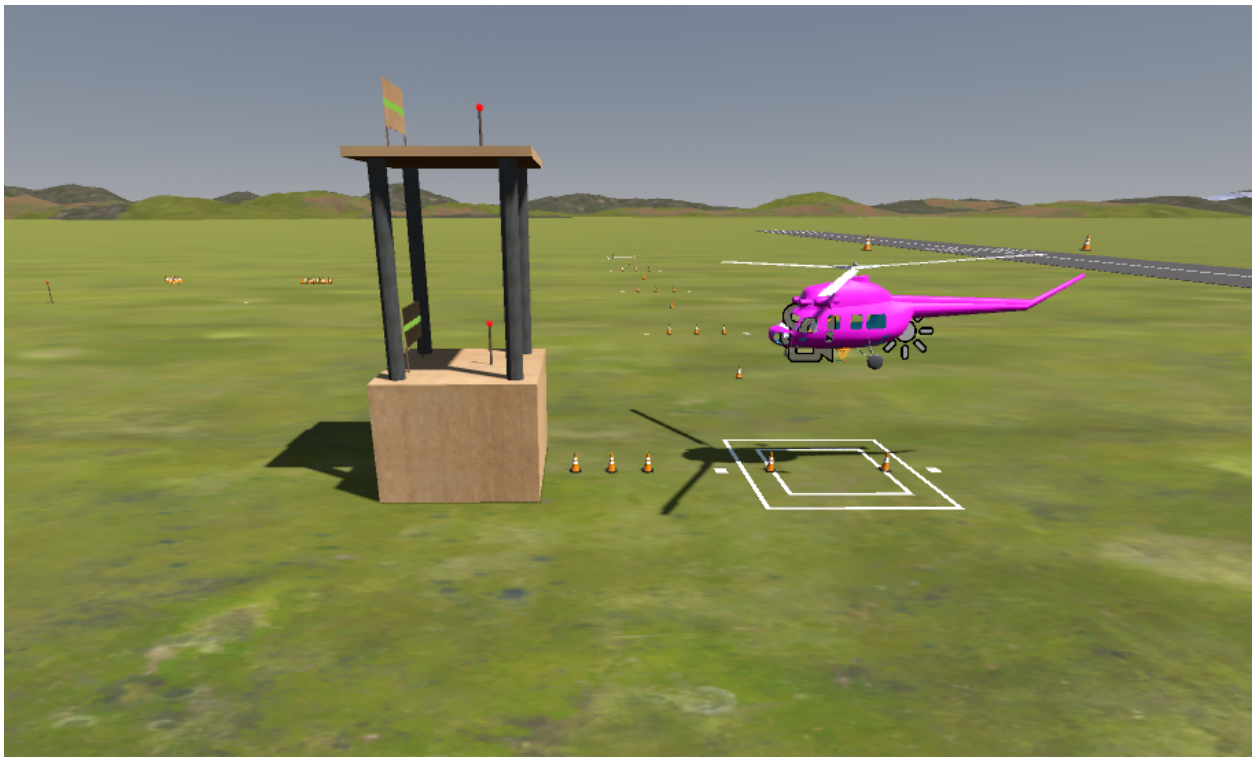


Figure 5.5: An external point of view utilized during the simulated trials. (Source: Adapted from [40])

5.3.2. Pilot Preparation

The subject pool consists of volunteers who are briefed on the tracking task and the experiment's objectives [39]. Prior to the experiment, demographic and biometric data are collected to populate a database, including age, gender, height, and weight [39]. For professional pilots, additional data regarding flight hours on rotorcraft and fixed-wing aircraft, as well as specific models flown, is recorded.

6 | Final Assembly and Results

6.1. Final Hardware Assembly

A primary objective of this thesis work was to integrate the complete suite of selected sensors onto the RPC Test Rig to enable the experimental investigation on correlations between physiological signals and pilot workload. The sensor layout was designed based on practical considerations, aiming to optimize the available space on the platform effectively.

A dedicated Personal Computer (Named RPC-VR or Pilot PC) is positioned at the base of the simulator, serving as the central hub for connecting the various sensors, managing data acquisition, and rendering the simulator's graphics.

Figure 6.1 illustrates the final arrangement of the various modules and sensors on the simulator structure in the configuration utilized during the physiological sensors evaluation tests.

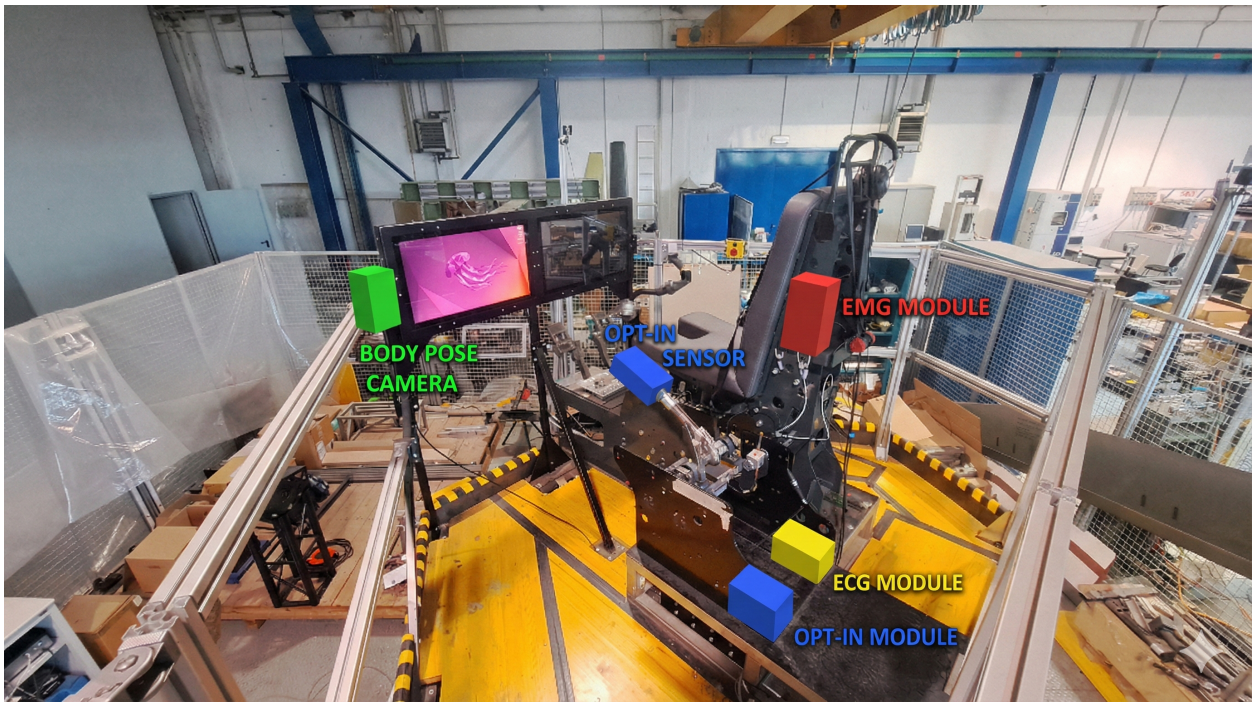


Figure 6.1: Diagram illustrating the final spatial arrangement of the various sensor modules integrated into the simulator platform.

6.1.1. sEMG Module

The placement of the Surface Electromyography (sEMG) sensor was necessitated by physical constraints inherent to its form factor and measurement system. Consequently, the acquisition card was anchored to the structure on the rear left side of the pilot's seat for the following reasons:

- **Electrode Cabling**: The card provided by LWT3 utilizes a wired system that physically connects the acquisition unit directly to the electrodes. Therefore, it is necessary to arrange the cabling to prevent interference or entanglement with moving parts. This is particularly critical as RPC phenomena studies focus heavily on the left arm, which is used to manipulate the collective lever.
- **Data Acquisition Connection**: To facilitate data acquisition, a USB-C docking station was installed at the base of the seat. While initially intended for connecting simulator components such as the intercom communication system, this hub was utilized to connect the sEMG acquisition card via its USB interface, enabling direct data transmission.

An image showing the housing of the card on the back of the seat is provided below.

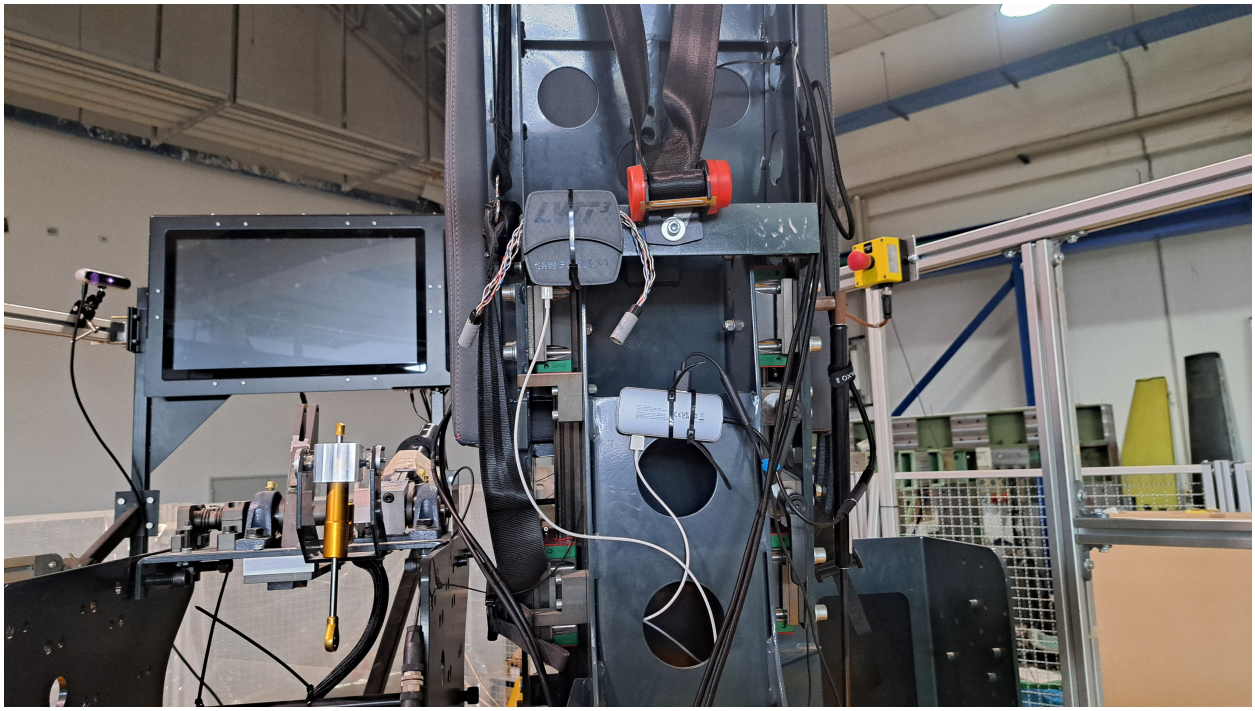


Figure 6.2: Photograph showing the installation of the sEMG data acquisition card on the left side of the pilot's seat. The docking station is visible below, providing power to the card, transmitting data, and acting as a hub for the intercom communication system.

6.1.2. Eye Tracking Module

The integration of the eye-tracking system, consisting of the Pupil Labs Core glasses, was achieved by routing a dedicated USB-C cable that connects the glasses directly to the pilot's PC, thereby enabling continuous data acquisition.



Figure 6.3: The image clearly shows the positioning of the electrodes on the pilot's left arm and the hardware part of the eye tracking system.

6.1.3. ECG Module

The final assembly of the Electrocardiogram (ECG) sensor involved two distinct phases.

Sensor Case Assembly

As described in Section 4.3, the system comprises various interconnected modules. To ensure mechanical stability, a custom case was manufactured using 3D printing technology. This enclosure houses the constituent boards—specifically the red AD8232 ECG acquisition board, the white ST Nucleo management board, and the blue microSD memory module—securing them to a rigid surface to prevent unwanted movement during operation.

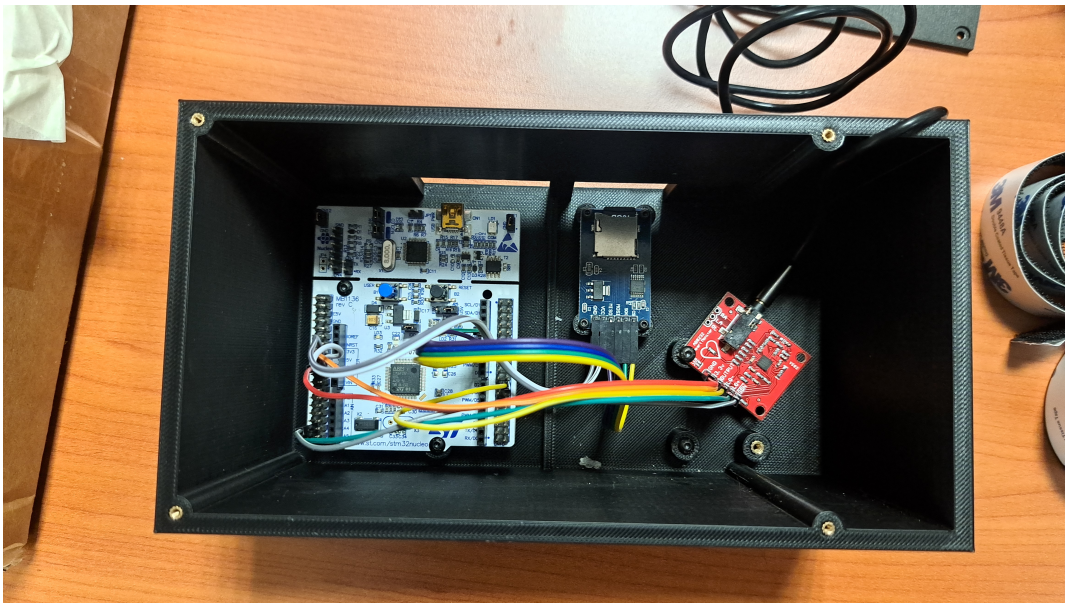


Figure 6.4: Photograph of the assembled ECG module case. The internal components are visible: the red AD8232 ECG acquisition board, the white ST Nucleo management board, and the blue microSD memory management board.

Installation on the Simulator

The second phase involved the direct integration of the module onto the simulator. To maximize space efficiency, the case containing the sensor was positioned in a recess beneath the collective lever in a rearward location. This position facilitates the connection of the electrode cables for monitoring the pilot's cardiac activity while ensuring they do not interfere with the operation of the collective control lever.

As previously mentioned, the system stores data locally on a microSD card; therefore, it is not directly connected to a PC for data transfer. Electrical power is supplied by a $20,000$ mAh power bank.

To synchronize the start and stop of data acquisition, a trigger signal is sent by a LabJack T7 via the MARSH software environment.

Both the case and the power bank were secured to the simulator's metal structure using heavy-duty Velcro strips.



Figure 6.5: Photograph showing the installed position of the ECG module case and its respective power supply unit (power bank).

6.1.4. Body Pose Module

Regarding the Body Pose module, the Intel RealSense D455f camera was mounted using a rigid clamp directly onto the platform frame, positioned to ensure an unobstructed field of view of the pilot's left side.

A dedicated USB-C cable was routed between the camera and the pilot's PC to provide both power and high-bandwidth data transfer.



Figure 6.6: Attachment of the body pose camera to the platform structure.

6.1.5. OPT-IN Module

The OPT-IN module utilized for these tests shares a similar architectural composition with the ECG module presented in Subsection 6.1.3.

Sensor Case Assembly

Analogous to the ECG module, a thermoplastic case was 3D printed (similar to that described in Subsection 6.1.3) to house all electronic components of the system.

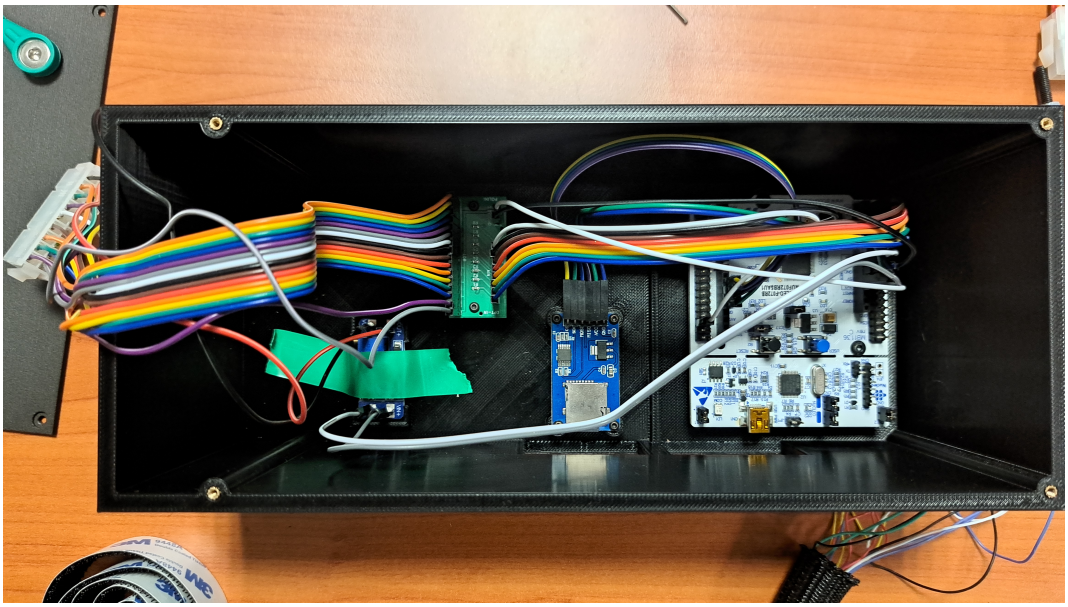


Figure 6.7: Photograph of the OPT-IN module case. The internal layout mirrors that seen in Figure 6.4. The cabling connecting the pressure sensor on the collective lever is clearly visible.

Installation on the Simulator

The OPT-IN module case was also positioned beneath the collective lever, adjacent to the ECG module. This module is similarly powered by an independent power bank, saves data to a local microSD card, and receives a synchronization trigger via MARSH through the LabJack T7 interface.

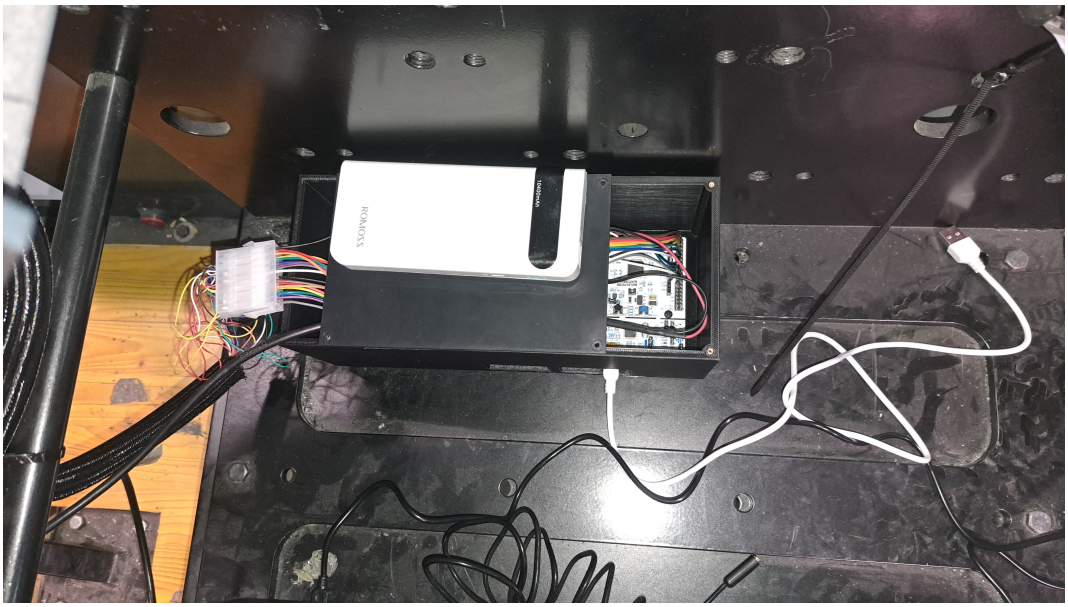


Figure 6.8: Photograph showing the installed position of the OPT-IN module case and its respective power supply unit.

Regarding the installation of the pressure sensor on the collective lever, the modular grip attachment architecture developed by the FRAME Lab was utilized. A 3D-printed interface, analogous to existing aluminum adapters in the laboratory, was fabricated to connect the sensor to the lever tube, thereby integrating the various system components seamlessly.

Concerning cabling management, the connector and the cable bundle were secured to the interface and the upper section of the tube using nylon zip ties. This arrangement prevents tension on the cables and avoids any mechanical obstruction to the lever's range of motion.

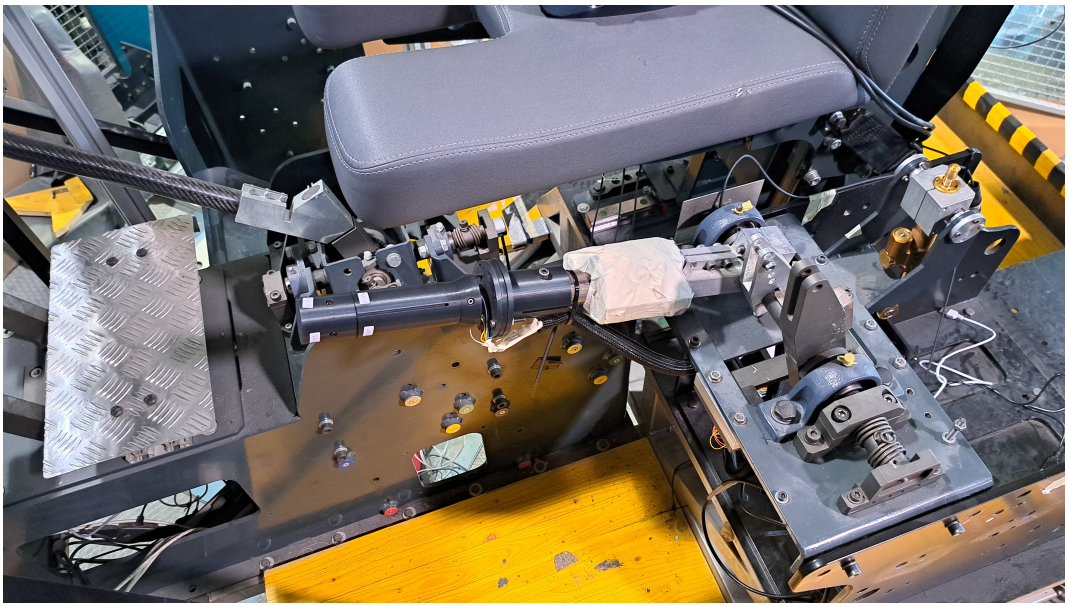


Figure 6.9: Photograph showing the OPT-IN sensor mounted on the collective lever. The mechanical connection to the structure is enabled by a custom 3D-printed interface.

6.2. Final Software Implementation

Regarding the organization and final deployment of the software infrastructure governing signal acquisition, the MARSH communication protocol was extensively utilized. The technical specifications and architecture of this protocol are comprehensively described in Appendix B. This standardized framework facilitated the seamless integration of heterogeneous sensor modules into the simulation environment.

For each hardware component, a dedicated software interface was developed to establish robust communication between the specific module and the central MARSH Manager. These implementations are detailed in Subsections 4.2.2, 4.3.2, 4.4.2, and 4.5.1.

6.2.1. Synchronization and Data Logging

To ensure precise temporal alignment across different data streams — a critical requirement for correlating physiological responses with flight maneuvers — a centralized synchronization strategy was adopted. The data acquisition command for all subsystems is synchronized via a hardware digital trigger system managed by the LabJack T7 unit. This mechanism minimizes latency and ensures that all recordings commence simultaneously, thereby facilitating accurate post-hoc analysis.

Furthermore, specific optimization was required for high-bandwidth systems, namely the Eye Tracking and Body Pose modules. For these sensors, custom telemetry messages were defined within the architecture. This implementation enables the associated software drivers to log collected sensor data directly in the binary `.tlog` format. This approach not only streamlines the data collection process but also allows for rapid preliminary inspection and validation of the datasets immediately following experimental sessions.

6.2.2. Post-Processing and Analysis

Finally, to complete the data processing workflow, custom MATLAB scripts were utilized. These scripts were designed to perform advanced signal processing tasks, including data parsing, noise filtering, and feature extraction. This allowed for a significantly more in-depth visualization and analysis of the pilot's physiological state compared to raw data inspection. The methodologies and results of these specific analyses are presented in Subsections 4.1.2, 4.2.3, and 4.3.3.

6.3. Preliminary Sensors Results

Leveraging the assembled sensor ecosystem, a series of preliminary measurements were conducted to verify the stable co-operation of all sensors and to evaluate an initial, simplified

correlation with pilot workload trends.

6.3.1. sEMG Results

For the simulated flight trials, the pilot's left arm was instrumented to evaluate muscle activity during maneuvers requiring the operation of the collective control.

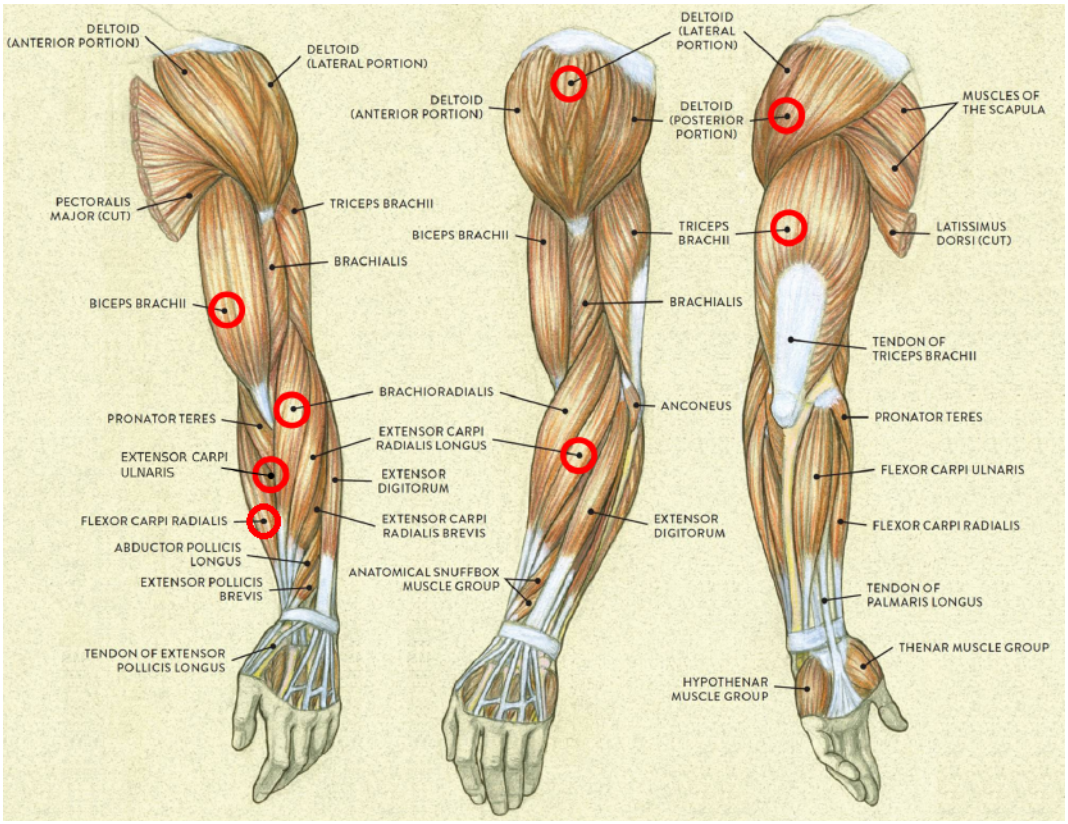


Figure 6.10: Position of the sEMG sensors on the pilot's left arm [39]. (Source Adapted from [39])

The results regarding muscle activity measurements collected via sEMG are evaluated based on the specific gear ratio setting selected during the trial.

Specifically, the analysis for each muscle focuses on the filtered signal, the Root Mean Square (RMS) amplitude, and muscle fatigue analysis via specific spectral trends. It is important to note that while standard practice often involves normalizing the signal against the Maximum Voluntary Contraction (MVC) under isometric conditions, this study focuses on the qualitative trend of the signal rather than its absolute quantitative value.

Professional Pilot

As illustrated in Figures 6.11, 6.12, and 6.13, two distinct regions can be identified for each muscle:

1. **Active Muscle Phase**: This phase corresponds to the execution of the simulated flight task involving repositioning between visual targets. Specifically, the signal magnitude (Figure 6.11) and RMS (Figure 6.12) are elevated. Consequently, the Mean Spectral Frequency (MNF) (Figure 6.13) generally tends to decrease over time during this phase, following the trend indicated by the dashed line. The red color indicates fatigue (negative slope of the interpolating line), while green indicates an absence of fatigue.

2. **Relaxation Phase**: This phase exhibits an inversion of the behavior observed in the previous phase. This is attributed to the pilot rapidly releasing the collective control, leading to a relaxation of the arm musculature, a behavior clearly evidenced by the positive trend of the MNF.

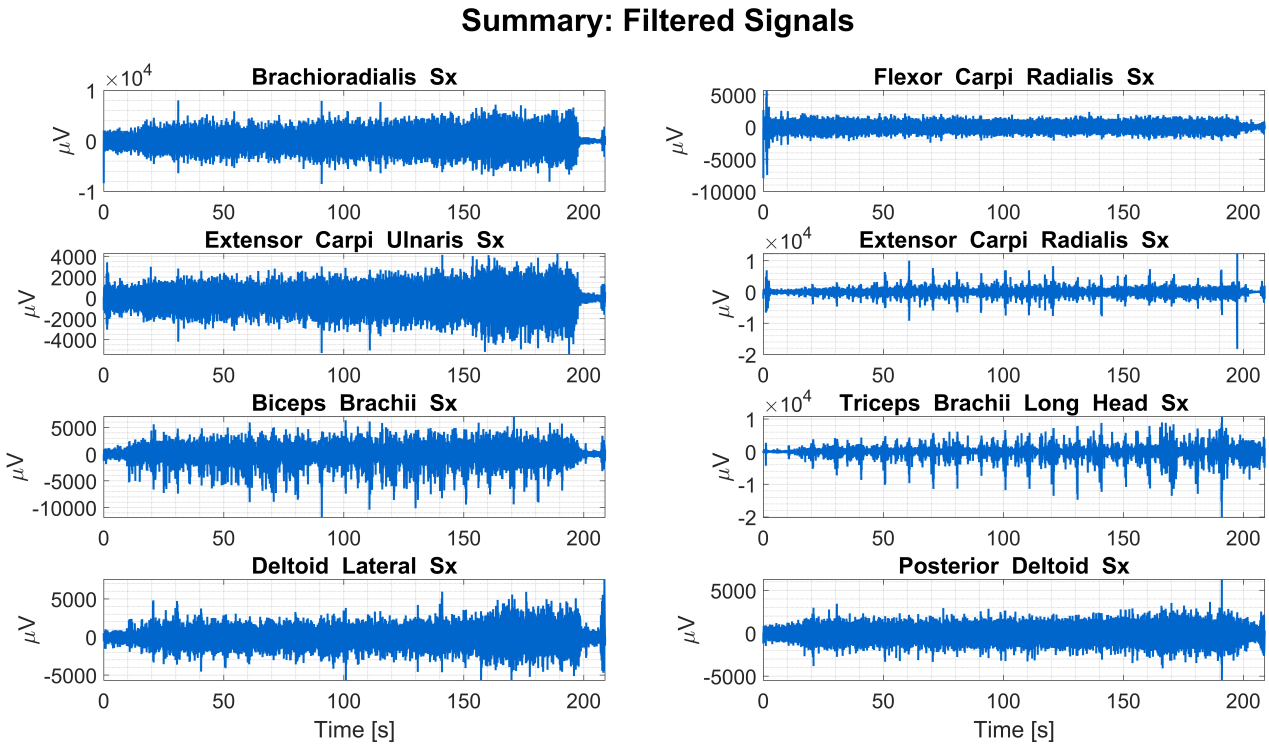


Figure 6.11: Filtered sEMG signals for all muscles (Professional Pilot).

A notable observation regarding Figure 6.12 is the presence of a series of peaks immediately preceding the relaxation phase. This effect is attributable to the simulated landing phase, where dynamic coupling effects between the helicopter and the ground are triggered, consequently inducing Rotorcraft-Pilot Coupling (RPC) effects that also involve the pilot.

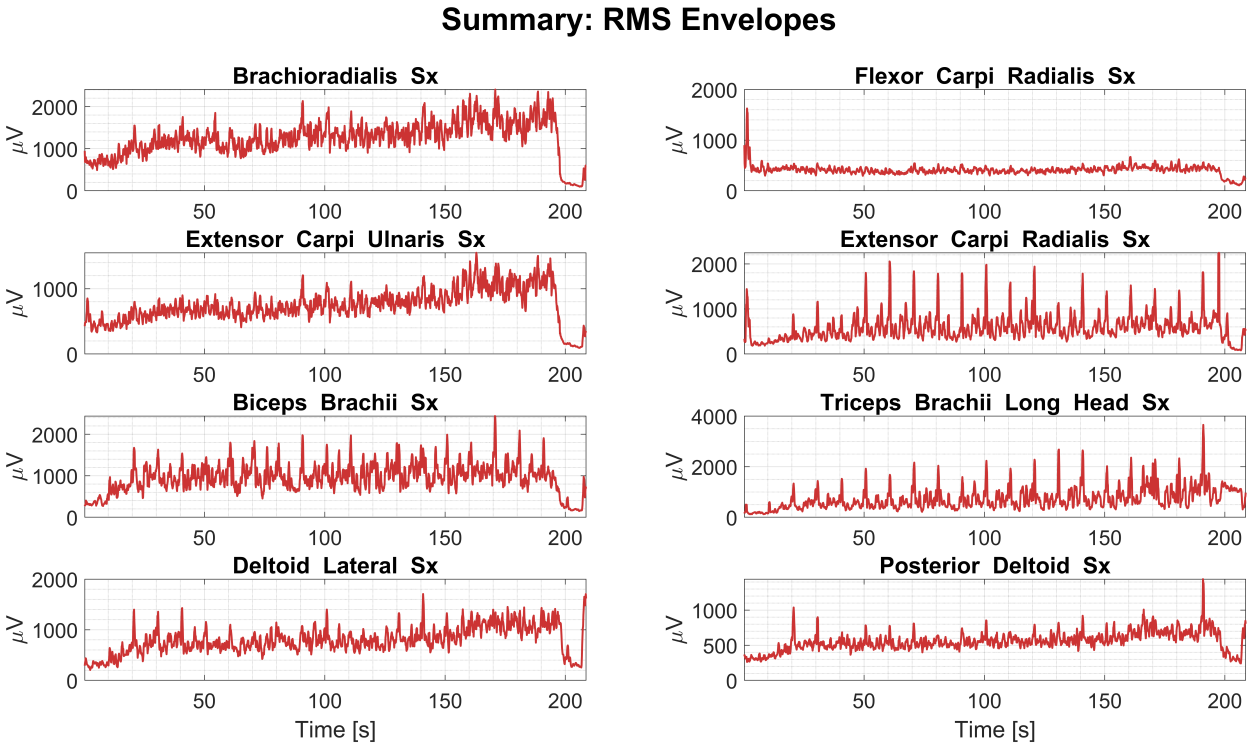


Figure 6.12: RMS values for all muscles (Professional Pilot).

Regarding the calculated fatigue trends (Figure 6.13), it is evident that during the trial, the arm musculature undergoes fatigue, highlighted by a decrease in MNF over time.

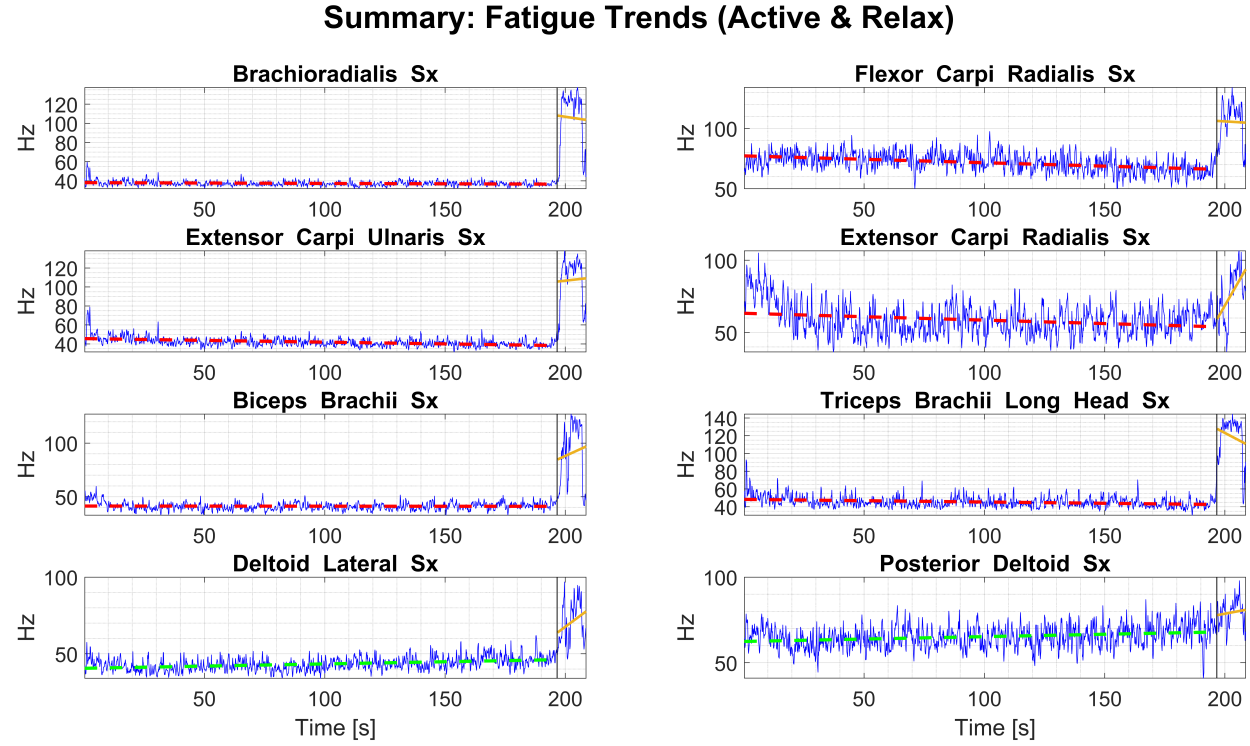


Figure 6.13: Muscle fatigue analysis (Professional Pilot).

Non-Pilot

In the analyses performed with a Non-Pilot subject, the observations regarding the segmentation of phases remain consistent with those seen for the Pilot subjects.

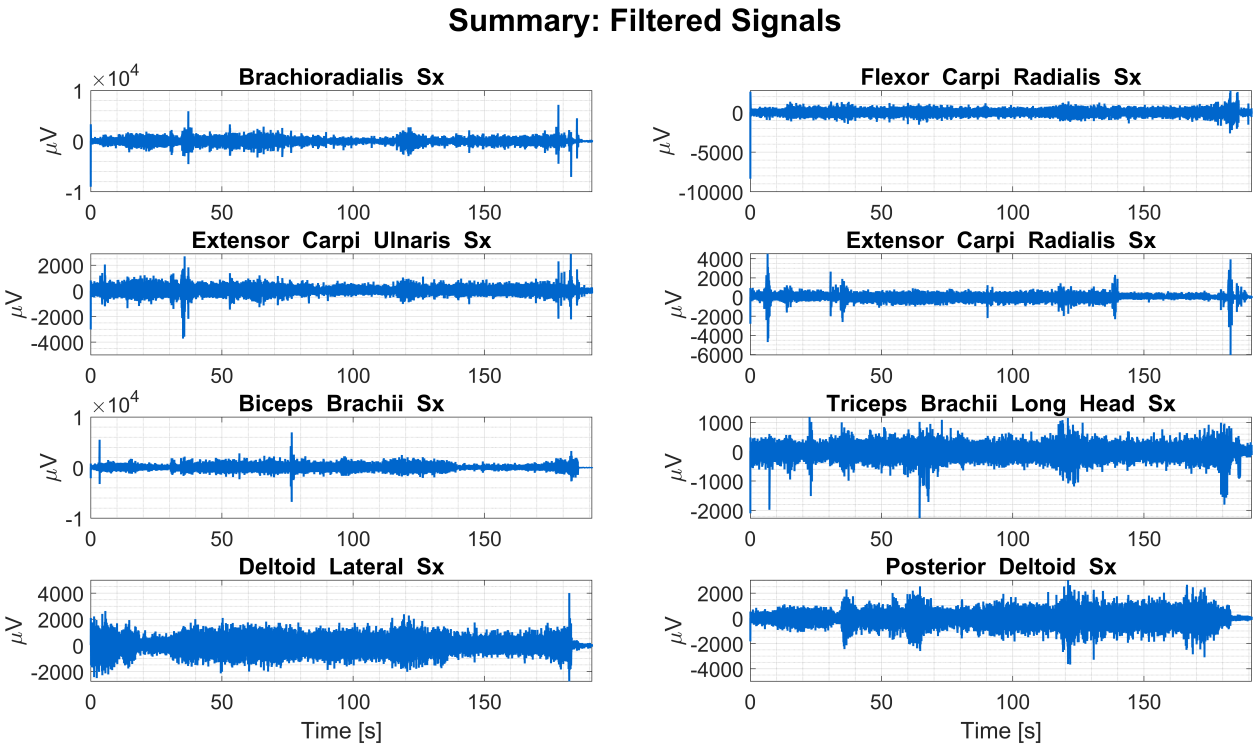


Figure 6.14: Filtered sEMG signals for all muscles (Non-Pilot).

The maximum RMS values recorded for the specific muscles of both the Professional Pilot and Non-Pilot (for Professional Pilot figure 6.12 and for Non-Pilot figure 6.15) warrant careful interpretation. As established earlier in this section, the primary objective of this analysis is to evaluate overall data trends rather than absolute signal amplitudes, as the raw data were not normalized to a reference metric such as MCV. Consequently, variances in absolute signal intensity may be attributable to multiple confounding factors, including inter-subject physical and physiological differences.

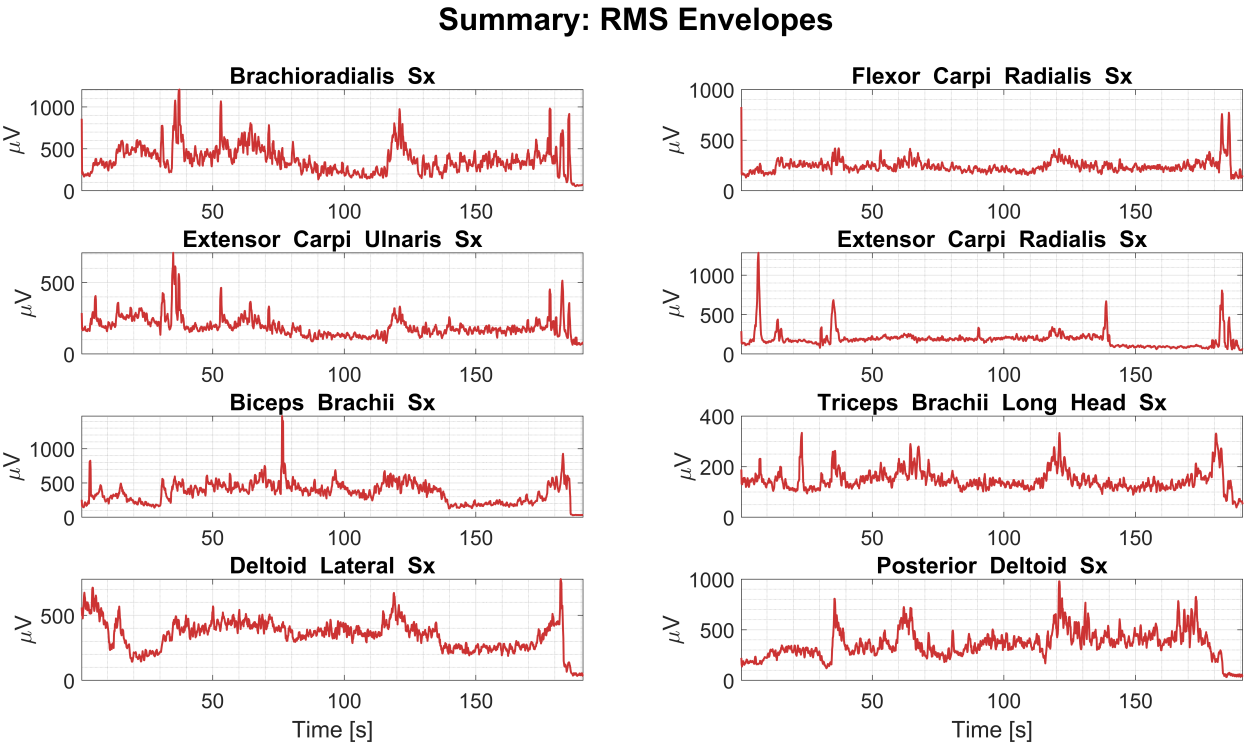


Figure 6.15: RMS values for all muscles (Non-Pilot).

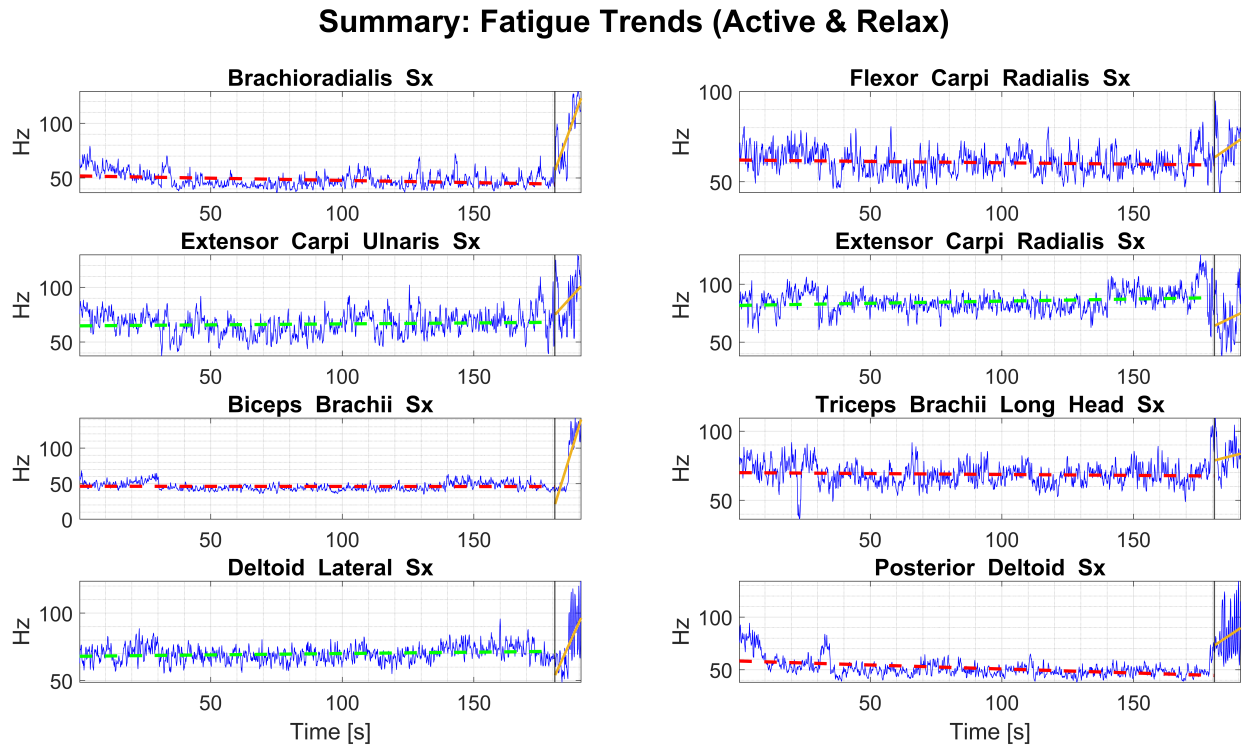


Figure 6.16: Muscle fatigue analysis (Non-Pilot).

6.3.2. Eye Tracking Results

For the eye-tracking module, the following metrics were considered:

- Pupil diameter.
- Blink duration and blink rate.
- Fixation events.

Professional Pilot

Due to a technical issue encountered during the trial, it was not possible to acquire eye-tracking data for the professional pilot.

Non-Pilot

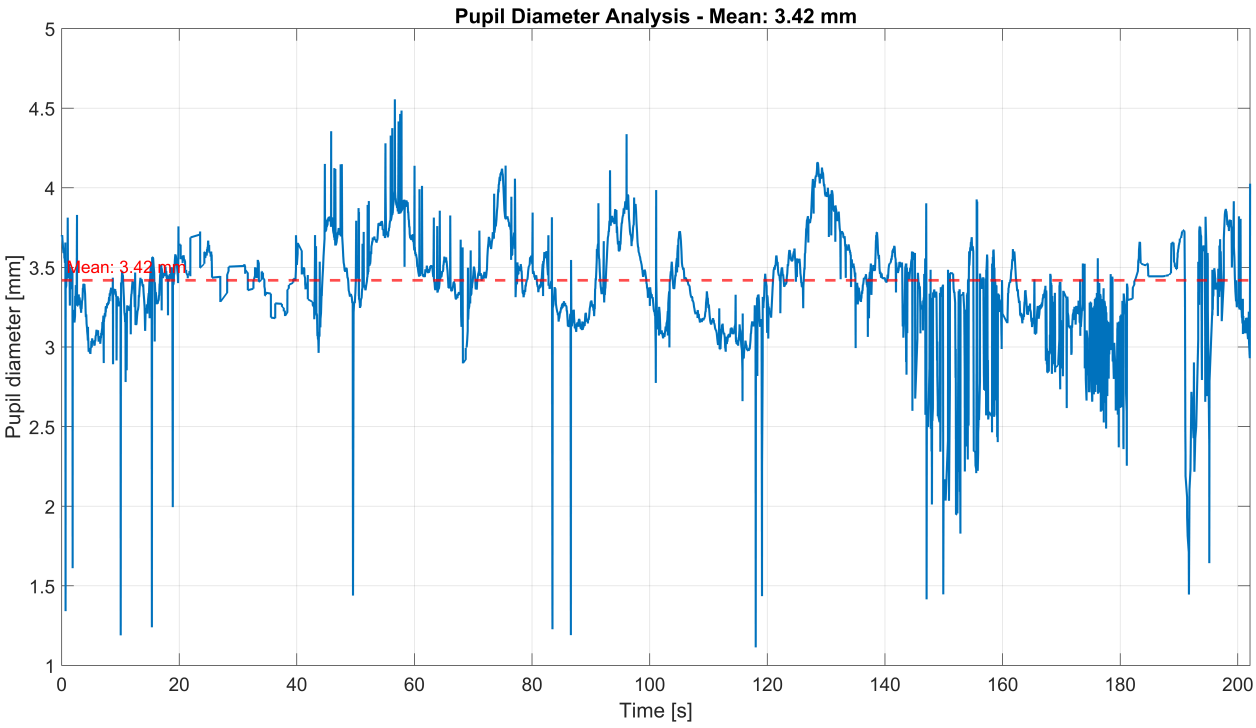


Figure 6.17: Pupil diameter analysis (Non-Pilot).

In Figure 6.18, it is possible to observe two distinct regions where the blink rate assumes minimum values. These minima correspond to the visual tracking phases during the vertical repositioning task and the final landing phase, indicating periods of heightened visual attention.

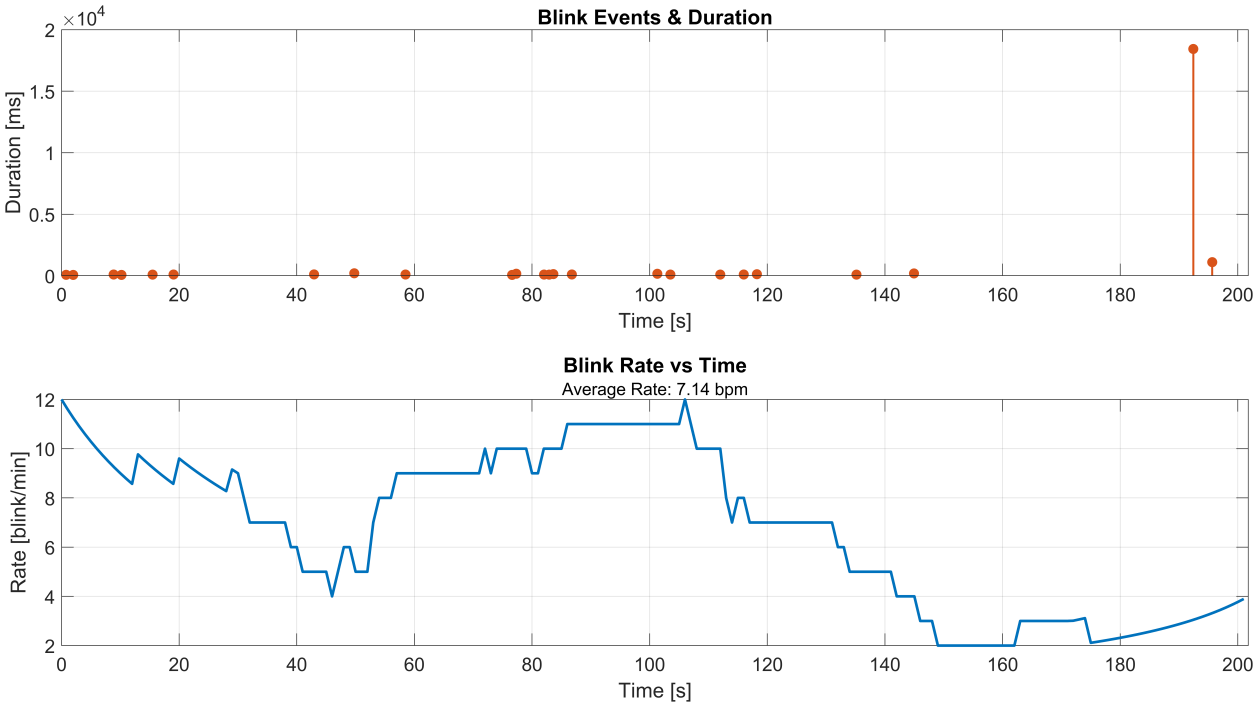


Figure 6.18: Blink analysis (Non-Pilot).

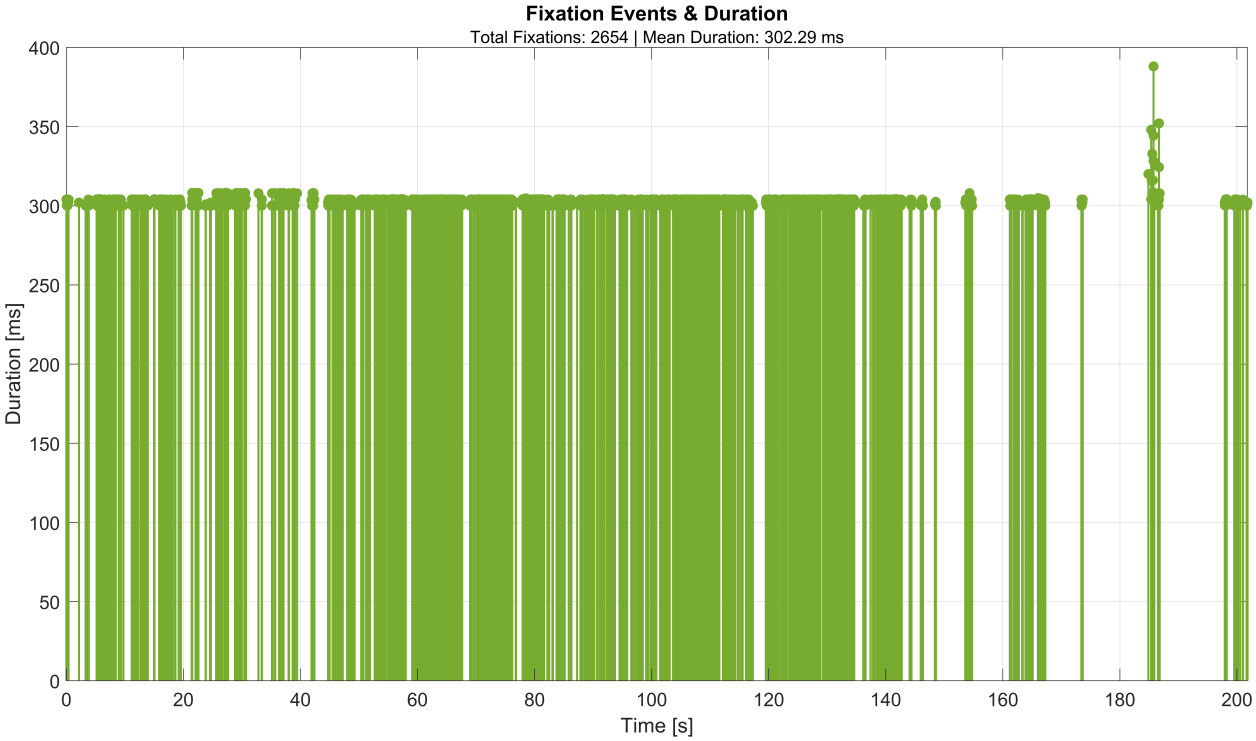


Figure 6.19: Fixation analysis (Non-Pilot).

6.3.3. ECG Results

Regarding the analysis of the pilot's cardiac activity, the following biological parameters were visualized:

- Signal visualization with R-Peak detection for each QRS complex.
- Evaluation of Beats Per Minute (BPM) over the temporal interval of the flight trial.
- Pilot Heart Rate (HR) over the same temporal interval.

Professional Pilot

As can be seen in Figures 6.20 and 6.22, the cardiac activity of the professional pilot remains consistently within the limits of a well-trained individual, with an average of 71 BPM. Notably, the low deviation of BPM from the mean value during the entire duration of the trial demonstrates the stability and reliability of the recorded values.

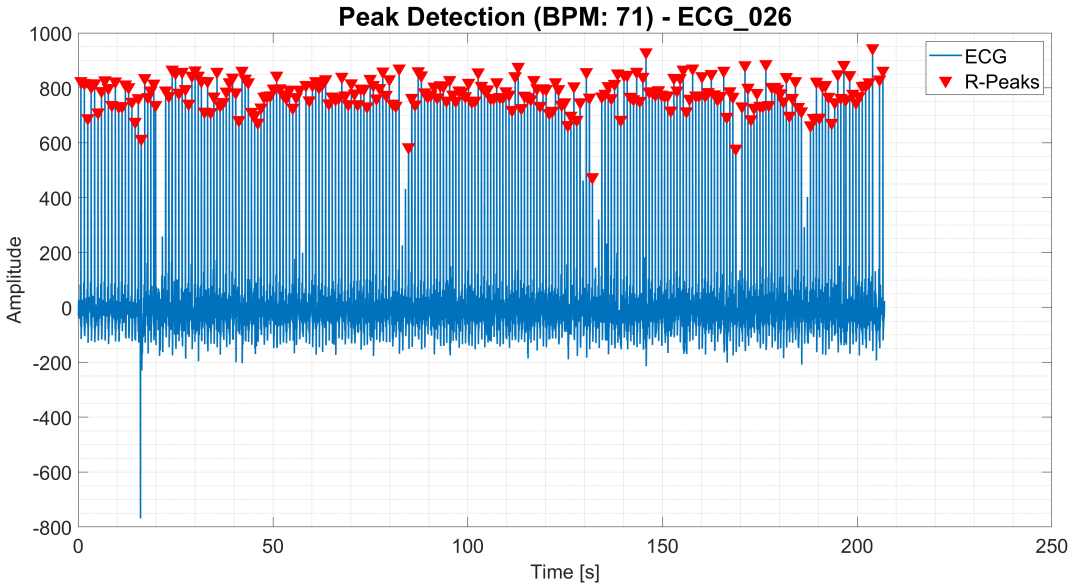


Figure 6.20: Identification of R-Peaks in the QRS complex during flight trials (Professional Pilot).

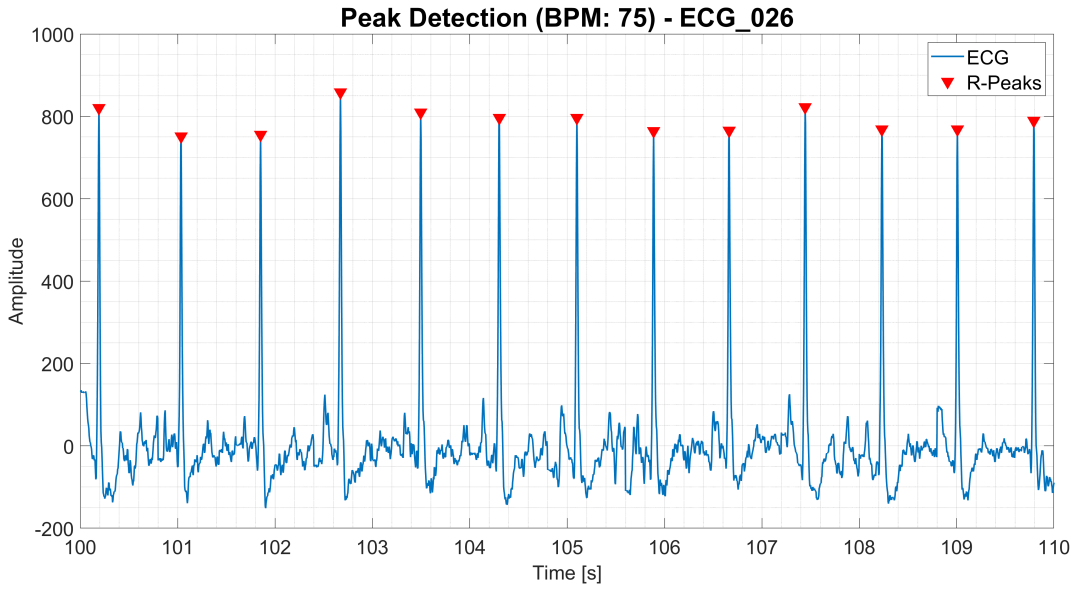


Figure 6.21: Zoom of the signal to highlight the QRS complex during flight trials over 10 seconds of time interval. Over such a short time interval, the BPM calculation is imprecise and not very indicative. (Professional Pilot).

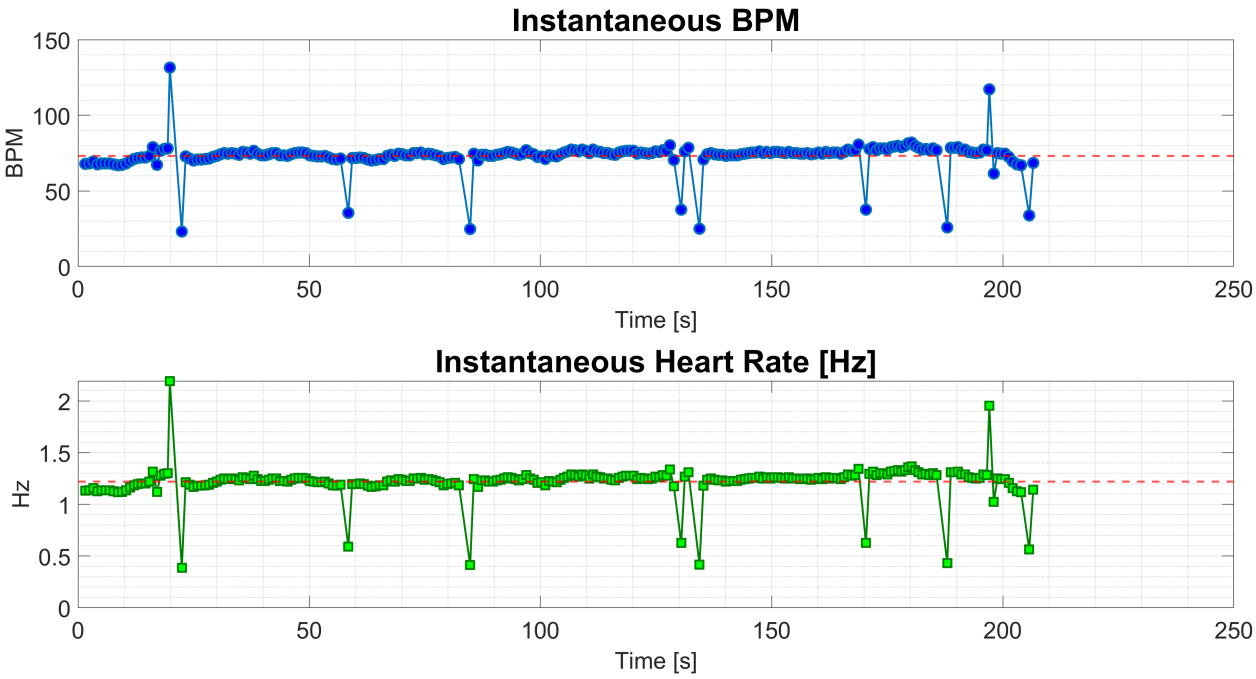


Figure 6.22: Identification of BPM and Heart Rate during flight trials (Professional Pilot). The red dashed line indicates the mean value calculated over the entire time interval.

Non-Pilot

A significant discrepancy exists in the signal amplitude data between the professional pilot (Figures 6.20 and 6.21) and the non-pilot (Figures 6.23 and 6.24). Specifically, the professional pilot's signal demonstrates a peak amplitude of approximately 1000, whereas the

non-pilot exhibits a peak amplitude roughly twice as large. This variance may be attributed to several confounding factors, including variations in thoracic electrode placement, age disparities between the subjects, and other unquantified physiological differences.

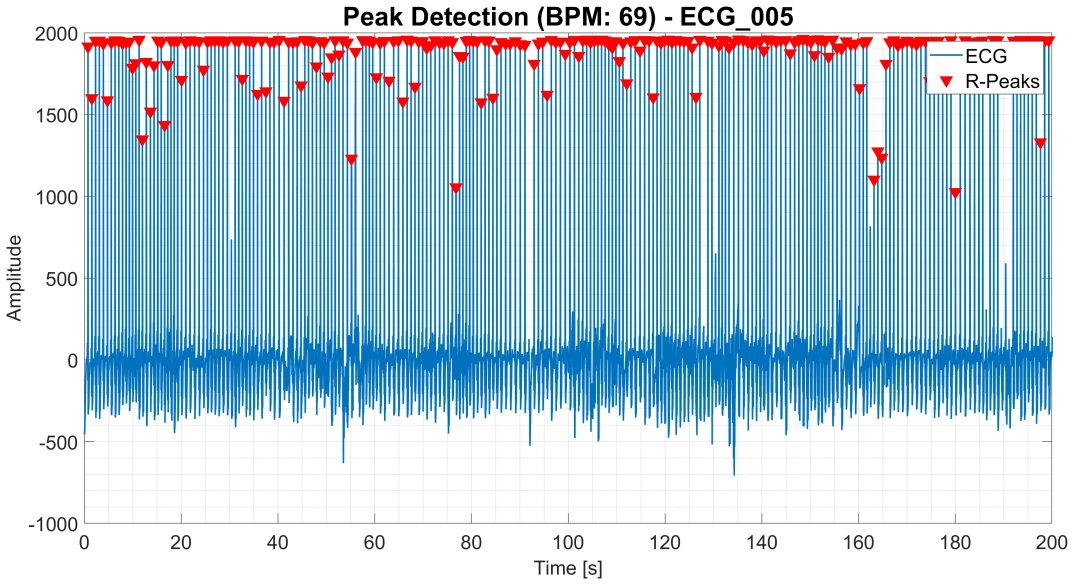


Figure 6.23: Identification of R-Peaks in the QRS complex during flight trials (Non-Pilot).

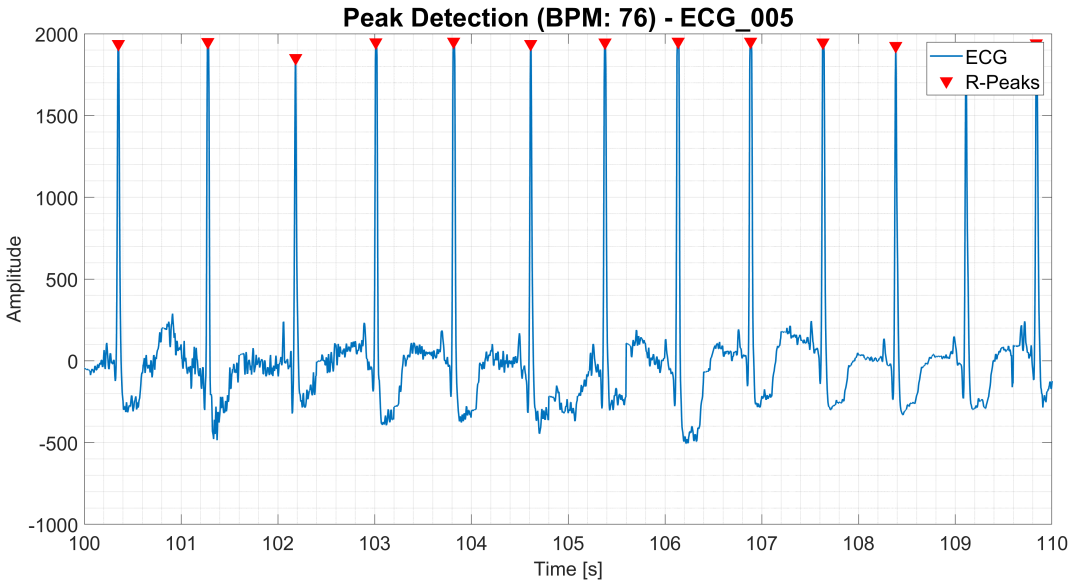


Figure 6.24: Zoom of the signal to highlight the QRS complex during flight trials over 10 seconds of time interval. Over such a short time interval, the BPM calculation is imprecise and not very indicative. (Non-Pilot).

As shown in Figure 6.25, the variation in Heart Rate for a Non-Pilot is significantly larger compared to that of a Professional Pilot (Figure 6.22) when performing the same task, indicating a higher physiological response and possible correlation with higher level of workload.

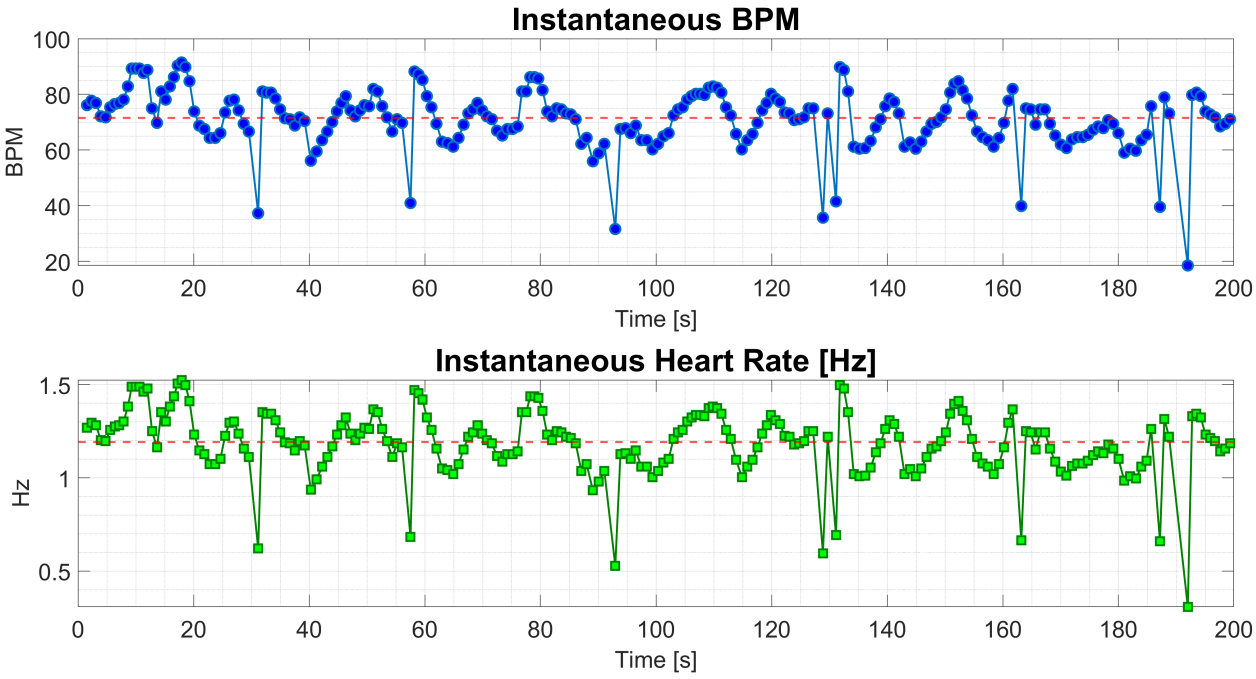
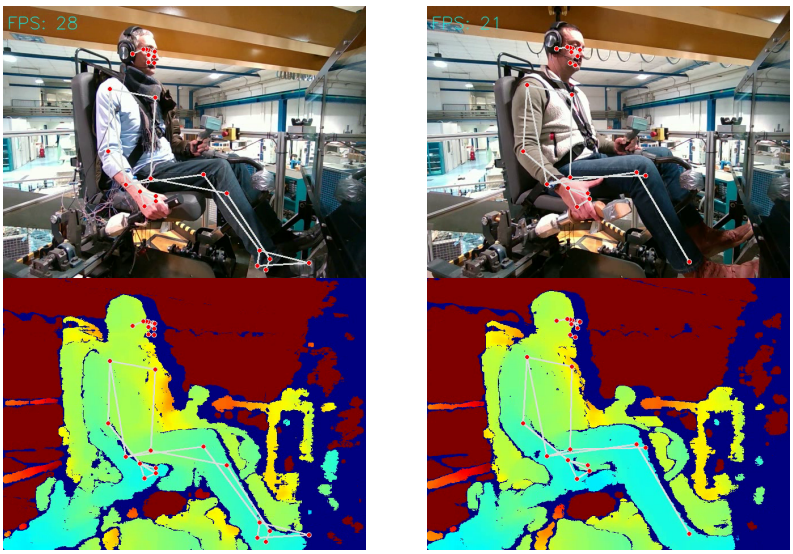


Figure 6.25: Identification of BPM and Heart Rate during flight trials (Non-Pilot). The red dashed line indicates the mean value calculated over the entire time interval.

6.3.4. Body Pose Results

The system was tested with various subjects of different anthropometric profiles, yielding robust tracking of the left forearm and arm during maneuvers requiring collective control operation.



(a) (b)

Figure 6.26: Comparison of body pose tracking for two pilots with significantly different body builds, highlighting the high tracking quality achievable in both cases.

Further analysis considered scenarios where tracking body keypoints is more complex due to the presence of heavier clothing. The following image demonstrates successful tracking performance even when clothing obscures body landmarks, making detection more challenging.

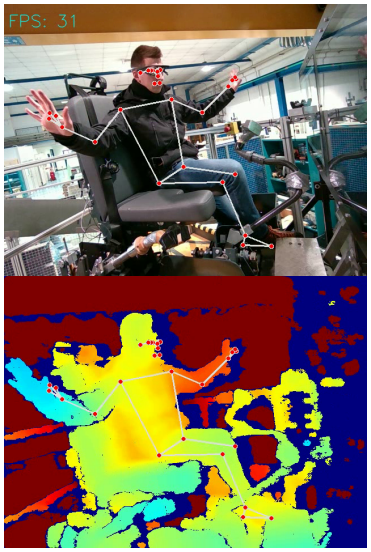


Figure 6.27: Tracking quality remains acceptable even in the presence of heavier clothing that complicates the identification of body keypoints.

6.3.5. OPT-IN Results

The installation of the OPT-IN sensor on the collective grip allowed for the acquisition of data regarding the pressure exerted by the pilot on the control during the flight trial.

It is noted that in this sensor, the voltage output value correlates with pressure. For each acquisition channel, 2 probes are installed to measure this variation. As with the data derived from the sEMG system, this evaluation focuses on the trend of the measured quantity—and by extension, the instantaneous voltage value—rather than its absolute quantitative value.

Also in this case, two well-defined zones can be highlighted during the trial:

1. **Active Flight Phase**: The phase in which maneuvers are effectively performed, where the voltage value is higher.
2. **Relaxation Phase**: The subsequent phase where the collective control is released, leading to a drastic reduction in voltage values.

Professional Pilot

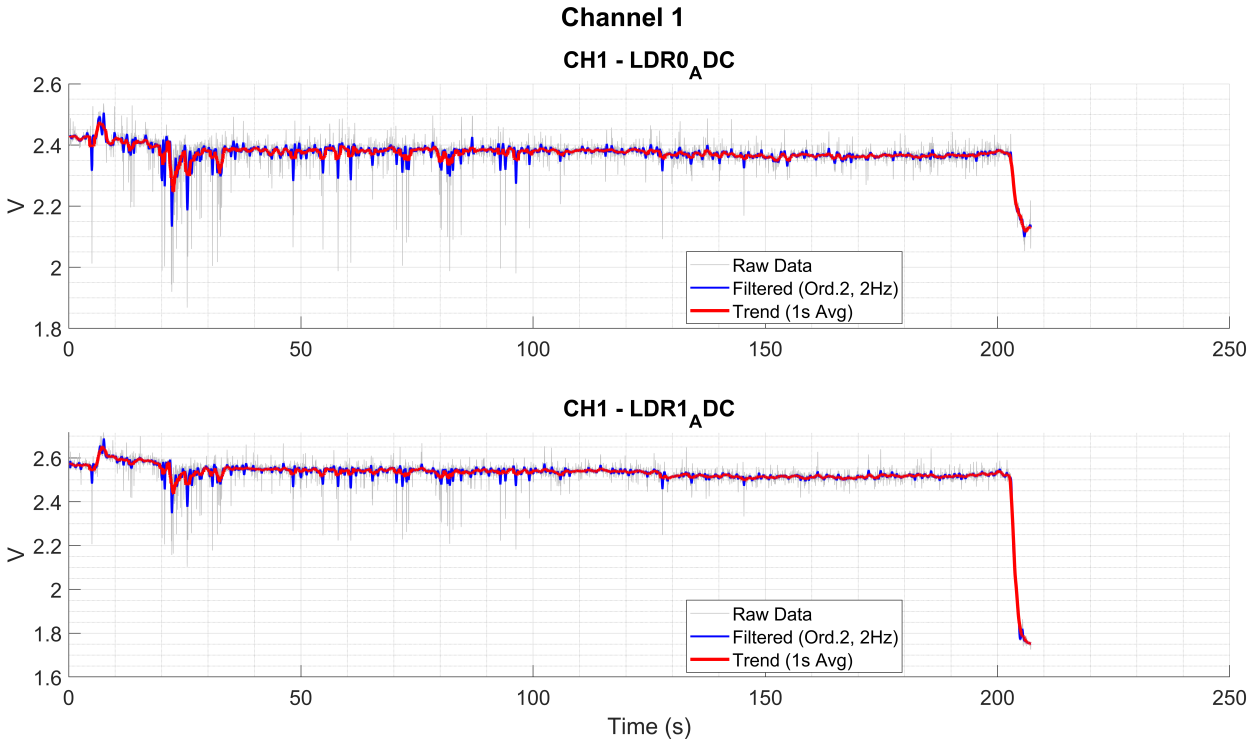


Figure 6.28: Identification of voltage values from Channel 1 of the OPT-IN sensor (Professional Pilot).

The inserted image is provided as an example and corresponds to the channel located on the lower part of the grip, where the pilot wraps their fingers around the collective lever.

Non-Pilot

A substantial difference compared to the professional pilot is observed: the pressure exerted by the non-pilot on the sensor is significantly higher on every OPT-IN channel, suggesting a "death grip" phenomenon typical of less experienced operators.

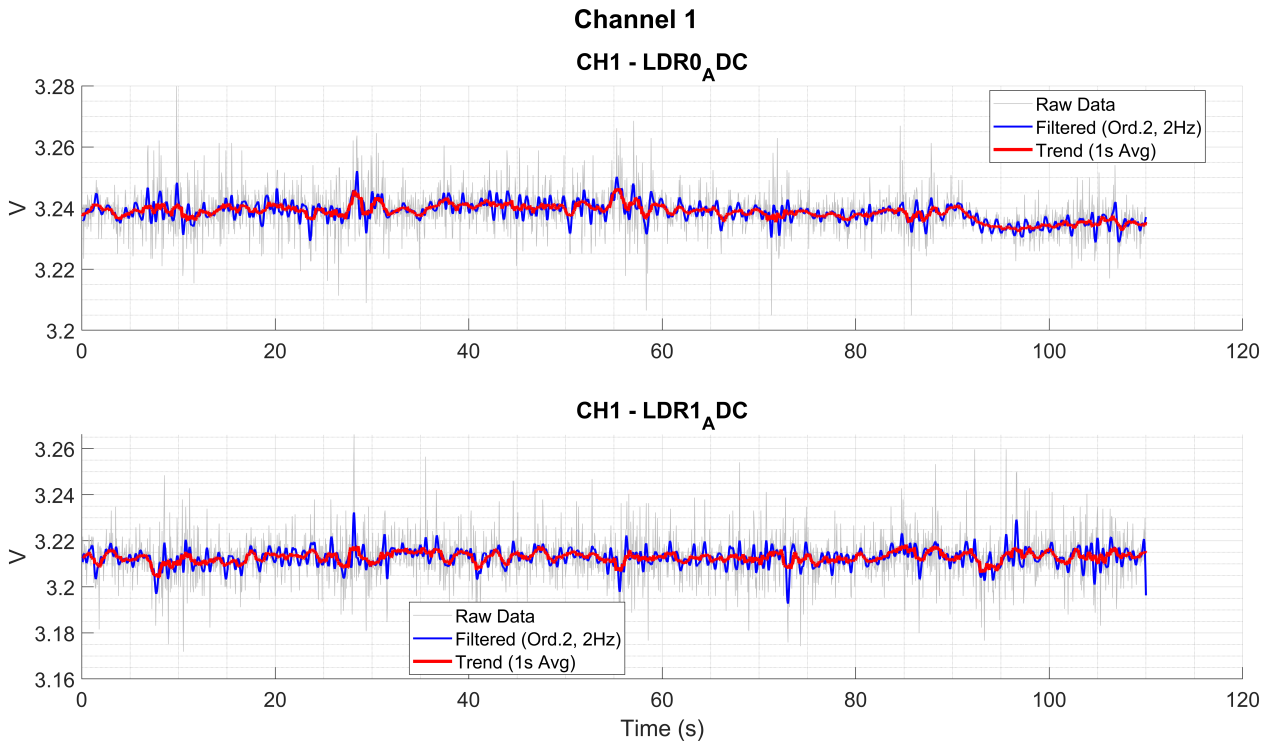


Figure 6.29: Identification of voltage values from Channel 1 of the OPT-IN sensor (Non-Pilot).

7 | Conclusions and future developments

7.1. Conclusions on System Integration

This chapter has detailed the successful deployment of the experimental setup, providing a concluding synthesis regarding both the mechanical integration of the hardware ecosystem and the development of the supporting software infrastructure. The primary objective — to equip the RPC Test Rig with a multi-modal sensor suite capable of recording physiological data and, at a later time, try to objectively assess pilot workload — was achieved through a distinct separation of hardware anchoring and software data management strategies.

7.1.1. Hardware Integration and Signal Integrity

The physical integration of the heterogeneous sensor suite (sEMG, Eye Tracking, ECG, Body Pose, and OPT-IN) onto the simulator platform was executed successfully. The mechanical design and placement strategies proved to be robust, satisfying two critical requirements:

- **Mechanical Stability:** Despite the dynamic nature of the simulator platform, the rigid mounting solutions and cable management strategies effectively mitigated mechanical interference. The data acquisition remained stable, minimizing susceptibility to excessive noise or motion artifacts typically induced by platform vibrations during high-gain maneuvers.
- **Ergonomics and Non-Intrusiveness:** The sensors were strategically positioned to minimize physical obstruction, ensuring that the pilot's range of motion and access to flight controls (especially the collective command) remained unhindered. This is vital for ensuring that the measured workload is a genuine result of the flight task rather than an artifact of the measurement equipment itself.

7.1.2. Software Infrastructure and Data Synchronization

The software architecture, constructed upon the MARSH communication protocol, established a robust foundation for the experiment. The integration facilitated precise temporal

alignment across all subsystems, a critical requirement for correlating physiological events (e.g., a transient spike in heart rate or pupil dilation) with specific flight dynamics events.

To manage the varying bandwidth and latency requirements of the different sensors, a hybrid data logging strategy was implemented:

- **Telemetry Logging (.tlog):** High-level telemetry from the Eye Tracking and Body Pose modules was encapsulated in custom MAVLink messages and logged directly into binary `.tlog` files via the central MARSH-Manager. This facilitated immediate post-flight inspection and synchronization validation.
- **Local Raw Data Storage:** To preserve signal fidelity and prevent network congestion, high-frequency raw data from the sEMG, ECG, and OPT-IN sensors were stored locally (either on onboard microSD cards or the pilot's dedicated PC).

7.1.3. Post-Processing Pipeline

Finally, the development of the MATLAB post-processing suite validated the entire data pipeline. Through the successful parsing, filtering, and visualization of the synchronized datasets, it was possible to confirm the signal quality. This workflow enables the extraction of key physiological features — such as Root Mean Square (RMS) for muscle activity or Heart Rate Variability (HRV) for cardiac response — laying the necessary foundation for the comprehensive analysis of the pilot's workload.

7.2. Future Developments

This final section outlines potential research avenues and technical refinements emerging from the work conducted in this thesis. These developments aim to enhance the robustness, accuracy, and usability of the physiological monitoring system.

7.2.1. Software Enhancements

A significant portion of future work will focus on developing additional software features to optimize data acquisition workflow and expand the dataset capabilities of the physiological sensor suite.

Advanced Eye Tracking Metrics

The current Eye Tracking implementation, leveraging Pupil Labs software, provides robust raw data. However, further processing algorithms are required to derive higher-order metrics:

- **Saccade Detection:** Implementing velocity-threshold or acceleration-threshold algorithms to distinctly classify saccadic events from smooth pursuit or fixation is crucial

for analyzing scanning strategies.

- **Dynamic Surface Mapping:** Improving the mapping of the gaze vector onto the virtual cockpit surfaces. A more precise definition of Areas of Interest (AOI) within the 3D virtual environment is necessary to automatically correlate gaze fixations with specific flight instruments (e.g., determining exactly when and for how long the pilot checks the torque indicator).

3D Body Pose Reconstruction

The current body tracking module effectively captures 2D keypoints in video coordinates, with depth approximated via the camera's laser sensor. To enable rigorous biomechanical analysis, future work must focus on a full 3D kinematic reconstruction. This involves calibrating the depth factor to map 2D pixel coordinates into 3D Euclidean space (x, y, z), allowing for the accurate measurement of real-world joint angles and limb displacements during control inputs.

Once this accurate 3D mapping is established, the resulting empirical measurements can be leveraged to validate and verify current and future multibody models designed to analyze pilot body dynamics during flight simulations. Furthermore, the concurrent recording of video data facilitates the identification of anomalous piloting techniques. This visual context is essential for interpreting atypical variations in the collected kinematic data, providing a clear rationale for outliers that would otherwise remain unexplained.

ECG and OPT-IN System Architecture

Given the architectural similarities between the ECG and OPT-IN modules (both based on microcontroller units), their future development paths are convergent. The primary areas for improvement include:

- **Real-Time Data Acquisition:** Upgrading the firmware to fully integrate with MARSH digital triggers for automated synchronization. Additionally, implementing a real-time data stream (via Serial/USB) to a host PC would allow for live monitoring of signal quality during the experiment, preventing data loss due to sensor detachment or noise.
- **Storage Reliability:** Currently, data is stored on local microSD cards. This medium has proven sensitive to power fluctuations, posing a risk of data corruption. A transition to direct PC logging via a robust wired interface (analogous to the sEMG setup) would mitigate this risk and streamline the file management process.
- **Structural Optimization of OPT-IN:** The current OPT-IN sensor housing is manufactured via Fused Deposition Modeling (FDM) 3D printing. This process introduces intrinsic anisotropy, making the part susceptible to failure under shear and bending

loads perpendicular to the print layers. Recent stress tests resulted in a structural failure at a stress concentration point (choke point) on the sensor.

7.2.2. Development of an Objective Workload Assessment System

The ultimate goal, enabled by the massive quantity of data collected by this multi-modal sensor ecosystem, is the development of a comprehensive system for the *objective evaluation of pilot Workload*.

By fusing data from muscular activity, ocular behavior, cardiac response, and kinematic performance, it is possible to train multi-variable estimators (potentially leveraging Machine Learning techniques) to output a real-time workload index. Furthermore, leveraging the modularity of the FRAME-Lab platform, this assessment system can be validated across a wide range of simulated rotorcraft dynamics, ensuring its robustness and applicability to diverse flight scenarios.

7.2.3. Proposed Experimental Protocol for Workload Validation

To validate the objective workload assessment system, a rigorous flight test campaign has been defined. This protocol is designed to correlate the physiological telemetry acquired by the multi-modal sensor suite with subjective *Bedford Workload Scale* ratings across a spectrum of task difficulties. The validation framework relies on a high-fidelity 6-DOF flight dynamics model to ensure realistic handling qualities and structural response.

Workload Modulation Strategy

Cognitive demand is modulated through two primary vectors: maneuver complexity and environmental degradation. The experimental design incorporates three distinct difficulty levels based on visual cue availability:

- **Low Difficulty (VMC):** Full visibility of the horizon and ground references, representing standard operations.
- **Medium Difficulty (Degraded):** The horizon is obscured, forcing the pilot to rely on ground tracking for attitude maintenance.
- **High Difficulty (IMC/DVE):** Both the horizon and 50% of ground markers are obscured. This condition simulates dense fog, maximizing the cognitive effort required for spatial orientation and path control.

Mission Task Elements (MTEs)

The flight profile consists of five Specific Test Objects (STOs) derived from the ADS-33E-PRF [64] standard chose by the FRAME Lab personel [60]. These maneuvers are selected to stress different axes of control and induce varying levels of task saturation. A summary of the defined experimental tasks is provided in Table 7.1.

Table 7.1: Summary of Specific Test Objects (STOs) for Workload Validation

ID	Maneuver	Operational Objective and Workload Driver
STO 1	Cruise	**Baseline Assessment:** Maintain steady-state parameters (300 ft AGL, 60 KIAS) to establish a physiological baseline for low-demand tasks.
STO 2	Hover	**Precision Station Keeping:** Transition from translation to a stabilized hover. Evaluates multi-axis coordination and attention distribution under wind disturbances.
STO 3	Vertical Maneuver	**RPC Triggering:** Rapid unmask/remask (15 ft $\leftrightarrow$ 40 ft). Specifically designed to evaluate heave axis controllability and trigger potential rotorcraft-pilot couplings via collective inputs.
STO 4	Accel / Decel	**Aggressive Handling:** Rapid energy management between hover and 50 KIAS. Assesses pitch-heave coupling and the pilot's ability to manage aggressive attitude changes.
STO 5	Depart / Abort	**Decision Making:** Initiation of departure followed by a rapid abort and precision stop. Induces high workload through the requirement for immediate corrective action and precise energy dissipation.

For each STO, performance is graded against the *Desired* and *Adequate* tolerances specified in ADS-33E. The synchronization of these performance metrics with physiological data points (e.g., heart rate variability peaks, gaze entropy, and muscle activation patterns) will enable the training of the objective workload estimation algorithm described in the future developments.

Bibliography

[1] ADVISORY GROUP FOR AEROSPACE RESEARCH & DEVELOPMENT. Advances in Rotorcraft Technology. In *AGARD CONFERENCE PROCEEDINGS 592*. North Atlantic Treaty Organization, 5 1996. ISBN 92-836-0038-X.

[2] Analog Devices. ad8232 - data sheet. Technical report, Analog Devices, 2025. URL `www.analog.com`.

[3] Anitha S Prasad and Kavanashree N. ECG MONITORING SYSTEM USING AD8232 SENSOR. In *Fourth International Conference on Communication and Electronics Systems*. [IEEE], 2019. ISBN 9781728112619.

[4] ARISTOTEL Project Board. Final Publishable Summary ARISTOTEL Project. Technical report, Technische Universiteit Delft, Politecncico di Milano and others, 2024. URL `http://www.aristotel-project.eu/`.

[5] E. Bachelder, B. Aponso, and T. Berger. A Theoretical Basis for Predicting Pilot Performance, Workload and Handling Qualities. In *AIAA SciTech Forum and Exposition, 2023*. American Institute of Aeronautics and Astronautics Inc, AIAA, 2023. ISBN 9781624106996. doi: 10.2514/6.2023-1369.

[6] M. Barbero, R. Merletti, and A. Rainoldi. *Atlas of Muscle Innervation Zones*. Springer Milan, 2012. doi: 10.1007/978-88-470-2463-2.

[7] P. Besson, C. Bourdin, L. Bringoux, E. Dousset, C. Maïano, T. Marqueste, D. R. Mestre, S. Gaetan, J. P. Baudry, and J. L. Vercher. Effectiveness of physiological and psychological features to estimate helicopter pilots' workload: A bayesian network approach. *IEEE Transactions on Intelligent Transportation Systems*, 14(4):1872–1881, 12 2013. ISSN 15249050. doi: 10.1109/TITS.2013.2269679.

[8] R. Bradley, C. A. Macdonald, and T. W. Buggy. Quantification and prediction of pilot workload in the helicopter/ship dynamic interface. *Proceedings of the Institution of Mechanical Engineers, Part G: Journal of Aerospace Engineering*, 219(5):429–443, 10 2005. ISSN 09544100. doi: 10.1243/095441005X33376.

[9] M. Bravo-Zanoguera, D. Cuevas-González, J. P. García-Vázquez, R. L. Avitia, and M. A. Reyna. Portable ECG System Design Using the AD8232 Microchip and Open-Source Platform. *MDPI*, page 49, 1 2020. doi: 10.3390/ecsa-6-06584.

[10] B. T. Carter and S. G. Luke. Best practices in eye tracking research. *International Journal of Psychophysiology*, 155:49–62, 9 2020. ISSN 18727697. doi: 10.1016/j.ijpsycho.2020.05.010.

[11] S. M. Casner and B. F. Gore. Measuring and Evaluating Workload: A Primer. Technical report, NASA, 2010. URL `http://www.sti.nasa.gov`.

[12] Davide Pio Loco Zanet. *Helicopter sensorized inceptors for pilot workload evaluation.* PhD thesis, Politecnico di Milano, 2023.

[13] De Franceschi Paolo. *Experimental Evaluation of Novel Control Inceptor Architectures for Rotorcraft-Pilot Coupling Mitigation.* PhD thesis, Politecnico di Milano, 12 2025.

[14] C. J. De Luca, L. Donald Gilmore, M. Kuznetsov, and S. H. Roy. Filtering the surface EMG signal: Movement artifact and baseline noise contamination. *Journal of Biomechanics*, 43(8):1573–1579, 5 2010. ISSN 00219290. doi: 10.1016/j.jbiomech.2010.01.027.

[15] Elena Rankova. *Exploring Pilot Workload Scenarios via Eye-Tracking: An Attempt at Inducing and Identifying Attentional Tunneling in the Cockpit.* PhD thesis, Università di Trento, 2023.

[16] K. Ellis and T. Schnell. Eye Tracking Metrics for Workload Estimation in flight Deck Operation. Technical report, OperatorPerformance Laboratory, University ofIowa, 2010.

[17] C. Feng, X. Wanyan, K. Yang, D. Zhuang, and X. Wu. A comprehensive prediction and evaluation method of pilot workload. In *Technology and Health Care*, volume 26, pages S65–S78. IOS Press, 5 2018. doi: 10.3233/THC-174201.

[18] FRAME-Lab Polimi. RPC Test Rig Specification, 2023. URL `https://gitlab.polimi.it/DAER/frame-sim/frame-wiki/-/wikis/home`.

[19] S. Gaetan, E. Dousset, T. Marqueste, L. Bringoux, C. Bourdin, J.-L. Vercher, and P. Besson. Cognitive Workload and Psychophysiological Parameters During Multitask Activity in He-licopter Pilots. *Aerospace Medicine and Human Performance*, 86(12), 2015. doi: 10.3357/AMHP.4228.2015{\"{i}}. URL `https://hal.science/hal-01414096v1`.

[20] P. Garbo, A. Zanoni, and G. Quaranta. An optical pressure measurement system for control inceptors to evaluate pilots' workload. Technical report, Dipartimento di Scienze e Tecnologie Aerospaziali, Politecnico di Milano, 2022. URL `https://openaccess.cms-conferences.org/#/publications/book/978-1-7923-8987-0`.

[21] M. Gennaretti, M. M. Colella, J. Serafini, R. Tre, B. Dang Vu, P. Masarati, G. Quaranta, V. M. Politecnico, D. Milano, M. Jump, M. Jones, L. Lu, A. Ionita, I. Fuiorea, M. Mihaila-Andres, and S. Straero. ANATOMY, MODELLING AND PREDICTION OF AEROSERVOELASTIC ROTORCRAFT-PILOT-COUPLING. Technical report,

University Roma Tre, Dept. of Engineering, Politecnico di Milano, Dept. of Aerospace Engineering, University of Liverpool, School of Engineering, STRAERO, Bucharest, 2013. URL `http://www.mbdyn.org/`.

[22] T. C. Hankins, M. D. And, and G. F. Wilson. A Comparison of Heart Rate, Eye Activity, EEG and Subjective Measures of Pilot Mental Workload During Flight. Technical report, Aerospace Medical Association, 1998. URL `https://asma.kglmeridian.com/`.

[23] K. Holmqvist, M. Nyström, R. Andersson, R. Dewhurst, H. Jarodzka, and J. van de Weijer. *Eye Tracking 2.* Oxford University Press, 2011. ISBN 978-0-19969708-3.

[24] Intel Corporation. Intel RealSense SDK 2.0, 2025. URL `https://github.com/IntelRealSense/librealsense`.

[25] Intel Corporation. RealSense Product Family D400 Series. Technical report, Intel Corporation, 2025.

[26] M. Jones, M. Alexander, M. Höfinger, M. Barnett, P. Comeau, and A. Gubbels. In-flight test campaign to validate PIO detection and assessment tools. *Aerospace*, 7(9), 9 2020. ISSN 22264310. doi: 10.3390/AEROSPACE7090136.

[27] Joost Venrooij, David A. Abbink, Mark Mulder, Marinus M. van Paassen, and Max Mulder. *Biodynamic feedthrough is task dependent.* I E E E, 2010. ISBN 9781424465880.

[28] D. H. Klyde, D. T. McRuer, and T. T. Myers. Pilot-induced oscillation analysis and prediction with actuator rate limiting. *Journal of Guidance, Control, and Dynamics*, 20(1):81–89, 1997. ISSN 07315090. doi: 10.2514/2.3998.

[29] A. Kopyt. Helicopter pilot's modeling including the stress factor. Technical report, Warsaw University of Technology, 2015.

[30] A. R. Kyle, B. Rouser, R. C. Paul, and K. A. Jurewicz. Quantifying Pilot Performance and Mental Workload in Modern Aviation Systems: A Scoping Literature Review. *Aerospace*, 12(7), 7 2025. ISSN 22264310. doi: 10.3390/aerospace12070626.

[31] D. Lee, C. Park, S. Chi, H. Yoon, and J. Kim. Markerless Human Body Pose Estimation from Consumer Depth Cameras for Simulator. In *12th International Conference on Ubiquitous Robots and Ambient Intelligence*, 10 2015.

[32] W.-C. Li, F.-C. Chiu, and K.-J. Wu. The Evaluation of Pilots Performance and Mental Workload by Eye Movement. Technical report, 2012.

[33] W. C. Li, C. S. Yu, M. Greaves, and G. Braithwaite. How Cockpit Design Impacts Pilots' Attention Distribution and Perceived Workload during Aiming a Stationary Target. In *Procedia Manufacturing*, volume 3, pages 5663–5669. Elsevier B.V., 2015. doi: 10.1016/j.promfg.2015.07.781.

[34] W.-C. Li, J. J. H. Lin, G. Braithwaite, and M. Greaves. The Development of Eye Tracking in Aviation (ETA) Technique to Investigate Pilot's Cognitive Processes of Attention and Decision-making. 2016.

[35] Lukasiewicz Marek Slawomir and Soldan Thomas. Pupil Eye Tracker, 2025. URL `https://github.com/marsh-sim/sim-nodes/blob/main/pupil_eye_tracker.py`.

[36] Lukasiewicz Marek Slawomir and Soldan Thomas. realsense-pose-detector, 2025. URL `https://github.com/marsh-sim/realsense-pose-detector`.

[37] G. Luzzani, I. Buraioli, D. Demarchi, and G. Guglieri. A review of physiological measures for mental workload assessment in aviation. *Aeronautical Journal*, 128(1323): 928–949, 5 2024. ISSN 20596464. doi: 10.1017/aer.2023.101.

[38] LWT3. Quick Start Raw Power. Technical report, LWT3 srl, 2025.

[39] D. Marchesoli. Comprehensive Analysis of Pilot-Vehicle Interactions. Technical report, Politecnico di Milano, 2024.

[40] Marek S. Lukasiewicz and Dipartimento di Scienze e Tecnologie Aerospaziali (DAER - PoliMi). MARSH documentation, 2023. URL `https://marsh-sim.github.io/`.

[41] T. Mehling, O. Halbe, M. Hajek, and M. Vrdoljak. Visual and Control Augmentation Techniques for Pilot Assistance During Helicopter Shipboard Recovery. Technical report, Technical University of Munich, University of Zagreb, 2021.

[42] Mun Wai Lee and Ram Nevatia. Body Part Detection for Human Pose Estimation and Tracking. Technical report, Institute for Robotics and Intelligent Systems University of Southern California, 2007.

[43] V. Muscarello, P. Masarati, and G. Quaranta. COLLECTIVE BOUNCE PROBLEMS IN TILTROTORS. Technical report, Department of Aerospace Science and Technology Politecnico di Milano, 2016. URL `http://ing.dk/artikel/`.

[44] V. Muscarello, A. Zanoni, and G. Quaranta. Impact of Design and Operational Parameters on Helicopter Vertical Bounce. *Journal of the American Helicopter Society*, 68(3), 7 2023. ISSN 00028711. doi: 10.4050/JAHS.68.032009.

[45] D. Nonnenmacher and H. M. Kim. Evaluation of an advanced slung load control system for piloted cargo operations. *CEAS Aeronautical Journal*, 11(4):897–915, 12 2020. ISSN 18695590. doi: 10.1007/s13272-020-00458-7.

[46] Olivari Mario, Venrooij Joost, Nieuwenhuizen Frank M., Pollini Lorenzo, and Buelthoff Heinrich. Identifying Time-Varying Pilot Responses: a Regularized Recursive Least-Squares. In *AIAA Modeling and Simulation Technologies Conference*, Reston, Virginia,

1 2016. American Institute of Aeronautics and Astronautics. ISBN 978-1-62410-387-2. doi: 10.2514/6.2016-1182.

[47] G. D. Padfield. *Helicopter flight dynamics : including a treatment of tiltrotor aircraft*. John Wiley & Sons, Inc., 2018. ISBN 9781119401025.

[48] T. Pan, H. Wang, H. Si, Y. Li, and L. Shang. Identification of pilots' fatigue status based on electrocardiogram signals. *Sensors*, 21(9), 5 2021. ISSN 14248220. doi: 10.3390/s21093003.

[49] Patrick Martin and Paul Calhoun. Objective Measures of Pilot Workload. Technical report, Air Force Test Center, Operator Performance Laboratory University of Iowa, 2019. URL `https://www.researchgate.net/publication/337901538`.

[50] M. Pavel and G. D. Padfield. Understanding the peculiarities of rotorcraft, pilot, couplings CITATIONS SEE PROFILE. *Delft University of Technology, The University of Liverpool*, 1 2008. URL `https://www.researchgate.net/publication/27353904`.

[51] M. D. Pavel, M. Jump, B. Dang-Vu, P. Masarati, M. Gennaretti, A. Ionita, L. Zaichik, H. Smaili, G. Quaranta, D. Yilmaz, M. Jones, J. Serafini, and J. Malecki. Adverse rotorcraft pilot couplings - Past, present and future challenges. *Progress in Aerospace Sciences*, 62:1–51, 10 2013. ISSN 03760421. doi: 10.1016/j.paerosci.2013.04.003.

[52] Po-Chi Huang and Shyh-Kang Jeng. *Human Body Pose Recognition from a Single-View Depth Camera*. IEEE, 2012. ISBN 9781467317146.

[53] Pupil Labs GmbH. Pupil Core Documentation, 2024. URL `https://docs.pupil-labs.com/core/`.

[54] Quaranta Giuseppe, Masarati Pierangelo, Serafini Jacopo, and Gennaretti Massimo. AEROELASTIC ROTORCRAFT-PILOT COUPLINGS: PROBLEMS AND METHODS. *Politecnico di Milano Dipartimento Scienze e Tecnologie Aerospaziali, Universit'a degli Studi Roma Tre Dipartimento di Ingegneria*, page 12, 2016.

[55] A. H. Roscoe and G. A. Ellis. A Subjective Rating Scale for Assessing Pilot Workload in Flight: A Decade of Practical Use. Technical report, Royal Aerospace Establishment, 1990.

[56] J. R. S. Scarpari, M. W. Ribeiro, C. S. Deolindo, M. A. A. Aratanha, D. de Andrade, C. H. Q. Forster, J. M. P. Figueira, F. L. S. Corrêa, S. S. Lacerda, B. S. Machado, E. Amaro Júnior, J. R. Sato, E. H. Kozasa, and R. G. Annes da Silva. Quantitative assessment of pilot-endured workloads during helicopter flying emergencies: an analysis of physiological parameters during an autorotation. *Scientific Reports*, 11(1), 12 2021. ISSN 20452322. doi: 10.1038/s41598-021-96773-y.

[57] S. Shao, Q. Zhou, and Z. Liu. A new assessment method of the pilot stress using ECG

signals during complex special flight operation. *IEEE Access*, 7:185360–185368, 2019. ISSN 21693536. doi: 10.1109/ACCESS.2019.2959626.

[58] Shian-Ru Ke, Jenq-Neng Hwang, Kung-Ming Lan, and Shen-Zheng Wang. View-Invariant 3D Human Body Pose Reconstruction using a Monocular Video Camera. In *Department of Electrical Engineering University of Washington, Service Systems Technology Center Industrial Technology Research Institute (ITRI) Hsinchu, Taiwan*. IEEE, 2011. ISBN 9781457717079.

[59] I. Škvareková, P. Pecho, V. Ažaltovic, and B. Kandera. Number of saccades and fixation duration as indicators of pilot. In *Transportation Research Procedia*, volume 51, pages 67–74. Elsevier B.V., 2020. doi: 10.1016/j.trpro.2020.11.009.

[60] Soldan Thomas and Abbasi Ahmad. FLIGHT TEST PLANNING DOCUMENT - WORKLOAD EVALUATION. Technical report, FRAME Lab Politecnico di Milano, 1 2026.

[61] Srijan Adhikari, Rajesh Shan, and Umesh Pokharel. EMG controlled Prosthetic Hand. 2015.

[62] STMicroelectronics NV. UM1724 User manual. Technical report, STMicroelectronics, 2025. URL `www.st.com`.

[63] Sujoy Ghosh Hajra, Pengcheng Xi, and Andrew Law. A comparison of ECG and EEG metrics for in-flight monitoring of helicopter pilot workload. In *IEEE International Conference on Systems, Man, and Cybernetics*. IEEE, 2020. ISBN 9781728185262.

[64] Us Army Aviation and Missile Command Aviation Engineering Directorate. AERONAUTICAL DESIGN STANDARD PERFORMANCE SPECIFICATION HANDLING QUALITIES REQUIREMENTS FOR MILITARY ROTORCRAFT (ADS33). Technical report, United States Army Aviation and Missile Comand, Aviation Engineering Directorate, 2000.

[65] Z. Wang, S. Liu, X. Wanyan, Y. Dang, X. Chen, and X. Zhang. Pilot workload measurement model based on task complexity analysis. *International Journal of Industrial Ergonomics*, 104, 11 2024. ISSN 18728219. doi: 10.1016/j.ergon.2024.103637.

[66] A. Zanoni, M. Zago, R. Paolini, G. Quaranta, M. Galli, and P. Masarati. On task dependence of helicopter pilot biodynamic feedthrough and neuromuscular admittance: An experimental and numerical study. *IEEE Transactions on Human-Machine Systems*, 51(5):421–431, 10 2021. ISSN 21682305. doi: 10.1109/THMS.2020.3044971.

[67] A. Zanoni, D. Marchesoli, C. Talamo, P. Masarati, F. Colombo, S. Kemp, and E. Fosco. Experimental test-bed for the identification of biodynamic feedthrough of helicopter-

pilot systems. Technical report, Politecnico di Milano - Dipartimento di Scienze e Tecnologie Aerospaziali, Leonardo Helicopters Division, 2022.

[68] A. Zanoni, P. Garbo, P. Masarati, and G. Quaranta. Frustrated Total Internal Reflection Measurement System for Pilot Inceptor Grip Pressure. *Sensors*, 23(14), 7 2023. ISSN 14248220. doi: 10.3390/s23146308.

[69] Zanoni Andrea, Lukasiewicz Marek S, Masarati Pierangelo, and Zilletti Michele. SIMULATOR EXPERIMENTS FOR AEROELASTIC ROTORCRAFT-PILOT COUPLINGS. In *Department of Aerospace Science and Technology, Politecnico di Milano Milano, Leonardo Helicopters Division*. Politecnico di Milano, 2025.

[70] W. Zhu, C. Zhang, C. Liu, F. Xu, C. Jiang, and W. Cao. Assessment of Pilot Mental Workload Based on Physiological Signals: A Real Helicopter Cross-country Flight Study. In *Proceedings of 2023 IEEE 5th International Conference on Civil Aviation Safety and Information Technology, ICCASIT 2023*, pages 638–643. Institute of Electrical and Electronics Engineers Inc., 2023. ISBN 9798350310603. doi: 10.1109/ICCASIT58768.2023.10351548.

A | Appendix A - RPC Test Rig

This appendix details the hardware and software architecture of the RPC Test Rig located in the FRAME-Lab of the Department of Aerospace Science and Technology (DAER), a highly specialized experimental platform designed for the biodynamic characterization of pilots in the context of Rotorcraft-Pilot Couplings (RPC) and Biodynamic Feedthrough (BDFT). The information presented herein is derived from the DAER Frame Wiki, the doctoral thesis of Davide Marchesoli [18, 39], and recent experimental campaigns presented at the European Rotorcraft Forum [67, 69].

A.1. Overview and Purpose

The RPC Test Rig constitutes a specialized experimental platform engineered for the biodynamic characterization of pilots across various cockpit configurations. Unlike conventional flight simulators primarily focused on procedural training, this testbed is designed to operate within a specific, high-frequency bandwidth (up to 7.5 Hz), which is critical for investigating Pilot-Assisted Oscillations (PAO) and BDFT phenomena. The design philosophy of the rig is predicated on the accurate replication of the geometric and force-feel characteristics of actual rotorcraft cockpits. Two geometric parameters of paramount importance are rigorously maintained: the Mean Seat Reference Point (MSRP) and the Finger Reference Point (FRP), ensuring the faithful reproduction of pilot limb positioning during testing.



(a) (b)

Figure A.1: Testbed configuration: Motion Platform (Fig A.1a), Cockpit Mock-up and Instrumentation (Fig A.1b).

A.2. Motion Platform System (MPS)

Motion cues are provided by the *Bosch Rexroth eMotion* 1500 6-DOF Motion Platform (currently supported by Van Halteren Technologies, VHT). Its selection was driven by the stringent requirement to achieve substantial acceleration performance in the 0–7.5 Hz frequency range, particularly along the heave axis, which is essential for RPC investigations.

A.2.1. Dynamic Capabilities

The platform's performance metrics meet or exceed the specified requirements for BDFT identification tests. The system is capable of supporting a maximum payload of 1500 kg and delivering acceleration inputs in excess of $10\,\mathrm{m/s^2}$ within the frequency band of interest. Key range of motion and acceleration performance data are summarized in Tables A.1 and A.2.

Table A.1: eMotion 1500 Motion Platform Range of Motion

Direction	Desired	Minimum	Maximum	Peak-to-Peak
Surge	0.2 m	−0.499 m	0.628 m	1.127 m
Sway	0.2 m	−0.506 m	0.506 m	1.012 m
Heave	0.5 m	−0.383 m	0.372 m	0.755 m
Roll	25°	−24.01°	24.01°	48.02°
Pitch	25°	−25.05°	28.02°	53.07°
Yaw	25°	−27.25°	27.25°	54.5°

Table A.2: eMotion 1500 Motion Platform Acceleration Capabilities

Direction	Acceleration	Direction	Angular Acceleration
Surge	$\pm 7.000\,\mathrm{m/s^2}$	Roll	$\pm 250°/\mathrm{s^2}$
Sway	$\pm 7.000\,\mathrm{m/s^2}$	Pitch	$\pm 250°/\mathrm{s^2}$
Heave	$\pm 10.000\,\mathrm{m/s^2}$	Yaw	$\pm 250°/\mathrm{s^2}$

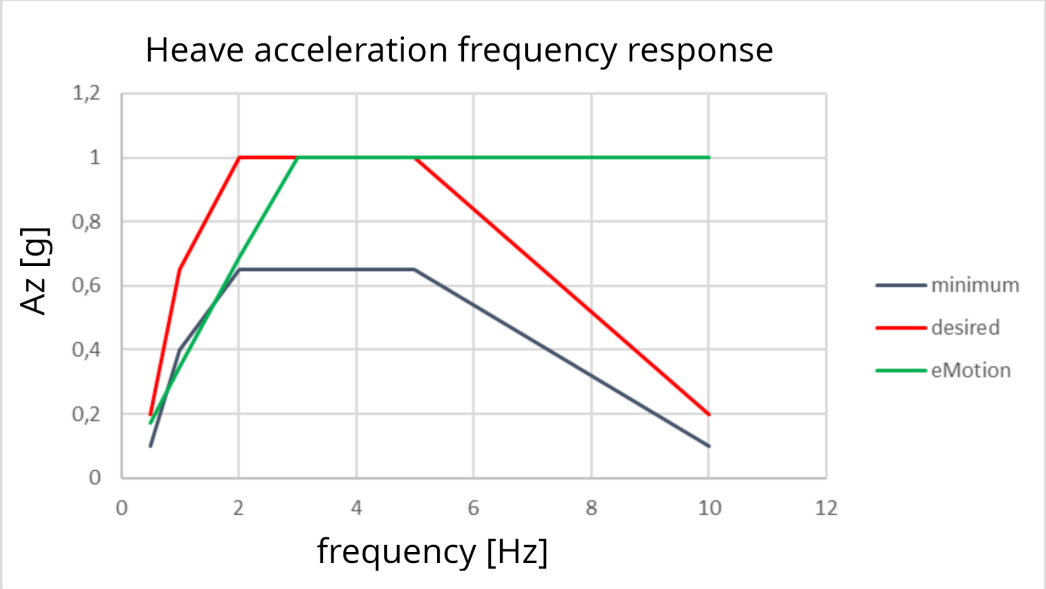


Figure A.2: Dynamic response performance of the eMotion 1500 Motion Platform System compared with the heave acceleration requirements for RPC testing.

A.2.2. Usage Modes

The Motion Platform System (MPS) supports two primary operational modes, managed via the `Hypcos` control software:

1. **Open Loop (Manual):** Utilized primarily during BDFT identification tests. Predefined time histories of platform displacement—typically pseudo-random waveforms with a flat Power Spectral Density (PSD) in the 1–7.5 Hz band—are generated and fed directly to the `Hypcos` low-level control, operating in a Real-Time Linux environment.
2. **Closed Loop (Normal):** Enables real-time control via UDP packets, allowing the platform to provide motion cueing based on simulated flight conditions (e.g., flight mechanics or aeroelastic models). This mode is integrated into the comprehensive simulation architecture described in Section A.6.

A.3. Structural Components

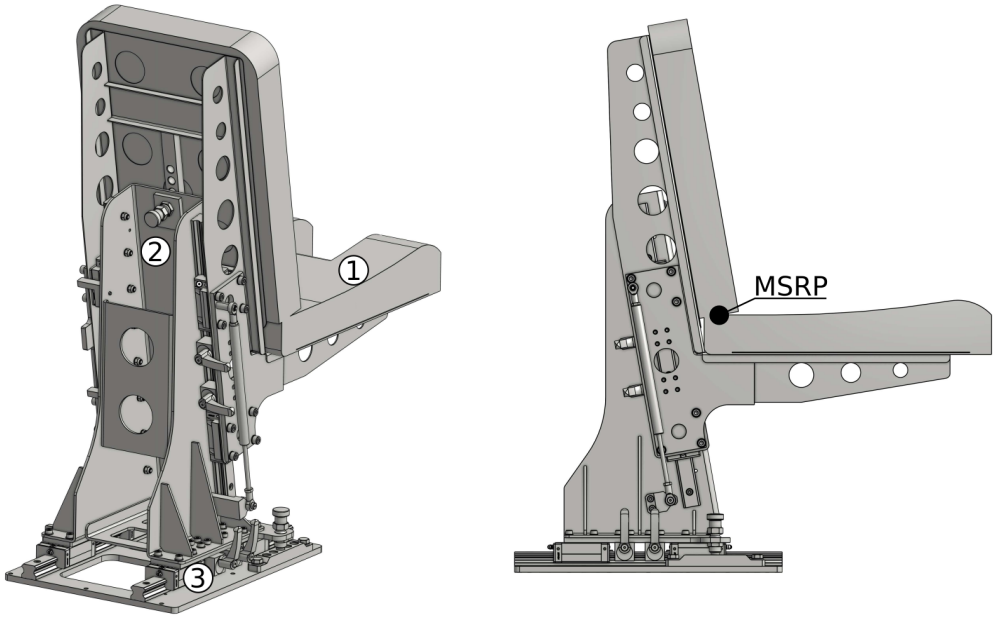
A.3.1. Support Structure

The primary frame connects the cockpit mock-up to the motion platform. It is a stainless steel welded structure composed of square tubes ($50 \times 50 \times 3\,\text{mm}$). Structural integrity was validated through static analysis, yielding a maximum Von Mises equivalent stress of 31.6 MPa under worst-case loading scenarios. Fatigue analysis indicated an effectively infinite operational life ($N_{cr} = 9.2 \times 10^{11}$ cycles). Experimental Resonance Assessment Profile (RAP) tests confirmed the absence of undesired structural eigenmodes in the critical 0–10 Hz frequency band.

A.3.2. Pilot Seat

The pilot seat design prioritizes rigidity to prevent eigenmodes within the frequency range of interest (0–10 Hz). It is constructed from solid 8 mm thick folded steel plates, rather than being an adaptation of a commercial automotive or aviation seat. The seat features stepped adjustments for pilot configuration:

- **Vertical Axis:** Two steps of ±25 mm.
- **Longitudinal Axis:** Three steps of ±25 mm.



(a) (b)

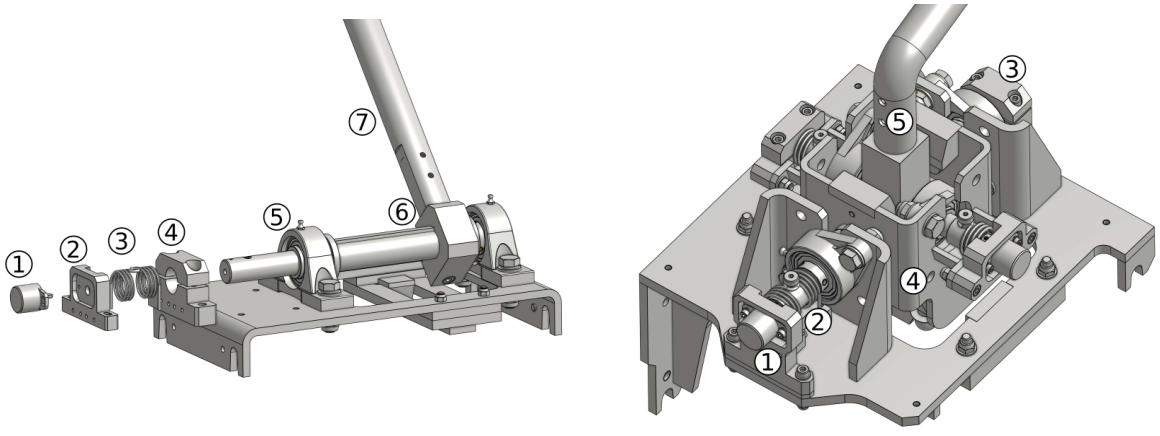
Figure A.3: Illustration of the rigid seat structure, highlighting the stepped vertical and longitudinal adjustment mechanisms.

A.4. Cockpit Inceptors and Control Loading

A.4.1. Inceptors Assembly

The testbed is configured with a passive full mechanical system to replicate the trim-OFF condition of conventional helicopter controls, incorporating mechanical linkages, friction rings, and balancing springs. Crucially, the assembly allows for the reconfiguration of the cockpit layout to represent various rotorcraft while maintaining the correct geometry of the inceptors and the relative position of the pivot point with respect to the Seat Reference Point (SRP). Different physical sticks can be installed to test varying inertial properties; for instance, "Collective 1" (1.21 kg, 0.1352 kg m^2) and "Collective 2" (3.35 kg, 1.5245 kg m^2) have been utilized to assess the impact of control chain inertia on stability.

- **Collective Lever:** Features a torque tube with a rotational balancing spring, an adjustable friction ring, and an analogue encoder for angular position measurement.
- **Cyclic Stick:** A complex assembly where the longitudinal lever is integrated into the lateral one. It is equipped with balancing springs, friction rings, and analogue encoders.
- **Pedal Assembly:** A dummy set of pedals allows pilots to replicate their accustomed foot position, featuring brake/pedal springs, a damper, and a Linear Variable Differential Transformer (LVDT).
- **Force Trim System:** The system includes an electro-actuated brake (activated by a grip push-button) that engages a slider equipped with a linear spring, thereby adding stiffness around the trim position (Trim ON/OFF capability).



(a) (b)

Figure A.4: Exploded views of the Collective (a) and Cyclic (b) inceptor sub-assemblies.

A.4.2. Control Loading System (CLS) Upgrade

The rig includes provisions for an upgrade to an active Control Loading System (CLS) utilizing the Wittenstein Rotary Wing Drop-in solution for the collective axis. This system is capable of reproducing complex force-feel laws (e.g., fly-by-wire) with a continuous torque of 45.5 Nm and a peak torque of 76.5 Nm.

A.5. Instrumentation and Data Acquisition

The data acquisition system is centered around the *Siemens LMS SCADAS Mobile*, which manages up to 40 analogue channels at a sampling frequency of 1024 Hz. For BDFT identification, waveforms are typically bandpass filtered using a double-pass filtering algorithm to eliminate phase distortion.

A.5.1. Sensors

The sensor suite has been expanded to ensure comprehensive kinematic monitoring:

- **Accelerometers:** A total of 9 accelerometers are installed: three are located on the Motion Platform System (MPS) frame to measure input acceleration; three are installed under the pilot seat structure; and three are mounted on the control inceptors (two on the cyclic grip, one on the collective grip) to measure the vibration feedthrough to the pilot's hands.
- **Position Sensors (Angular):** Rotary absolute encoders (*Baumer EAM*280-*Analog*) are employed at the pivot points of the collective and cyclic levers (12-bit resolution, 360° range).
- **Position Sensor (Linear):** A linear potentiometer (*P*34*A Gefran* 100 *mm*) measures pedal deflection.
- **Force Sensors:** Optical force sensors, based on the Frustrated Total Internal Reflection (FTIR) of light, are embedded in the collective and cyclic grips to measure the interaction forces between the pilot and the controls.

A.6. Closed-Loop Simulation Architecture

Closed-loop operations are facilitated by the *Modular Architecture for Reconfigurable Simulation of Helicopters* (MARSH) system, which connects loosely coupled programs via the MAVLink protocol into a unified research flight simulator environment. The core components include:

1. **MARSH Manager:** The central graphical application responsible for handling com-

munication and connectivity.

2. **Pilot Inceptors Interface:** Analog signals are interfaced via a `LabJack T4` board.
3. **Flight Dynamics Model (FDM):** Implemented in MATLAB Simulink, the FDM can represent Linear Time-Invariant (LTI) models (e.g., Bo-105, CH-53) or Collective Bounce 2-DOF models. It receives control inputs and transmits the vehicle state to the motion and visual systems.
4. **Visual System:** The visualization module is developed using the open-source Godot game engine. The pilot views the environment through either:
   - Two *ELO* 2402*L* 24″ touchscreen monitors mounted on the platform.
   - An OpenXR-compatible headset, specifically the *Varjo XR-3*.

   To compensate for platform motion in Virtual Reality (VR), the platform's movement is tracked using a *Vive Tracker 3.0*, and its relative transform is subtracted from the headset position.
5. **MPS Adapter:** The software (`mps-gui`) that links MARSH to the Bosch platform, managing washout filters and safety ramp-up/down sequences.

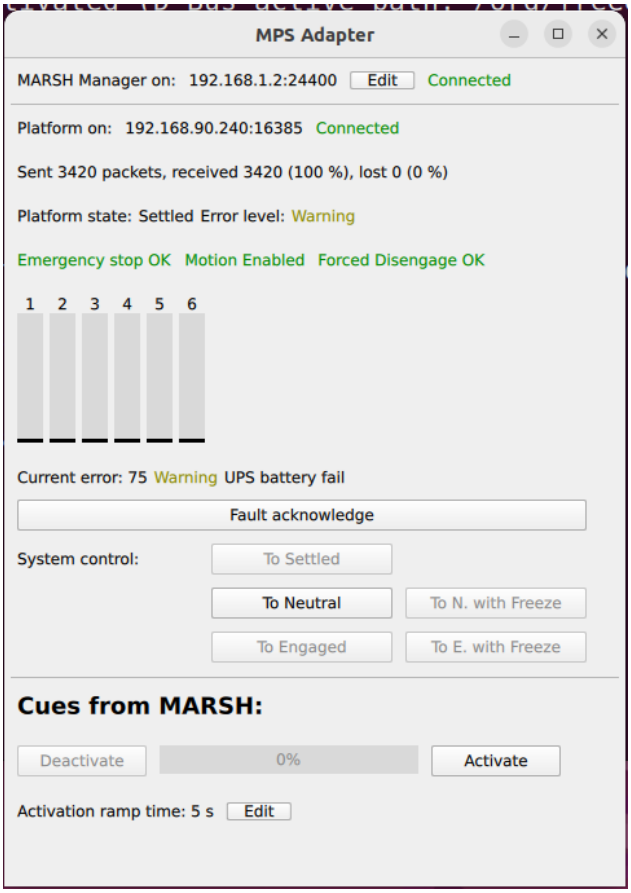
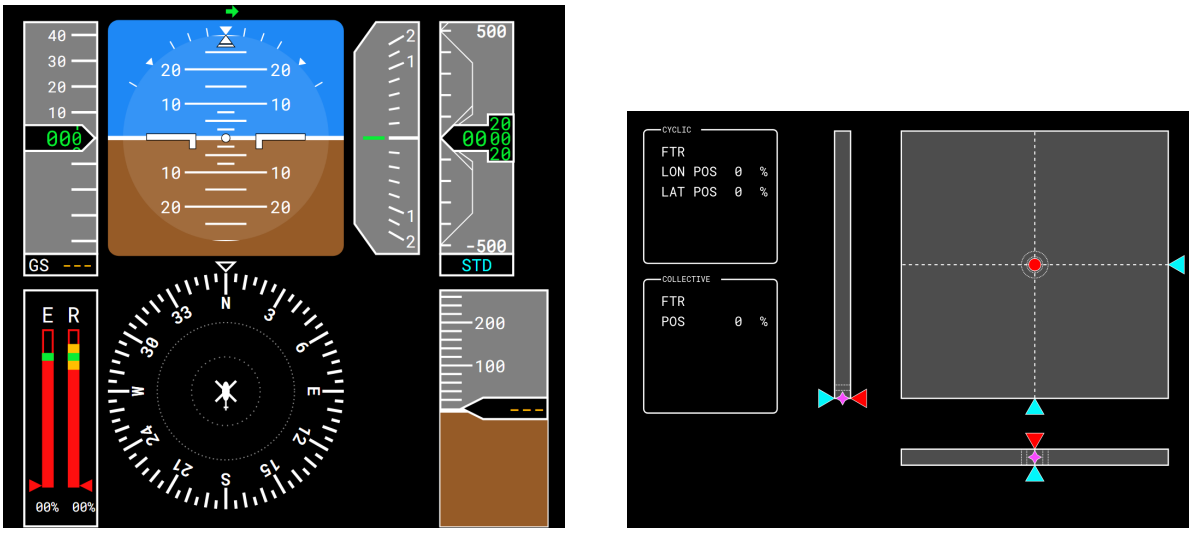


Figure A.5: Screenshot of the MPS Adapter GUI, illustrating the connection status to the MARSH Manager.



(a) (b)

Figure A.6: Visualization of the PFD (Fig A.6a) and controls position display (Fig. A.6b) used in Instrument Meteorological Conditions (IMC) scenarios.

B | Appendix B - The MARSH Simulation Environment

This chapter presents a comprehensive technical analysis of the *Modular Architecture for Reconfigurable Simulation of Helicopters* (MARSH). MARSH constitutes a flexible, distributed simulation environment engineered to integrate heterogeneous hardware and software resources into a cohesive research flight simulator.

The architectural principles, communication protocols, and software specifications detailed herein are grounded in the official technical documentation [40] and the ongoing development activities conducted within the FRAME-Lab of the *Dipartimento di Scienze e Tecnologie Aerospaziali* at Politecnico di Milano.

All documentation relating to MARSH is publicly available at the link: `https://marsh-sim.github.io/`.

B.1. Project Rationale and Research Objectives

The inception of MARSH was driven by the limitations inherent in Commercial-Off-The-Shelf (COTS) simulation platforms. Proprietary solutions frequently impose rigid architectures that impede the integration of experimental control laws, novel Human-Machine Interfaces (HMIs), or custom Flight Dynamics Models (FDMs).

B.1.1. Design Philosophy

The framework addresses these challenges through four foundational pillars:

1. **Decoupling and Modularity:** The system establishes a strict abstraction layer between the simulation core and peripheral components. This facilitates the asynchronous replacement of subsystems (e.g., upgrading a visual generator from FlightGear to Unreal Engine) without necessitating alterations to the core messaging backbone.

2. **Adherence to Open Standards:** By leveraging open-source protocols—specifically MAVLink—the architecture circumvents vendor lock-in, thereby ensuring the longevity

and reproducibility of research data.

3. **Interoperability:** MARSH functions as a middleware bridge, enabling seamless communication between typically incompatible environments, such as MATLAB/Simulink (control design), MBDyn (multibody dynamics), and gaming engines (visualization).
4. **Research-Oriented Workflow:** The ecosystem provides high-level Software Development Kits (SDKs) that abstract network complexity, allowing researchers to concentrate on algorithm implementation rather than low-level network programming.

B.2. System Architecture

MARSH implements a *star network topology* centered around a distinct server application. The architecture is defined by the interaction between the central *Manager* and various distributed clients, designated as *Nodes*.

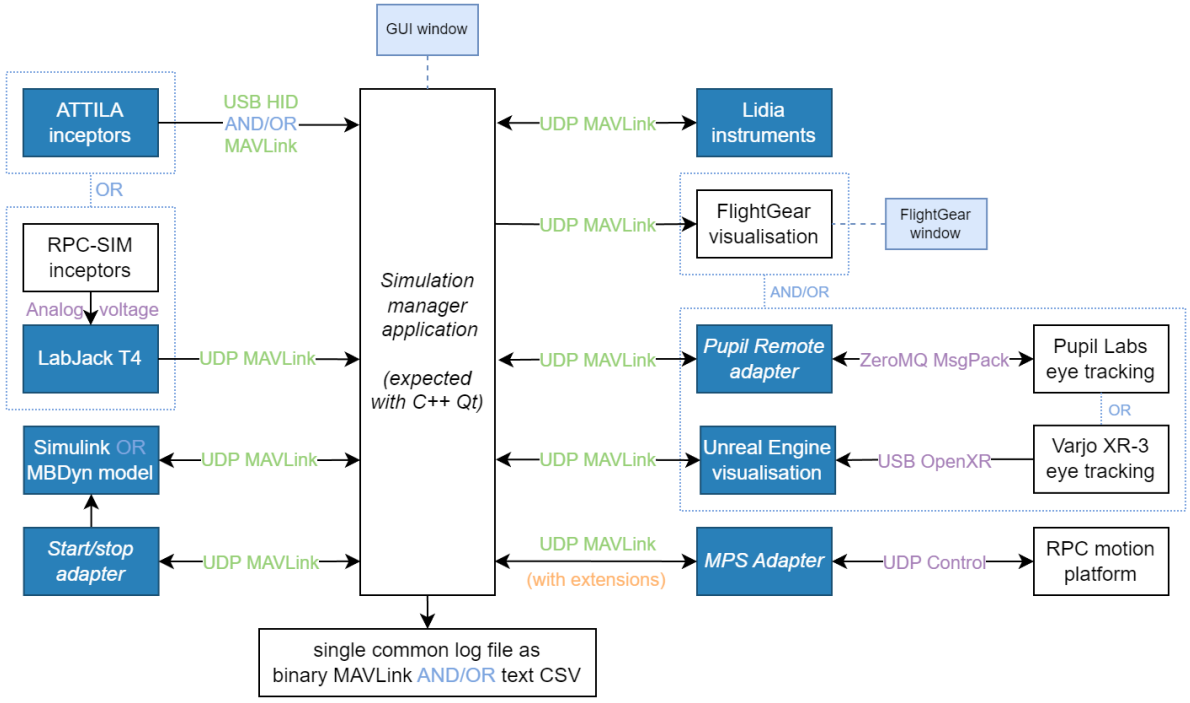


Figure B.1: The star network topology of MARSH, illustrating the central Manager orchestrating data flow between specialized simulation Nodes.

B.2.1. The Core: MARSH Manager

The `marsh-mgr` serves as the critical orchestration unit of the simulation. In its most recent iteration, the Manager has been re-engineered using the *Rust* programming language. This design choice was predicated on the need for memory safety without garbage collection, ensuring the deterministic performance critical for real-time simulation coordination.

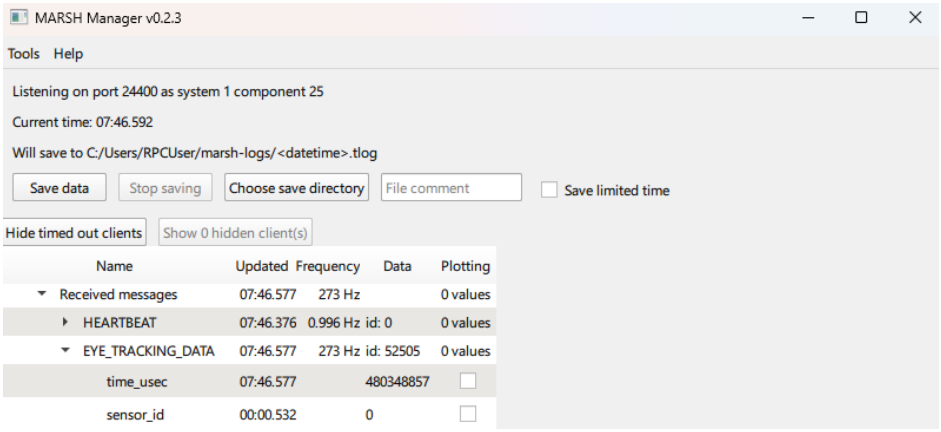


Figure B.2: The graphical user interface of the MARSH Manager, displaying connected nodes, active MAVLink streams, and system health status.

The Manager performs three primary functions:

1. **Message Routing:** It acts as a switchboard, parsing incoming MAVLink packets and routing them to subscribed nodes based on message ID and target component.
2. **Clock Synchronization:** It establishes the master simulation time base, ensuring that data logged from disparate sources (e.g., 1 kHz accelerometer data versus 60 Hz eye-tracking data) can be temporally aligned during post-processing.
3. **State Management:** It controls the lifecycle of the simulation (Standby, Armed, Running, Paused), ensuring that motion platforms and control loading systems engage only when safety criteria are met.

B.2.2. Peripheral Nodes

A "Node" in the MARSH ecosystem is defined as any software application capable of establishing a TCP/UDP socket connection to the Manager and serializing data via the MARSH protocol. This loose coupling allows nodes to be distributed across different operating systems (Linux, Windows, macOS) within a local area network.

Key node categories include:

- **Dynamics Solvers:** Interfaces for MBDyn or compiled Simulink executables serving as the physics engine.
- **Motion Cueing:** Middleware that converts aircraft accelerations into actuator instructions for Stewart platforms (e.g., Bosch Rexroth eMotion).
- **Biometrics:** Modules utilizing the `marsh-py` library to stream data from Tobii eye-trackers or physiological sensors.

B.3. Software Development Ecosystem

To accelerate the development of experimental setups, the FRAME-Lab maintains a suite of libraries that serve as the integration middleware for the architecture.

B.3.1. Rapid Prototyping: `marsh-py`

`marsh-py` is the official Python client library. It exposes a high-level API that encapsulates the low-level serialization logic. It enables researchers to instantiate a simulation node in fewer than 20 lines of code, making it ideal for scripting experiment logic or processing non-real-time signals.

B.3.2. Cockpit Visualization: LIDIA

For the creation of glass cockpit interfaces, the framework utilizes *LIDIA* (Library for Instrument Display Interface for Aviation). LIDIA is a Python-based rendering engine optimized for vector graphics.

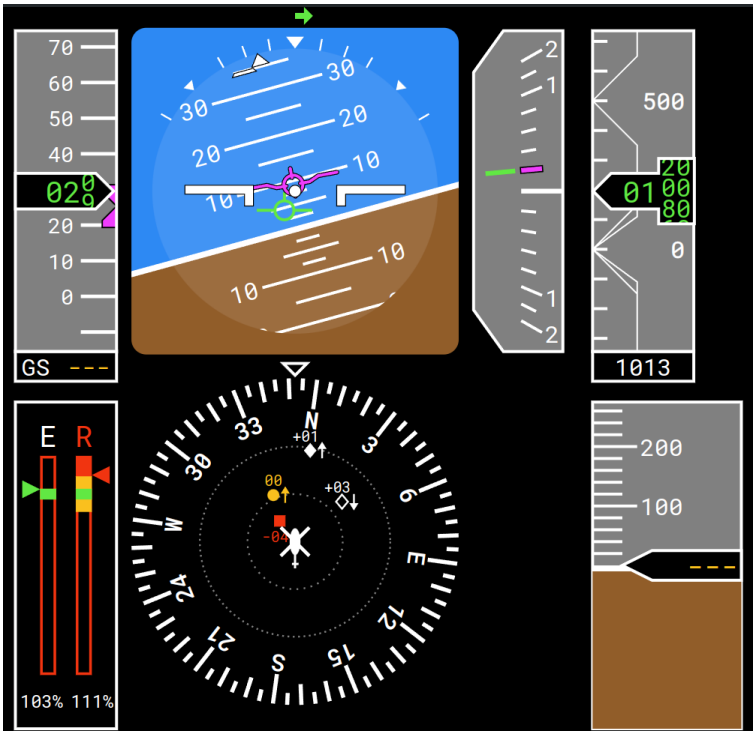


Figure B.3: An example of a reconfigurable Primary Flight Display created with LIDIA, demonstrating vector-based gauge rendering.

Unlike raster-based image displays, LIDIA's vector approach ensures that flight instruments remain resolution-independent and visually sharp at any scale. It uses a declarative syntax to define instrument behaviors, allowing for the rapid reconfiguration of cockpit layouts

between different experimental conditions.

B.4. Communication Protocol: MAVLink Integration

The backbone of MARSH is the MAVLink protocol, a lightweight, header-only message marshalling library. MAVLink was selected for its bandwidth efficiency (crucial for UDP transmission) and its robust code-generation tools for C, C++, Python, and MATLAB.

B.4.1. The MARSH Custom Dialect

Standard MAVLink definitions cover basic UAV telemetry. To support piloted rotorcraft simulation, MARSH extends this with a custom XML definition file (`marsh.xml`). This dialect introduces high-fidelity message sets required for Human-In-The-Loop (HITL) simulation.

Component Enumeration

To facilitate precise routing, the `MARSH_TYPE` enumeration extends the standard `MAV_TYPE` field. This allows the Manager to distinguish between semantically different nodes.

Table B.1: Extended Component Types in the MARSH Dialect

ID	Enum Identifier	Function Description
100	`MARSH_TYPE_MANAGER`	The simulation server/hub.
101	`MARSH_TYPE_FLIGHT_MODEL`	The physics engine (e.g., MBDyn).
105	`MARSH_TYPE_MOTION_PLATFORM`	Hexapod motion system interface.
107	`MARSH_TYPE_EYE_TRACKER`	Gaze vector and pupilometry source.
108	`MARSH_TYPE_CONTROL_LOADING`	Active force-feedback stick interface.
111	`MARSH_TYPE_EXPERIMENT_DIRECTOR`	Automated scenario controller.

Critical Message Definitions

The custom dialect defines data structures that are absent in standard UAV protocols:

- `MOTION_PLATFORM_STATE`: Encapsulates the 6-DOF position, velocity, and acceleration of the cockpit centroid, used for washout filter verification.
- `CONTROL_LOADING_AXIS`: A bidirectional message carrying stick position (input to FDM) and force requirements (output to motors), operating at high frequencies (> 500 Hz) to ensure haptic stability.
- `HUMAN_BODY_POSE`: Transmits skeletal tracking data (33 keypoints) derived from computer vision models (e.g., MediaPipe) for ergonomic analysis.

B.5. Data Acquisition and Analysis Workflow

Data integrity is maintained through a centralized logging mechanism. The Manager records all network traffic into MAVLink Telemetry Logs (`.tlog`), a binary format that captures every message with microsecond-resolution timestamps.

B.5.1. Post-Processing in MATLAB

Given the widespread adoption of MATLAB in aerospace engineering, the MARSH workflow is optimized for the MATLAB *UAV Toolbox*. However, due to the custom nature of the protocol, a specific initialization procedure is required to parse the binary logs correctly:

1. **Dialect Compilation:** The `marsh.xml` definition must be compiled into a '.m' format or loaded dynamically using `mavlinkdialect`.
2. **Sequential Loading:** The standard `common.xml` dialect must be loaded prior to the custom dialect to resolve dependencies.
3. **Time-Series Extraction:** The `mavlinktlog` function is utilized to extract specific topics (e.g., `MOTION_PLATFORM_STATE`) into `timeseries` objects, facilitating direct correlation analysis between pilot inputs and aircraft response.

List of Figures

1.1 Schematization of the RPC closed loop 2
1.2 Sling Load Operation 5
1.3 High-Speed Maneuvering helicopter example 6
1.4 Flow block diagram of the PVS 7
1.5 Shipboard helicopter operations 8

2.1 Dead Man's Curve 16
2.2 Smooth ramp profile 18
2.3 Example of Attack Chart 19

3.1 AP propagation 22
3.2 Positions of eletrodes over IZ 24
3.3 Example of eye tracking measurement 27
3.4 Typical Heart Rate profile during complex special flight operations 30
3.5 Cross country flight route 31
3.6 Comparison of machine learning algorithms 31
3.7 Body pose reconstruction 34
3.8 Total Internal Reflection (TIR) 37
3.9 Structure of the Bedford Workload Scale (BWS) 39

4.1 Raw-Power system 41
4.2 Electrode siting 42
4.3 Electrode real placement example 43
4.4 Raw-Power interface 44
4.5 Raw vs filtered signal 45
4.6 RMS, MNF features 46
4.7 Filtered signal vs VAR 47
4.8 Filtered signal vs MDF 47
4.9 sEMG Spectrogram 48
4.10 Pupil Core eye tracking glasses 49
4.11 GUI of Pupil Capture software 50
4.12 Pupil diameter analysis over time 54
4.13 Blink analysis 55

4.14 Fixation analysis . . . 56
4.15 ECG Measurement System Architecture . . . 57
4.16 Functional block diagram of the AD8232 sensor . . . 57
4.17 AD8232 Cable and Electrodes . . . 58
4.18 STM32 Nucleo-64 board . . . 59
4.19 Signal Visualization and Windowing . . . 61
4.20 Peak Detection . . . 62
4.21 BPM and Heart Rate Estimation . . . 62
4.22 Intel RealSense D455f camera . . . 63
4.23 Body pose estimation via Camera . . . 67
4.24 Schematic of OPT-IN sensing channels . . . 68
4.25 Mechanical integration of the OPT-IN prototype sensor . . . 69

5.1 Example helicopters . . . 72
5.2 Suggested course layout for Vertical Reposition maneuver . . . 74
5.3 ADS-33E FRAME lab test tower . . . 77
5.4 Pilot POV during the simulation . . . 77
5.5 External POV during the simulation . . . 78

6.1 Final arrangement of modules on the simulator . . . 79
6.2 sEMG Card Location . . . 80
6.3 sEMG electrode placement and eye tracking system . . . 81
6.4 ECG Sensor's Case . . . 82
6.5 ECG module installation . . . 83
6.6 Body pose camera position . . . 83
6.7 OPT-IN Sensor's Case . . . 84
6.8 OPT-IN module installation . . . 85
6.9 OPT-IN sensor installation . . . 85
6.10 Position of the EMG sensors on the pilot's left arm . . . 87
6.11 Pilot all muscles filtered signal . . . 88
6.12 Pilot all muscles signals RMS . . . 89
6.13 Pilot all muscles fatigue analysis . . . 89
6.14 Non pilot all muscles filtered signal . . . 90
6.15 Non pilot all muscles signals RMS . . . 91
6.16 Non pilot all muscles fatigue analysis . . . 91
6.17 Pupils diameter analysis . . . 92
6.18 Blink analysis . . . 93
6.19 fixation analysis . . . 93
6.20 R-Peak detection Pilot . . . 94
6.21 Zoom on R-Peak detection Pilot . . . 95

6.22 BPM and Heart Rate detection Pilot 95
6.23 R-Peak detection Non Pilot 96
6.24 Zoom on R-Peak detection Non Pilot 96
6.25 BPM and Heart Rate detection Non Pilot 97
6.26 Body pose comparison 97
6.27 Body pose tracking in challenging conditions 98
6.28 OPT-IN detection Pilot 99
6.29 OPT-IN detection Non Pilot 100

A.1 RPC Test Rig 116
A.2 Dynamic response performance Test Rig 117
A.3 Pilot Seat 118
A.4 Exploded Collective and Cyclic inceptor 119
A.5 MPS Adapter GUI 121
A.6 PFD Visualization 122

B.1 MARSH Architecture Topology 124
B.2 MARSH Manager Interface 125
B.3 LIDIA Instrument Panel 126

List of Tables

2.1 Physiological Parameters and Correlation Trends 14

4.1 MAVLink Message: EYE_TRACKING_DATA 51
4.2 MAVLink Message: EYE_TRACKING_EVENT 53

5.1 Performance - Vertical Maneuver 75

7.1 Summary of Specific Test Objects (STOs) for Workload Validation 105

A.1 eMotion 1500 Motion Platform Range of Motion 116
A.2 eMotion 1500 Motion Platform Acceleration Capabilities 117

B.1 Extended Component Types in the MARSH Dialect 127

List of Symbols

Variable	Description	SI unit
β_0	main rotor collective flap/coning angle	rad or deg
C_ℓ	collective lever rotational damping	$N \cdot m \cdot s/rad$
C_T	collective lever equivalent damping due to force trim	$N \cdot m \cdot s/rad$
c	viscous coefficient	$N \cdot s/m$
c_p	equivalent pilot biomechanical viscous coefficient	$N \cdot s/m$
Δ	amplitude or increment	various
δ_0	collective lever position/rotation	rad or deg
δ_c	lateral cyclic rotation	rad or deg
δ_s	longitudinal cyclic rotation	rad or deg
δ_3	pitch-flap coupling	deg
$\mathbf{F}_{ext}$	external force vector	N
F_{probe}	force measured by OPT-IN probe	N
F_{th}	OPT-IN activation threshold force	N
f	frequency	Hz
f_s	sampling frequency	Hz
f_{HP}	high-pass filter frequency	Hz
f_{LP}	low-pass filter frequency	Hz
G_0	gear ratio (collective lever to pitch)	-
G_m	gain margin	dB
g	gravity acceleration	m/s^2
g_{pk}	peak gradient	units/s
γ	Lock number	-
$H(s)$	generic transfer function	various
H_{B2P}	BDFT to Position transfer function	-
H_{BDFT}	pilot Biodynamic Feedthrough transfer function	-
H_{LTF}	Loop Transfer Function	-

Continued on next page

List of Symbols – Continuation

Variable	Description	SI unit
H_{NMA}	pilot Neuromuscular Admittance transfer function	-
$H_{\ddot{z}\vartheta_0}$	helicopter vertical acceleration response	$m/s^2/rad$
h	altitude (AGL)	ft or m
I_β	blade inertia moment about the flap hinge	$kg \cdot m^2$
I_{xx}, I_{yy}, I_{zz}	moments of inertia	$kg \cdot m^2$
I_{xz}	product of inertia	$kg \cdot m^2$
J_ℓ	collective lever equivalent inertia	$kg \cdot m^2$
K_ℓ	collective lever rotational stiffness	$N \cdot m/rad$
K_T	collective lever equivalent stiffness due to force trim	$N \cdot m/rad$
k	stiffness	N/m
k_p	equivalent pilot biomechanical stiffness	N/m
L_{ext}	external rolling moment	$N \cdot m$
ℓ	collective lever length	m
M	moment acting on the collective control lever	$N \cdot m$
M_c	control torque applied by pilot	$N \cdot m$
M_{ext}	external pitching moment	$N \cdot m$
M_p	modal mass	kg
m	helicopter mass	kg
m_ℓ	collective lever mass	kg
m_p	equivalent pilot biomechanical mass	kg
N	number of samples	-
N_{ext}	external yawing moment	$N \cdot m$
N_b	number of blades	-
ν_β	dimensionless flap frequency	/rev
Ω	rotor speed	rad/s or rpm
ω_{LG}	landing gear heave mode natural frequency	rad/s
ω_n	natural frequency	rad/s
ω_p	pilot biomechanical natural frequency	rad/s
P_m	phase margin	deg
p	roll rate	rad/s
q	pitch rate	rad/s
R	rotor radius	m

Continued on next page

List of Symbols – Continuation

Variable	Description	SI unit
r	yaw rate	rad/s
s	Laplace variable	$1/s$
S_β	blade static moment about the flap hinge	$kg \cdot m$
S_ℓ	collective lever static moment about pivot point	$kg \cdot m$
T_ϑ	thrust coefficient derivative	N/rad
t	time	s
θ	pitch attitude	rad or deg
ϑ_0	main rotor collective pitch	rad or deg
$\mathbf{u}$	control vector	various
u	longitudinal velocity (body frame)	m/s
v	lateral velocity (body frame)	m/s
w	vertical velocity (body frame)	m/s
$\mathbf{x}$	state vector	various
x	linear displacement	m
x_{CM}	collective lever center of mass offset	m
$\dot{x}$	linear velocity	m/s
$\ddot{x}$	linear acceleration	m/s^2
z	vertical plunge motion	m
$\ddot{z}$	vertical acceleration	m/s^2
ζ	damping ratio	-
ξ_{LG}	landing gear heave mode damping ratio	% or -
ξ_p	pilot biomechanical damping ratio	% or -
ϕ	roll attitude	rad or deg
ψ	yaw attitude/heading	rad or deg

List of Abbrevations

Abbreviation	Meaning
AAS	Adaptive Automation Systems
ADC	Analog-to-Digital Converter
AFE	Analog Front-End
AGL	Above Ground Level
ANS	Autonomic Nervous System
AOI	Area of Interest
AP	Action Potential
APC	Aircraft-Pilot Coupling
API	Application Programming Interface
ARV	Average Rectified Value
AUC	Area Under the Curve
B2P	BDFT to Position
BDFT	Biodynamic Feedthrough
BPM	Beats Per Minute
BSW	Bedford Workload Scale
CART	Classification and Regression Trees
CFIT	Controlled Flight Into Terrain
CLS	Control Loading System
CMRR	Common-Mode Rejection Ratio
CNS	Central Nervous System
COTS	Commercial-Off-The-Shelf
CRITIC	Criteria Through the Inter-criteria Correlation
CV	Conduction Velocity
DAER	Dipartimento di Scienze e Tecnologie Aerospaziali
DOF	Degrees Of Freedom
DVE	Degraded Visual Environment

Continued on next page

List of Abbreviations – Continuation

Abbreviation	Meaning
ECG	Electrocardiogram
EDA	Electrodermal Activity
EEG	Electroencephalography
EMG	Electromyography
ETA	Eye Tracking in Aviation
EWMA	Exponentially Weighted Moving Average
FBW	Fly-By-Wire
FCS	Flight Control System
FDM	Flight Dynamics Model
FFT	Fast Fourier Transform
FOV	Field Of View
FRP	Finger Reference Point
FTIR	Frustrated Total Internal Reflection
GMM	Gaussian Mixture Model
GPU	Graphics Processing Unit
GSR	Galvanic Skin Response
GUI	Graphical User Interface
GVE	Good Visual Environment
HD	High Density
HF	High Frequency
HITL	Human-In-The-Loop
HMI	Human-Machine Interface
HQR	Handling Quality Ratings
HR	Heart Rate
HRV	Heart Rate Variability
HSDI	Helicopter-Ship Dynamic Interface
HSI	Human-System Interaction
HUD	Head-Up Display
IA	Instrumentation Amplifier
IAS	Indicated Airspeed
ICP	Iterative Closest Point
IEMG	Integrated EMG

Continued on next page

List of Abbreviations – Continuation

Abbreviation	Meaning
IFR	Instrument Flight Rules
IMC	Instrument Meteorological Conditions
IMU	Inertial Measurement Unit
IR	Infrared
IZ	Innervation Zone
KIAS	Knots Indicated Airspeed
KNN	K-Nearest Neighbors
LA	Left Arm
LED	Light Emitting Diode
LF	Low Frequency
LIDIA	Library for Instrument Display Interface for Aviation
LoSA	Loss of Situation Awareness
LTF	Loop Transfer Function
LTI	Linear Time-Invariant
LVDT	Linear Variable Differential Transformer
MARSH	Modular Architecture for Reconfigurable Simulation of Helicopters
MAV	Mean Absolute Value
MCP	Maximum Continuous Power
MCU	Microcontroller Unit
MDF	Median Spectral Frequency
MFD	Multi-Function Display
MH	Medium-Heavy (Helicopter Class)
ML	Medium-Light (Helicopter Class)
MNF	Mean Spectral Frequency
MSE	Mean Squared Error
MSRP	Mean Seat Reference Point
MTE	Mission Task Element
MU	Motor Unit
MUAP	Motor Unit Action Potential
MVC	Maximum Voluntary Contraction
MWL	Mental Workload
NASA − TLX	NASA Task Load Index

Continued on next page

List of Abbreviations – Continuation

Abbreviation	Meaning
NMA	Neuromuscular Admittance
NMJ	Neuromuscular Junction
OFE	Outside Flight Envelope
OPT − IN	Optical Inceptor
PAC	Phase-Aggression Criterion
PAO	Pilot-Assisted Oscillation
PC	Personal Computer / Polycarbonate
PCHIP	Piecewise Cubic Hermite Interpolating Polynomial
PDR	Pupil Diameter Rate
PFD	Primary Flight Display
PIO	Pilot-Induced Oscillation
POV	Point Of View
PPG	Photoplethysmography
PPL	Private Pilot License
PSD	Power Spectral Density
PVS	Pilot-Vehicle System
RA	Right Arm
RAE	Royal Aircraft Establishment
RAP	Resonance Assessment Profile
RCO	Reduced-Crew Operations
RF	Random Forest
RGB	Red-Green-Blue
RL	Right Leg
RLD	Right Leg Drive
RMS	Root Mean Square
RMSSD	Root Mean Square of Successive Differences
RPC	Rotorcraft-Pilot Coupling
SA	Situation Awareness
SC	Skin Conductance
SCOPE	Spare Capacity Operator Estimator
SCR	Skin Conductance Response
SDK	Software Development Kit

Continued on next page

List of Abbreviations – Continuation

Abbreviation	Meaning
SDNN	Standard Deviation of NN intervals
sEMG	Surface Electromyography
SENIAM	Surface EMG for Non-Invasive Assessment of Muscles
SFE	Service Flight Envelope
SISO	Single-Input Single-Output
SLC	Skin Conductance Level
SPO	Single-Pilot Operations
SSC	Slope Sign Change
STO	Specific Test Object
SVM	Support Vector Machines
SWB	Symmetric Wing Bending
TIR	Total Internal Reflection
UAV	Unmanned Aerial Vehicle
USB	Universal Serial Bus
VAR	Variance
VFR	Visual Flight Rules
VHT	Van Halteren Technologies
VMC	Visual Meteorological Conditions
VR	Virtual Reality
VTOL	Vertical Take-Off and Landing
WAMP	Willison Amplitude
WL	Wavefront Length
WR	Workload Rating
ZC	Zero Crossing

Ringraziamenti

A conclusione di questo lavoro di tesi, che segna il termine del mio percorso di studi e, per ora, della mia esperienza al Politecnico di Milano, desidero dedicare queste pagine per esprimere la mia profonda gratitudine a chi mi ha supportato — e talvolta pazientemente sopportato — in questi anni.

È stato un percorso lungo e complesso, le cui radici risalgono a ben prima della scelta universitaria: già dai tempi delle scuole medie, infatti, aveva iniziato a prendere forma in me la decisione di intraprendere la strada dell'ingegneria aerospaziale, concretizzatasi poi nei corsi di Ingegneria Aerospaziale e, infine, in quelli di Ingegneria Aeronautica.

Alla luce di tutto il tempo trascorso, desidero ringraziare coralmente tutte le persone che ho incontrato lungo il cammino: da chi è stato al mio fianco sin dal primo giorno a chi ho conosciuto solo negli ultimi mesi di lavoro; da chi mi ha vissuto nella mia quotidianità e informalità, a chi ha conosciuto esclusivamente la mia veste più professionale. A tutti voi, un sincero grazie.

Il mio primo e più formale ringraziamento va ai Professori Zanoni e Masarati, per avermi dato l'opportunità di prendere parte a questa meravigliosa esperienza. Li ringrazio per l'insostituibile supporto, per le nozioni che mi hanno trasmesso e per la preziosa libertà che mi hanno concesso nella scelta di alcune metodologie di prova.

Un grande grazie va a Marek e Ahmad, per l'aiuto fondamentale nella realizzazione e implementazione dei sensori, per la stesura dei software e, non da ultimo, per il tempo trascorso insieme e le risate condivise. Ringrazio inoltre tutto il personale dei laboratori dell'edificio B14: siete sempre stati estremamente disponibili e pronti a collaborare in ogni attività e necessità legata ai miei esperimenti.

Esprimo la mia gratitudine all'Ingegner Paolo Belluco e all'azienda LWT3 per la disponibilità e la collaborazione nello sviluppo del sistema sEMG, e all'Ingegner Michele Zilletti, insieme a tutto il suo team di Leonardo Helicopter Division, per il prezioso supporto ricevuto durante le prove di volo.

Un ringraziamento fondamentale è rivolto ai Comandanti Fabio Bocola e Andrea Scopa: avete reso possibile la realizzazione di molti dei nostri test, mi avete dispensato consigli preziosi e siete stati, senza dubbio, un grande esempio per me. Un pensiero di gratitudine va

anche al Comandante Domenico Grande: la sua esperienza e disponibilità durante il corso di sperimentazione in volo sono state determinanti nell'ispirare la mia volontà di impegnarmi in questo specifico ambito sperimentale.

Il grazie più profondo e sentito va alla mia famiglia. A mia madre Stefania, che ha sempre creduto nelle mie capacità e mi ha costantemente spronato a dare il massimo; anche quando gli argomenti dei miei studi le risultavano complessi, non ha mai fatto mancare il suo appoggio. Spero, al termine di questo lungo percorso scientifico, di averla resa fiera di me. A mio padre Giorgio: seppur con le nostre differenze, mi hai trasmesso l'inestimabile valore della flessibilità, dote che mi ha permesso di superare diverse impasse lungo il cammino. A mio fratello Mathias, che forse avrebbe meritato un fratello diverso, e invece si è ritrovato un ingegnere con tutti i difetti del caso, compresa l'eccessiva tendenza alla programmazione. Grazie per avermi sopportato e per non esserti mai tirato indietro dal tuo ruolo di fratello; sono molto fiero di te.

Una parte essenziale del mio percorso si fonda sui valori di semplicità che mi hanno trasmesso i miei nonni, Maria Carla e Giancarlo. Credo che uno dei motivi per cui ho scelto l'ingegneria sia nato molto tempo fa, aiutando mio nonno nei lavoretti di casa, tra il giardino e le innumerevoli riparazioni in cantina. Un pensiero pieno d'affetto va anche ai miei Oma Elizabeth e Opa Willhem, che mi hanno accompagnato in questi anni. Sono certo che Opa mi abbia seguito da lassù, sia nel mio percorso di studi, sia in tutte le escursioni in montagna che non abbiamo fatto in tempo a condividere.

Grazie ad Elisa, che ha sempre cercato di supportarmi in ogni modo possibile, accogliendo le mie peculiarità, standomi accanto con pazienza e condividendo il peso del mio lavoro.

Un grazie di cuore a Margherita, Gregory, Alessia, Demi, Maddalena, Elena, Arianna, Paola e Daniele con la piccola Minni, Chiara ed Edoardo, per esserci sempre stati, in tutto e per tutto.

Un pensiero speciale va ai compagni che hanno condiviso con me gli anni del Politecnico, tra corsi ed esperienze vissute insieme: Valeria, Luca, Stefano, Enrico, Mattia, Silvia, Luca, Leonardo, Lucrezia, Andrea, Martina, Luca, Carolina, Giulia, Pier ed Enrico. Ognuno di voi ha lasciato un segno indelebile in questo viaggio.

Grazie ai miei compagni di avventura durante il periodo di tesi: Paolo, Olga e Rebecca. Mi avete supportato — e sopportato — unendo le idee, aiutandomi praticamente nelle varie prove di volo, nei pranzi e negli esperimenti.

Infine, ringrazio tutti i docenti che ho incrociato nel mio percorso universitario, con una menzione particolare ai Professori Cefis, Dedè, Trainelli e Rolando. Senza i vostri insegnamenti, i vostri consigli e le costruttive discussioni, non potrei essere l'ingegnere che mi appresto a diventare.